

1-1-2009

Modeling And Development Of An Experimental Pneumatic Facility For Aircraft Bleed Air System Studies

Dale Molenaar
Ryerson University

Follow this and additional works at: <http://digitalcommons.ryerson.ca/dissertations>



Part of the [Aerospace Engineering Commons](#)

Recommended Citation

Molenaar, Dale, "Modeling And Development Of An Experimental Pneumatic Facility For Aircraft Bleed Air System Studies" (2009). *Theses and dissertations*. Paper 1168.

This Thesis is brought to you for free and open access by Digital Commons @ Ryerson. It has been accepted for inclusion in Theses and dissertations by an authorized administrator of Digital Commons @ Ryerson. For more information, please contact bcameron@ryerson.ca.

TL
201.1
M68
2009

MODELING AND DEVELOPMENT OF AN EXPERIMENTAL PNEUMATIC FACILITY FOR AIRCRAFT BLEED AIR SYSTEM STUDIES

by

Dale Molenaar

Bachelor of Engineering in Aerospace Engineering
Ryerson University, 2007

A thesis

presented to Ryerson University

in partial fulfillment of the

requirements for the degree of

Master of Applied Science

In the Program of

Aerospace Engineering

Toronto, Ontario, Canada

© Dale Molenaar, 2009

Author's Declaration

I hereby declare that I am the sole author of this thesis.

I authorize Ryerson University to lend this thesis to other institutions or individuals for the purpose of scholarly research.

Dale Molenaar

I further authorize Ryerson University to reproduce this thesis by photocopying or by other means, in total or in part, at the request of other institutions or individuals for the purpose of scholarly research.

Dale Molenaar

Modeling and Development of an Experimental Pneumatic Facility
For Aircraft Bleed Air System Studies

Dale Molenaar

Bachelor of Engineering in Aerospace Engineering, 2007

Master of Applied Science in Aerospace Engineering, Ryerson University

Abstract

Research on aircraft bleed air systems has been performed at Ryerson University for the last eight years. During this time, the requirements of the test apparatus have been constantly expanding. This thesis work aims at developing a new reconfigurable rig that supports current and future research on aircraft bleed air control systems and takes advantage of lessons learned from previous test rigs. The new rig consists of two temperature control channels in a parallel arrangement to allow for flow sharing control, and a load tank with variable exhaust. Beyond the development of the test rig, research has been performed to improve mass flow measurement based on signals from traditional thermal mass flow and pressure sensors. The proposed method utilizes these redundant means of indicating flow to obtain fast and accurate flow measurement through the use of a dynamically weighted average. This method has been experimentally investigated using the test rig.

Acknowledgements

I would like to thank my Professor, G. Liu, for giving me the great privilege of designing and building a test rig for current and future research in the Systems and Controls Laboratory. As well, I would like to express my appreciation for his faith in my abilities, his balanced viewpoint when the project was beginning, and his encouragement during difficult times when nothing seemed to go as planned.

Also, I would like to thank the Ryerson Technical Staff for their help and dedication to this project. Foremost, I would like to acknowledge P. Cresnik for his unwavering support and drive throughout the project. Without his help and expertise, I would have been hard pressed to move the project beyond the initial planning. Among other things, he enabled me to learn a great deal about data acquisition systems in a short period of time, in order to construct the terminal boxes to interface all of the sensors with the computer. In addition, I would also like to thank G. Bootes, H. Ghaemi, and P. Bradley, for their advice and encouragement, donated components, and machining expertise.

Next, I would like to thank the other students in the Systems and Controls Laboratory for their patience during the installation and testing of the system. As well, I would like to thank L. Shang for her help with learning SIMULINK, and S. Shah for his input on the heat exchangers.

Finally, special thanks to my mom and stepdad, Shelley and Ian Laird, for their support throughout my university career and my sister, Annalecia, for making sure that I take a break and go out once in a while. I would also like to thank my brother and his wife, Stephen and Lisa, as well as my half-brothers, Eric and Evan, for their patience and understanding during my university career.

Dedication

I would like to dedicate this work to my Dad, John 'Hank' Molenaar,
who passed away in 2001.

Wish I could have showed the rig to you once, pretty sure you
would have said,

"Well, that ain't gonna move."

Table of Contents

Author's Declaration	ii
Abstract	iii
Acknowledgements	iv
Dedication	v
Table of Contents	vi
List of Tables	viii
List of Figures	x
1 Introduction	1
1.1 Objectives and Organization.....	1
1.2 Background Information	2
1.2.1 Bleed Air System	3
1.2.2 Environmental Control System	4
1.2.3 Sensors.....	5
1.2.4 Sensor Fusion	7
1.2.5 Previous Test Rigs.....	8
1.3 Literature Review	10
1.4 Purpose.....	13
2 Test Rig.....	14
2.1 Requirements	14
2.2 Design and Construction	15
2.2.1 Major Components.....	26
2.2.2 Sensors.....	33
2.3 Instrumentation	37
2.3.1 Wiring Diagrams.....	38
2.3.2 Construction.....	38
2.4 Calibration	46
2.4.1 Resistance Temperature Detectors.....	47
2.4.2 Thermocouples.....	52
2.4.3 Pressure Sensors	55

2.4.4	Flow Sensors	59
2.4.5	Potentiometers	61
2.5	Software	64
3	Theoretical Model	73
3.1	Thermal Flow Sensor Model.....	74
3.2	Orifice Plate Flow Sensor Model.....	82
3.3	Sensor Fusion between Thermal and Orifice Plate Flow Meters.....	87
3.4	Pressure Drop along a Channel.....	91
4	Experimental Work	103
4.1	Flow Rate Calculation.....	104
4.2	Hybrid Sensor Algorithm Validation.....	112
4.3	Flow Control using the Hybrid Algorithm	116
5	Conclusion and Future Research	121
5.1	Conclusion	121
5.2	Future Research	123
	References	125
	Appendix A: TSSA Approved Drawings	128
	Appendix B: Wiring Diagrams	139

List of Tables

Table 1: Measured Resistance between Pins for RTDs and Pin Information.....	34
Table 2: Pressure Sensor Information	35
Table 3: RTD 100C-123 Calibration Data: 1 mA Excitation	47
Table 4: RTD 113C-0203 Calibration Data: 1 mA Excitation	47
Table 5: RTD Polynomial Calibration Values: 1 mA Excitation	49
Table 6: RTD 113C-0203 Calibration Data: 3 mA Excitation	50
Table 7: RTD 113C-0203 Calibration Data: 5 mA Excitation	50
Table 8: RTD 100C-123 Calibration Data: 3 mA Excitation	50
Table 9: RTD 100C-123 Calibration Data: 5mA Excitation	51
Table 10: Total Resistances for Given Temperature and Excitation	51
Table 11: RTD Polynomial Calibration Values: 5 mA Excitation	52
Table 12: Thermocouple Calibration Measurements, Channels 17-18.....	53
Table 13: Thermocouple Calibration Measurements, Channels 19-20.....	53
Table 14: Thermocouple Calibration Measurements, Channels 21-22.....	53
Table 15: Thermocouple Calibration Measurements, Channels 23-24.....	53
Table 16: Thermocouple Calibration Measurements, RTD Readings and Channel 25.....	54
Table 17: Thermocouple Coefficients: Channels 17-19	54
Table 18: Thermocouple Coefficients: Channels 20-22	54
Table 19: Thermocouple Coefficients: Channels 23-25	55
Table 20: PX303 Calibration Data: Channels 2 and 3	56
Table 21: PX303 Calibration Data: Channels 4 and 5	56
Table 22: PX209 Calibration Data: Channels 6 and 7	57
Table 23: PX219 Calibration Data: Channels 9 and 11	57

Table 24: CA150 Handheld Calibration Unit Pressure Sensor Data	57
Table 25: Pressure Transducer Coefficients: 2 to 4.....	58
Table 26: Pressure Transducer Coefficients: 5 to 7.....	58
Table 27: Pressure Transducer Coefficients: 9 and 11	58
Table 28: Thermal Flow Sensor Calibration Data: Channel 2.....	60
Table 29: Thermal Flow Sensor Polynomial Coefficients: Channel 2	60
Table 30: Valve Calibration Data for Bottom Bleed and Outflow Channels	62
Table 31: Average Calibration Data for Bottom Bleed and Outflow Channels.....	63
Table 32: Polynomial Coefficients for Bottom Bleed and Outflow Valves	63
Table 33: Flow Sensor Physical Parameters Relevant to Model	79
Table 34: Simulated Thermal Flow Sensor Data	80
Table 35: Flow Sensor Model Signal Calibration.....	81
Table 36: Physical Parameters for Orifice Plate Flow Meter	84
Table 37: Orifice Plate Flow Meter Results.....	85
Table 38: Assumed Coefficients for Channel Model	95
Table 39: Pressure Drop with respect to Flow Rate and Opening Angle - 0° to 40°	96
Table 40: Pressure Drop with respect to Flow Rate and Opening Angle - 50° to 90°	96

List of Figures

Figure 1: Two Channel Flow Sharing Test Rig Diagram	8
Figure 2: Four Channel Flow Sharing Test Rig Diagram	9
Figure 3: Temperature Control Test Rig Diagram	9
Figure 4: Conceptual Isometric View of New Test Rig.....	17
Figure 5: Conceptual View of Supply Lines and Tanks.....	18
Figure 6: Conceptual View of Bleed Air Channels	19
Figure 7: Conceptual View of Single Temperature Control Channel.....	19
Figure 8: Conceptual View of the Outflow Channel.....	20
Figure 9: Photograph of Tank Supply Lines.....	22
Figure 10: Photograph of Supply Side of Test Rig	23
Figure 11: Photograph of Bypass and Heat Exchangers from Below	24
Figure 12: Photograph of Bypass and Heat Exchangers from Above.....	24
Figure 13: Photograph of Exhaust Side.....	25
Figure 14: Photograph of Entire Rig	26
Figure 15: Photograph of Actuator Controller Card.....	32
Figure 16: Photograph of Open and Closed Valves.....	32
Figure 17: Rack Mounted Data Acquisition System and Workstation	38
Figure 18: Front Panel Photograph of Terminal Box #1	40
Figure 19: Top Internal Photograph of Terminal Box #1	41
Figure 20: Back Panel Photograph of Terminal Box #1	42
Figure 21: Front Panel Photograph of Terminal Box #2	43
Figure 22: Top Internal View of Terminal Box #2.....	44
Figure 23: Back Panel Photograph of Terminal Box #2	44

Figure 24: Sample SIMULINK Signal Analysis Subsystem Block	46
Figure 25: RTD Channel 11 Curve Fit: 1 mA Excitation	48
Figure 26: RTD Channel 12 Curve Fit: 1 mA Excitation	48
Figure 27: RTD Channel 3 Curve Fit: 1 mA Excitation	48
Figure 28: RTD Channel 4 Curve Fit: 1 mA Excitation	48
Figure 29: SIMULINK Overall Control System	64
Figure 30: SIMULINK NI PCI-6034E Data Acquisition.....	65
Figure 31: SIMULINK NI PCI-67044 Excitation.....	67
Figure 32: SIMULINK Scope Subsystem Overview	67
Figure 33: Control System Demonstration: Varying Flow with Constant Pressure, Flow Plot	69
Figure 34: Control System Demonstration: Varying Flow with Constant Pressure, Pressure Plot	69
Figure 35: Control System Demonstration: Constant Flow with Varying Pressure, Pressure Plot	71
Figure 36: Control System Demonstration: Constant Flow with Varying Pressure, Flow Plot	71
Figure 37: Control System Demonstration: Varying Flow and Pressure, Flow Plot	72
Figure 38: Control System Demonstration: Varying Flow and Pressure, Pressure Plot	72
Figure 39: Bleed Line Diagram with Notation	74
Figure 40: Diagram of a Thermal Flow Sensor	75
Figure 41: Flow Sensor Model Calibration Curve	81
Figure 42: Thermal Flow Meter Response to a Mass Flow Step Change.....	82
Figure 43: Diagram of an Orifice Plate Flow Meter.....	83
Figure 44: Dynamic Response of Thermal and Orifice Plate Flow Sensors.....	86
Figure 45: Diagram of Physical Hybrid Sensor	87
Figure 46: Model Results for Hybrid Sensor, Step from 0.002 kg/s to 0.5 kg/s.....	90
Figure 47: Model Results for Hybrid Sensor, Step from 0.5 kg/s to 0.002 kg/s.....	91

Figure 48: Simplified Flow Resistance Sketch	93
Figure 49: Change in Pressure Drop Coefficient due to Bypass Valve Position	98
Figure 50: Effects of Bypass Valve Position on Flow Calculation	98
Figure 51: Hybrid Sensor 0.002 kg/s to 0.5 kg/s	99
Figure 52: Hybrid Sensor 0.5 kg/s to 0.002 kg/s	100
Figure 53: Effects of Bypass Valve Position on Hybrid Sensor	101
Figure 54: Sensor Configuration for Experiments	103
Figure 55: Pressure Drop across the Bottom Bleed Channel	104
Figure 56: SIMULINK Pressure Drop Calculation	106
Figure 57: Command and Actual Valve Positions for Omega Flow Sensor Response Test	107
Figure 58: Omega Flow Response Test Results	108
Figure 59: Omega Flow Sensor Step Response	109
Figure 60: Varying Flow with Constant Pressure, Thermal Flow Sensor Plot	110
Figure 61: Command and Actual Valve Positions for Thermal Flow Sensor Response Test	111
Figure 62: Thermal Flow Response Test Results	111
Figure 63: Thermal Flow Sensor Step Response	112
Figure 64: SIMULINK Hybrid Sensor Subsystem	113
Figure 65: Hybrid Algorithm Flow Response Test	114
Figure 66: Hybrid Flow Sensor Step Response	115
Figure 67: Flow Control: Thermal Flow Sensor Response	117
Figure 68: Flow Control: Pressure Drop Flow Calculation Response	118
Figure 69: Flow Control: Hybrid Flow Sensor Response	118
Figure 70: Decreasing Step Response: Hybrid Flow Sensor	119
Figure 71: Run 3 Outflow Control with Hybrid Sensor Feedback	120

1 Introduction

This chapter introduces the overall objectives, topics, and background information of this thesis. In addition, this chapter provides an overview of prior research performed at the Systems and Control Laboratory of Ryerson University and a survey of publications relevant to this study. The overall organization of this thesis begins with an introduction and literature review, and then discusses the test rig design and construction, before outlining the theoretical algorithm behind the hybrid mass flow method. Experimental results will follow which include calibration results for the sensors, control system performance, and outputs of the hybrid mass flow algorithm. Finally, conclusions and recommendations for future work will close out this thesis.

1.1 Objectives and Organization

The three primary objectives that form the framework organizing this thesis are listed below:

1. ***Development of a Pneumatic System Test Rig.*** The rig is intended to be used for the study of controls, diagnostics, prognostics, and health management for aircraft bleed air systems. The rig design is to be based on previous designs and incorporates lessons learned from those designs. Also, the rig should accommodate different types of research so that it may be used for many years to come. Four tasks were identified to complete this primary objective.
 - ***System Design.*** The requirements and overall design of the test rig were planned based on current and future research needs, with input from the principal investigator, peers, and technical staff. This design was approved by the principal investigator and specified to the contractors.
 - ***Detailed Design.*** This task included the selection of major components and the design of terminal boxes for the instrumentation packages by the author with supervision from the technical staff of Ryerson University.
 - ***Construction.*** The test rig was built and certified by the selected contractors. The instrumentation package was constructed by the author and technical staff at Ryerson University.

- **Calibration.** After installation, all sensors and actuators were carefully calibrated by the author and technical staff of Ryerson University.
- 2. **Development of a Hybrid Flow Sensor Algorithm.** This algorithm was developed as a dynamic weighted average between a fast responding pressure drop flow calculation used during transients and a more accurate thermal flow measurement during steady state. The intention was that this algorithm would lead to more accurate mass flow estimation as well as improved flow control by measuring changes in flow faster.
- 3. **Validation of the Test Rig and Hybrid Flow Sensor Algorithm.** This involved the actual experiments performed on the rig. Initial tests were performed to determine sensor calibration and the basic control system of the test rig. Tests of the hybrid flow sensor algorithm were also performed with satisfactory results.

1.2 Background Information

This thesis requires an understanding of two major aircraft systems as follows:

1. **Bleed Air System**
2. **Environmental Control System**

Furthermore, it requires familiarity with the operation of the following five different types of sensors:

1. **Thermocouples**
2. **Resistance Temperature Detectors**
3. **Pressure Sensors or Strain Gauges**
4. **Thermal Mass Flow Meters**
5. **Potentiometers**

Finally, a simple overview of how sensor fusion ties in all sensors and system functions will be presented.

Note that throughout this thesis, units will predominantly be imperial. This is due to the fact that most of the components were purchased from the USA, and that various standards dealing with the piping are imperial. However, metric has been used where convenient, such as the theoretical section.

1.2.1 Bleed Air System

A wide variety of aircraft systems primarily use pneumatic power, and the turbofan engine is the main pneumatic power source on modern aircraft. The bleed air system connects the pneumatic power users to the source by bleeding air from the turbofan engine compressor, conditioning the air to a safe pressure and temperature, and transporting it to the user.

The most significant difficulty with using bleed air is the variability of the air source at different turbofan power levels. During ground idle and flight idle, the turbofan may not be producing enough pressure or temperature at a specific location of the compressor to power the dependent systems. However, at the same location during takeoff, the turbofan may be producing too much pressure or too high a temperature. Typically, the pressure and temperature during ground idle at the compressor exit are 345 kPa and 180°C respectively, but during takeoff the same location can experience a pressure and temperature of 2830 kPa and 540°C.

To adapt to this inherent variability, air is bled from different compressor stages using multiple bleed-off valves. Air is bled at a higher pressure and temperature than required, and then conditioned using a pressure-reducing shut-off valve and a pre-cooler to the required working level. The working levels are approximately 275 kPa absolute and 100°C.

The pressure-reducing shut-off valve is the component used to restrict downstream pressure to approximately 275 kPa. Typically, the valve is pneumatically operated, electrically controlled, and styled as a butterfly valve.

Immediately downstream of the pressure-reducing shut-off valve is the pre-cooler. Typically, the pre-cooler is a cross-flow heat exchanger, which uses the airflow bled from the turbofan bypass as cooling air. After the pre-cooler, valves direct the conditioned bleed air to the users, such as the Environmental

Control System (Moir & Seabridge, Aircraft Systems: Mechanical, Electrical, and Avionics Subsystems Integration, 2008)(Moir & Seabridge, Civil Avionics Systems, 2003).

1.2.2 Environmental Control System

Passengers and crew should be kept comfortable and safe during their flight; achieving this is the responsibility of the environmental control system (ECS). The ECS primarily controls cabin pressurization and temperature control, though many other subsystems may fall under its domain, such as anti-icing or anti-misting. Modern aircraft typically condition bleed air further using air cycle machines to achieve the required cabin temperature and fresh air flow. Outflow valves are used to control the pressure inside of the cabin of aircraft with open environmental control systems.

The ventilation requirements specified by the Canadian Air Regulations (CAR) for normal operating conditions are found under CAR 525.831 Ventilation. To paraphrase this section, the aircraft should be designed to deliver at least 0.55 pounds of fresh air per minute for each occupant of the aircraft, or 0.0042 kg/s for each occupant. In addition to ventilation requirements CAR 525.831 also includes cabin temperature limits that vary with exposure time. CAR 525.841 Pressurised Cabins defines how all pressurized cabins are to be built, with a maximum allowable pressure altitude of 8,000ft, or 2,400m, at maximum altitude of the aircraft at normal operating conditions.

Air cycle machines are primarily used to cool the air and reduce pressure. However, there are many different configurations of the air cycle machine that may be used to achieve this, but the bootstrap system is the most prevalent.

In the most basic bootstrap system, bleed air is passed through a compressor which pressurizes and heats the air. The air is then cooled in a heat exchanger by ram air, before being passed through a turbine. The turbine is mounted on a common shaft with the compressor, the compressor serving as a load to the turbine. Air expands across the turbine, resulting in chilled low pressure air. A bypass valve

allows a small amount of hot bleed air to reheat the chilled air, which has just expanded across the turbine, to the level required by the cabin.

Optional components to the basic system depend heavily on the aircraft, and may include some of the following items.

- ❖ **Multiple Stages.** This provides a stepped decrease in temperature for larger airflows and uses the extracted heat and pressure more efficiently.
- ❖ **Ram Air Fan.** This fan is mounted on the same shaft as the turbine and compressor. It draws air across the heat exchangers in the ram air channel for cooling during ground operation.
- ❖ **Jet Pump.** This operates on the same principle as the Ram Air Fan, except it uses a nozzle to blow bleed air downstream of the heat exchangers drawing cool air over the heat exchangers.
- ❖ **Water Extractor.** This component dehumidifies the air upstream of the turbine which prevents the turbine from icing and extremely moist air from entering the cabin. The water extracted is then sprayed on the heat exchangers inside the ram air channel to provide further cooling.

The bootstrap system contains many inefficient processes, not only involving the reductions of pressure and temperature of the bleed air, but also causing increased drag due to the ram air cooled heat exchangers and power loss from large quantities of air being bled from the engines. With rising fuel costs, this is one of the systems being studied to improve aircraft efficiency (Moir & Seabridge, Aircraft Systems: Mechanical, Electrical, and Avionics Subsystems Integration, 2008).

1.2.3 Sensors

Both the bleed air and the environmental control system use a variety of sensors. Likewise, the new test rig also has incorporated a range of sensors. These sensors measure quantities such as temperature, pressure, flow rate, and valve position.

1.2.3.1 Thermocouples

An electric potential can be generated when two wires of different materials are connected at both ends with each junction experiencing a different temperature. This is called the Seebeck effect, and it forms the basis of how thermocouples operate. The amount of voltage generated may not be the same as that which is measured due to losses in the connecting wires. Therefore, thermocouples must be calibrated, since thermocouple installation plays a direct role in the final measured output.

Formerly, thermocouples were referenced to a thermojunction mounted in an ice bath (this process is outlined by Doebelin (Doebelin, 1966)). However, new room temperature methods have been developed that allow the reference junction to be incorporated into the signal conditioner or replaced entirely by different temperature sensing means usually mounted on an isothermal block.

1.2.3.2 Resistance Temperature Detectors

The predictable change of resistance in a conductor as temperature increases forms the basis of resistance temperature detectors. Semiconductor temperature sensors operate on a similar principle and are known as thermistors. A polynomial is used to determine the temperature based on the measured resistance. For modern instrumentation systems, a four wire constant current system is commonly used such that resistance variations of the lead wires do not affect the measurement (Doebelin, 1966).

The four wire configuration is now the most commonly used. A constant current flows through one pair of leads, while the other pair measures the voltage drop across the sensor. Lead resistance plays a small role in the final measurement since there is no current in the measurement leads. Keithley suggests a current of 1 mA or less to minimize self heating errors. Fortunately, self heating is minimized when the medium undergoing measurement flows past the sensor head (Keithley Instruments, Inc., 2007).

1.2.3.3 Pressure Sensors

Typical pressure transducers operate using strain gauges mounted on small flexible discs, or diaphragms, which are exposed to varying pressures. On one side of the diaphragm is the load pressure being measured and on the other side of the disc is either a vacuum or ambient pressure. A vacuum will result in an absolute pressure measurement, whereas ambient pressure will result in a gauge pressure measurement (Doebelin, 1966). Typically, pressure transducers are made containing the necessary signal conditioning inside of the sensor housing. (Keithley Instruments, Inc., 2007).

1.2.3.4 Thermal Mass Flow Sensors

There are many types of thermal mass flow sensors, but they all function in a similar manner. Typically, two platinum RTDs are exposed to a gas flow, one sensor is heated and the other is maintained at the current flow temperature. The power required to maintain a preset temperature difference between the two sensors indicates the mass velocity at a point or the total mass flow in a pipe, depending on the sensor design and calibration. Mass velocity is defined as the mass flow rate per unit area; thus, if the cross sectional area of the channel is known, then the total mass flow may be calculated (Olin).

1.2.4 Sensor Fusion

Some introductory work on sensor fusion and fault detection was performed by Day at Ryerson University in 2005 (Day, 2005). Sensor fusion focuses on combining sensor data into a common format with the goal of providing better information than the quality of the individual parts. Typically, this is performed across multiple measurements, but these measurements may be from the same sensor over time or from a multitude of sensors at the same instance in time.

There are several strategies for data fusion that are problem dependent. This application involves fusion across different sensors and attributes. Since pressure, temperature, and flow sensors measure different attributes of the same medium, this represents fusion across attributes. However, pressure

and temperature data may be used to find flow data, thus making another virtual flow sensor, and allowing data to be fused with respect to different sensors.

It is important to note that the sensors being considered have not faulted, but merely respond differently due to their calibration or individual operating characteristics. This is where sensor fusion can help form a complementary or redundant configuration that gives a more accurate response of what the measured medium is doing (Mitchell, 2007).

1.2.5 Previous Test Rigs

The first pneumatic test rig at Ryerson University was built by Chan in 2001. It was a two channel flow sharing rig built of plastic pipe. Flow rates and pressure drop along the rig were relatively low, on the order of 0.15 lb/s and 7 psig. A basic schematic of the two channel rig is shown below in Figure 1 (Chan, Design, Building, and Experiment on the Bleed Air Sharing Control System Emulation, 2001).

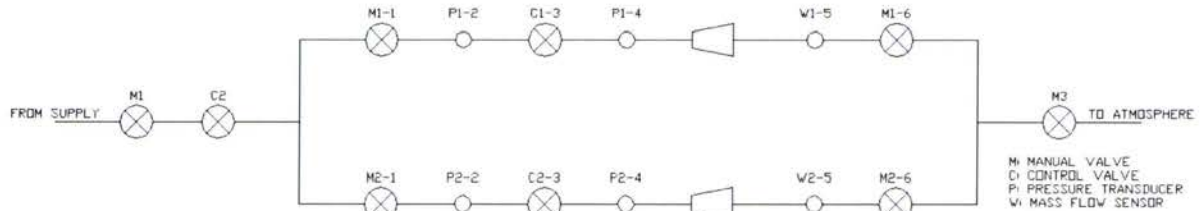


Figure 1: Two Channel Flow Sharing Test Rig Diagram

Bao used the two channel rig to develop a flow sharing algorithm (Bao, 2003), during this time Hardacre was adding an additional two channels to make a four channel flow sharing test rig (Hardacre, 2002). This allowed the master-slave approach to be validated across multiple slave channels. The four channel diagram is shown below in Figure 2.

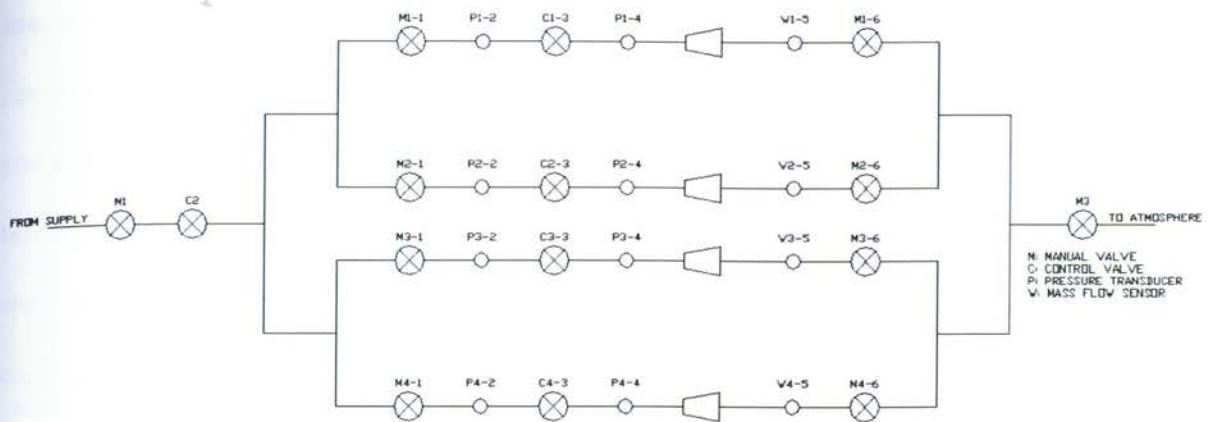


Figure 2: Four Channel Flow Sharing Test Rig Diagram

Focus shifted from flow sharing to optimal temperature control and heat exchanger analysis under Hodal, Shang, and Shah. A new test rig was built for temperature control, and the ability for flow sharing was lost with the disassembly of the four channel rig. The introduction of inline air heaters required the use of steel pipe. A diagram of the temperature control rig is shown in Figure 3 (Hodal, 2005)(Shang & Liu, 2007).

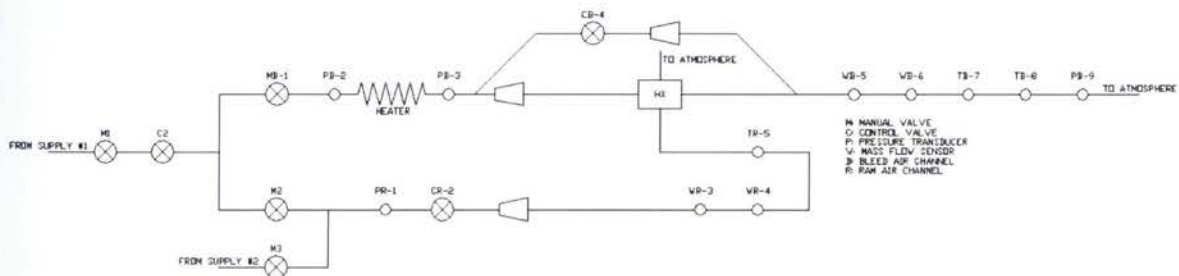


Figure 3: Temperature Control Test Rig Diagram

Issues concerning the old rigs focused both on safety and experimental performance. The plastic pipe was acceptable for simple flow sharing tests, but with the application of higher temperatures the plastic pipe could easily lose strength, which forced the transition to steel pipe on the temperature control rig. The temperature control rig was built solidly, but was plagued by sensor placement issues as the topic of research shifted. This resulted in poor installation of sensors, which were subject to leaks. To avoid the

safety issue of leaks, no exhaust restrictions were installed in order to keep the channel at a low pressure. Additionally, the bypass valve was not located in the main flow channel, so its effectiveness was reduced since the easiest flow path was directly through the heat exchanger. Finally, the heat exchanger fouling test performed by Shah had permanently damaged the old heat exchanger.

1.3 Literature Review

Bleed air research has been relatively stagnant in recent years, and most of the energy has been devoted to determining if new electric systems will be able to perform more efficiently than established bleed air systems. However, some modeling work was done by Elangovan on pneumatic ejectors, which are a form of jet pump. Elangovan's work modeled the supporting valves and ducting in the bleed air system to develop a control system that would modulate the valves and ejector flow to achieve cooling as necessary across the pre-cooler (Elangovan & Brushwood, 1985). This is similar to the work done at Ryerson University involving ram-air plus bypass temperature control schemes.

Research at Ryerson University began with the development of flow sharing by Bao and Hardacre (Bao, 2003) (Hardacre, 2002). This research was performed on the rig initially designed by Chan (Chan, Design, Building, and Experiment on the Bleed Air Sharing Control System Emulation, 2001). Also, a mass flow sensor algorithm was developed by Jiang, and later a digital algorithm by Yiu (Liu, Bao, Lam, & Jiang, 2005)(Jiang, Liu, & Jiang, 2005) (Yiu, 2004). Hodal started research on heat exchanger modeling, and this was furthered by Shang in the area of temperature control. The temperature control scheme used by Shang involved modulating flow in the ram air channel and heat exchanger bypass channel. This allowed for optimal control of the outlet temperature during transients (Hodal, 2005)(Shang & Liu, 2007). Most of the above research has played a role in the development of the new rig. This research has culminated in a patent for the flow sharing algorithm (Liu & Lam, 2003).

Many companies and universities are researching electric systems to meet the More-Electric Aircraft concept. Ensign has been performing analysis on an electric environmental control system for Cessna business jets for several years (note that in many cases the environmental control system includes the bleed air system). Essentially, Ensign suggests the replacement of the traditional bleed air system with electric compressors, so that the engine only needs to produce thrust and electricity. Electric compressors will provide pressurization and conditioning through traditional air cycle machines, and heating grids will meet anti-icing requirements (Ensign & Gallman, Energy Optimized Equipment Systems for General Aviation Jets, 2006)(Ensign, AIAA 2007-1395, 2007)(Ensign, Sensitivity Studies of Electric Systems on Business Jet Range, 2008).

Furthermore, the More-Electric Aircraft concept is undergoing exergy¹ analysis by several other authors to determine if it actually is more efficient. Slingerland states that the largest difficulty in comparing bleed air systems to electric systems is the inability to compare the off-takes directly. However, through the use of a gas turbine simulation program Slingerland concludes that electrical engine off-takes are less efficient than pneumatic off-takes, but the electrical systems operate much more efficiently resulting in a 2% improvement of thrust specific fuel consumption over the equivalent pneumatic system (Slingerland & Zandstra, 2007).

The effects of bleed air extraction on thrust were measured by NASA on an F404-GE-400 turbofan engine used in the F/A-18 High-Alpha Research Vehicle. This research found that at military power, a 1% increase of bleed flow results in a 2% decrease of thrust. However, this flow was to be used for flight

¹ "Exergy is defined as the maximum work obtained by an energy carrier, when it is brought into equilibrium with the environment, through reversible processes with common components of the environment." (Pellegrini, Gandolfi, & Lima da Silva, 2007)

control purposes at a high angle-of-attack rather than the environmental control system (Yuhas & Ray, 1992).

Buss brings an interesting viewpoint to the debate concerning electric system performance compared to bleed air system performance. This viewpoint involves the aircraft type and the usage of the aircraft as an entire system. Most aircraft can be loosely classified into transport, patrol, or fighter classes. Each class has a vastly different set of requirements to meet, and different possible solutions to meet these requirements which are explained below:

- ❖ **Transport Aircraft.** Due to the large number of people on board, these aircraft have very large fresh air and pressurization requirements. The current air cycle system being used is considered optimum, with potential savings to be found in the improvement of bleed air systems or a switch to electric compressors.
- ❖ **Patrol Aircraft.** Due to the large amount of high density electronic equipment on board, air conditioning would be most efficiently handled by a vapor cycle system. However, for the small amount of air required for fresh air and pressurization, the normal bleed air system could be used.
- ❖ **Fighter Aircraft.** It is difficult to determine which method is most efficient due to the dependency on the actual aircraft design and heat rejection requirements.

In overview, Buss states that the environmental control system design is highly subject to the mission of the aircraft, and that the method to be used should be evaluated for each aircraft (Buss, 1984).

Simulation of an environmental control system was performed by Eichler, but very little is mentioned about the actual method used. Look-up tables and correction values seem to be heavily used to force the simulation to match the actual test system (Eichler, 1975).

Sensor fusion has typically been used in imaging fields with multiple sensors of the same type employed over a period of time (Rathburn & Washburne, 1993). Similar techniques have been used to determine the location of flow reattachment after a separation due to a step in the flow. This method used an

array of flush mounted pressure sensors and interpolation of the data to find the reattachment point (Humphreys & Culliton, 2008). With respect to aircraft, sensor fusion has been increasingly used for positioning of unmanned aerial vehicles. For vertical positioning, the output of a laser altimeter was fused with data from a radar altimeter to give a more accurate altitude reading to an unmanned aircraft (Accardo, Esposito, Cimmino, Moccia, Ciniglio, & Corrado, 2004). For horizontal positioning, a method of fusing data from the Global Positioning System with the inertial navigation system data has been developed (Jarrell, Gu, Seanor, & Napolitano, 2008).

1.4 Purpose

The primary purpose of this thesis was to develop a flow sharing and temperature control test rig. The new rig was intended to be able to merge the two previously studied topics with more flexibility in sensing and control. Additionally, it was intended to provide a solid record of the individual sensor calibration used by the SIMULINK control system. Key research in this thesis involved the development of a hybrid sensor algorithm that was intended to have the rapid response of a head loss flow meter, such as an orifice plate flow meter, but the steady state accuracy of a thermal flow sensor. Experiments were conducted to investigate the performance of the hybrid algorithm on the actual system and to demonstrate how the algorithm improved control performance of the system.

2 Test Rig

In this section, the overall design and operation of the test rig is presented. In addition, this section describes the requirements of the new test rig, the finalized design, and outlines some of the issues encountered during construction. Major components, sensors, and the control system are also explained.

2.1 Requirements

The purpose of the test rig is to provide a reconfigurable platform to perform experiments combining past research of flow sharing and temperature control with new research on sensor fusion, analytical redundancy, and prognostics. The new test rig shall have two temperature control channels that exhaust into a load tank. The load tank will have a single controllable outflow channel, and the two channels will be individually controllable and decoupled to allow for flow sharing. This setup shall allow for simultaneous flow, temperature, and pressure control in the load tank. Pressure control of a load tank has not been included in previous test rigs since they were exhausted directly to ambient conditions. Besides accommodating flow sharing, a twin channel rig allows for physical redundancy and flexibility in new research fields such as fault detection, identification, and accommodation.

Fixed operating conditions shall consist of a maximum working pressure of 90 psi, or 620 kPa, with a maximum temperature of 200°F, or 366 K, downstream of the heater.

This rig shall be registered with the Technical Standards and Safety Authority (TSSA) of Canada. Hearing protection will be required in the lab. Other safety concerns involve pressure release valves on the tanks, and upper temperature limits placed on the heaters, and programmed into the heater controllers.

Wiring and connections for sensors shall be properly shielded, with all shields grounding at a common location inside of the junction box. The ground should be isolated from the rig to avoid ground loops. All wiring diagrams shall be recorded in this thesis, and a copy kept in the testing facility.

Sensor calibration will be performed on the rig with the process and results recorded in this thesis.

2.2 Design and Construction

The overall design was checked and stamped by the engineering contractor Teng and Associates Inc. (Mississauga, Ontario). The drawings were registered with the TSSA, and the rig itself was certified by the TSSA. Lemico Liquids (Mississauga, Ontario) was the subcontractor who built and installed the rig at Ryerson University. Lessons learned from previous test rigs were as follows:

- ❖ **Two Channels.** This allowed flow sharing capabilities and redundant channels for fault simulation and experimentation.
- ❖ **Straight through Heat Exchanger Bypass.** One of the primary lessons learned from the temperature control rig was low pressure drop across the heat exchanger reduced effectiveness of the bypass control valve. A mechanically linked T valve and straight through bypass was included in the new rig to improve bypass flow control.
- ❖ **Common 2" Diameter Piping.** This allows for simpler building and modeling due to reduced diameter changes.
- ❖ **Supply and Load Tanks.** The supply tanks were added to allow for increased test duration. They also effectively increased available pressure since the pressure can be maintained in the lab rather than the supply room; thus, experiments are not affected by pressure losses due to air flowing to the rig from the supply room. The load tank was also a new addition that allowed for new research in pressurization and further validation of past flow control schemes.
- ❖ **Butterfly Valves.** Previous control schemes were intended to be used with butterfly valves, but small diameter ball valves were used instead. Most sources agree that butterfly valves function better as throttling devices (Smith & Zappe, 2004).

- ❖ **Common Sensor Pads.** This rig must be reconfigurable. By using common sensor pads and machined bushings, sensors can be moved virtually anywhere on the rig easily. However, consideration was given to how the sensors operate, since some sensors do not perform well around obstructions.
- ❖ **Calibration.** Information on the calibration of old sensors and wiring diagrams of instrumentation are difficult to find for previous rigs, if they exist at all. Calibration and sensor performance has been taken under careful consideration in the design and construction of the instrumentation package for this rig. The calibration method used, equipment, and results were recorded so that they may be replicated in the future as necessary.

The following design was delivered to Teng and Associates to be revised to meet TSSA certification requirements and design of structural supports. The drawings were modified as needed and stamped by Teng and Associates before being registered with the TSSA. The official drawings are reproduced in Appendix A.

Figure 4 shows an isometric view of the test rig as it was modeled and presented to Teng and Associates in December 2008. As can be seen, three air tanks were used, two for supply and one for load. Between the supply and load tanks are the primary 'bleed' channels, which are heated and split between the bypass and heat exchanger lines before merging and exhausting into the load tank. The heat exchanger is cooled by the 'ram air' channels, which like the outlet channel are exhausted directly to the surroundings. The ram air channels are supplied by either the building air supply, or the supply tank of the opposite bleed channel. Specifically, the right tank provides air for the top bleed air channel and the lower ram air channel, whereas the left tank provides air for the bottom bleed air channel and top ram air channel. This was done to completely decouple the air sources, and provide longer duration running for temperature control tests.

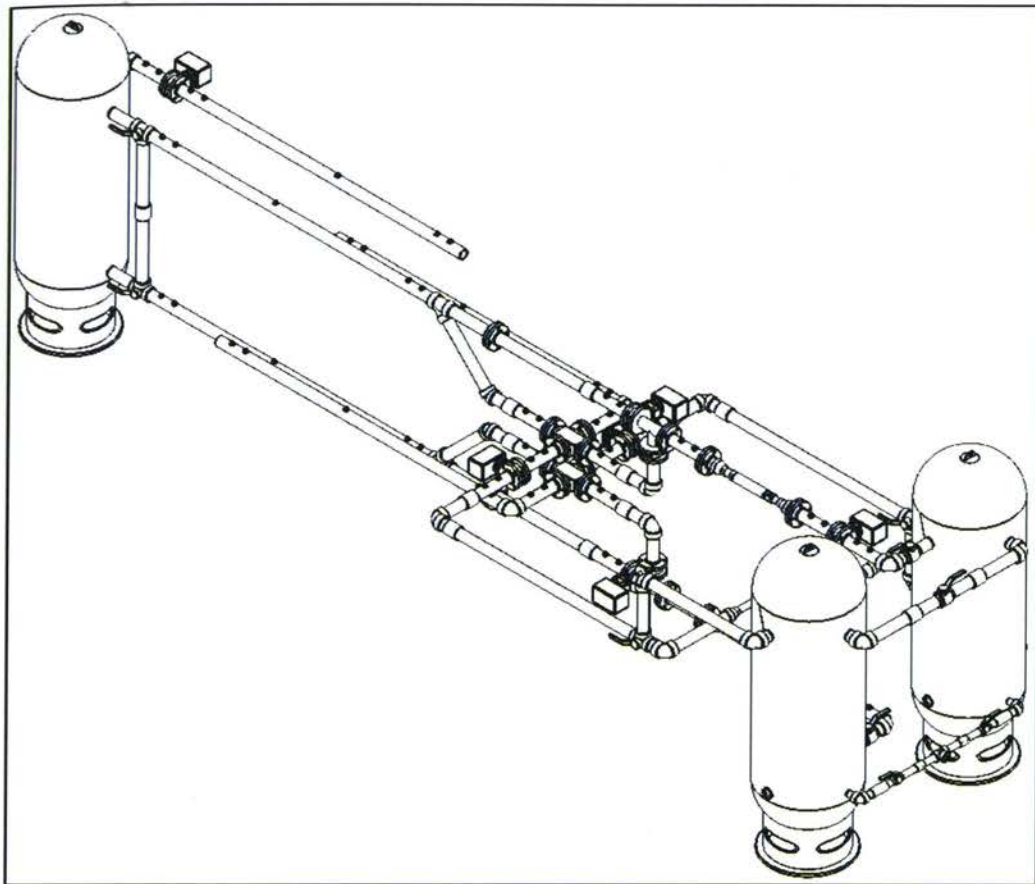


Figure 4: Conceptual Isometric View of New Test Rig

Each section of the rig will now be discussed and major components labeled. First is the supply end, which consists of a 1" pipe split by a T before being plumbed into the two laboratory supply tanks. Manual and check valves are used to allow filling of a single tank, and not allow cross flow between tanks as they are emptied during tests. If cross-flow is required for a test, the cross-flow valve may be opened. The location of these components is labeled in Figure 5.

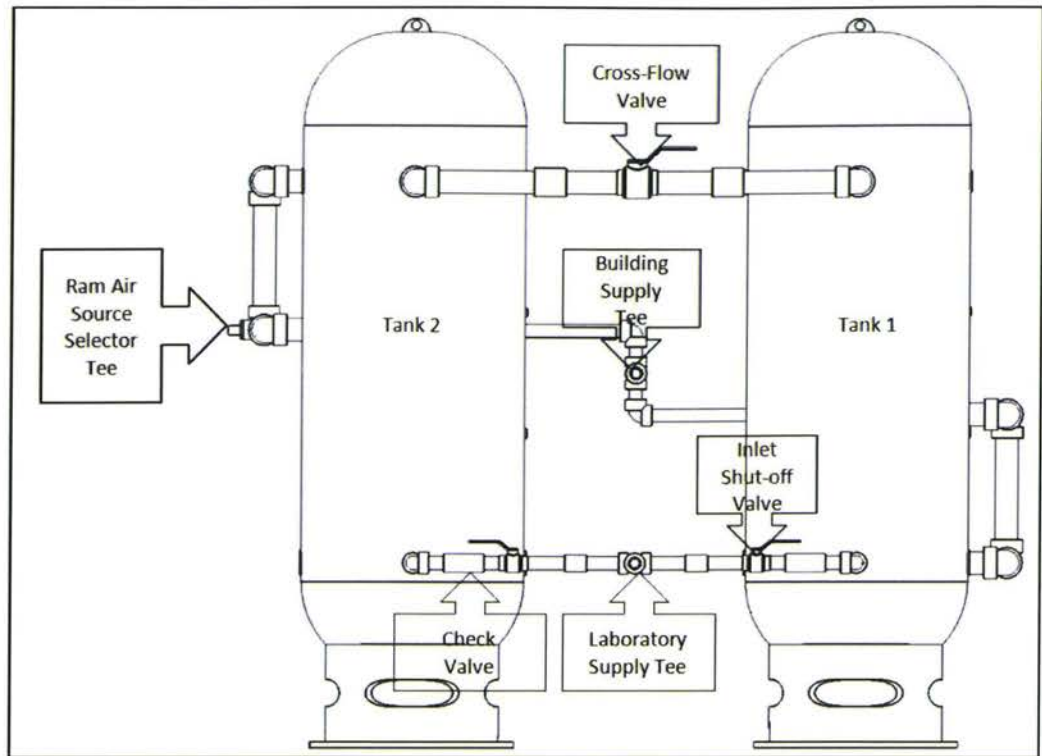


Figure 5: Conceptual View of Supply Lines and Tanks

After the supply tanks, air would either enter the bleed air or ram air channels. The bleed channel leaves its respective tank via manual valve followed by a 90° elbow. An electrically actuated butterfly valve is used to throttle the flow in the channel. After the main control valve, air is heated before being diverted through the heat exchanger. The Tee butterfly valve is electrically actuated and set to normally close off the bypass line. The air is cooled passing through the heat exchanger, before merging with the bypass flow and entering the downstream pipe. A cross-flow pipe is used to divert both flows to the same channel for stronger coupling effect if it is required. However, normal operation would have the flows being exhausted directly into the load tank. Figure 6 depicts the bleed air channels, along with their heat exchanger and bypass lines, and other major components. Threaded connections are used throughout the rig in conjunction with flanged connections around components that may need occasional servicing or replacement.

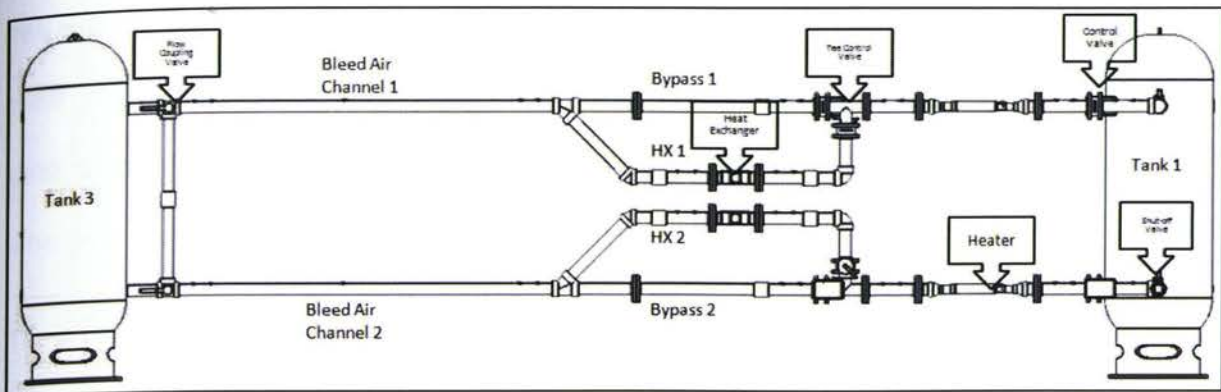


Figure 6: Conceptual View of Bleed Air Channels

The two bleed air channels also form the main flow sharing channels of the rig. The ram air channels are used to complete the temperature control requirements of each channel. Supply for the ram air channel can be from either the laboratory tanks or the building air supply. Flow is controlled via butterfly valve, and is passed directly through the heat exchanger before being exhausted to the surroundings. This is shown in Figure 7.

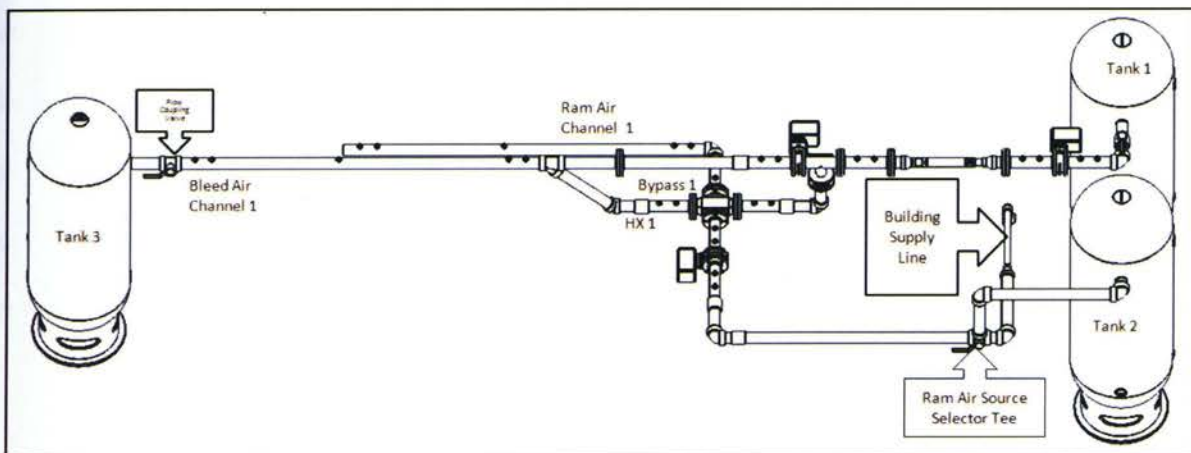


Figure 7: Conceptual View of Single Temperature Control Channel

Also obvious in Figure 7 is the decoupled nature of the temperature control channels. The bleed air channel and ram air channel each are supplied by a separate tank. Optionally, the ram air may be supplied by the building rather than the laboratory. It is arranged such that Bleed Air Channel 1 (BA1) is

supplied by Tank 1, and Bleed Air Channel 2 (BA2) is supplied by Tank 2. Also, Tank 1 supplies Ram Air Channel 2 (RAM2), and Tank 2 supplies Ram Air Channel 1 (RAM1), as shown in Figure 7. The final channel is the Outflow Channel (OC). The OC control valve affects the pressure in Tank 3 by controlling the outflow rate. It is shown below in Figure 8.

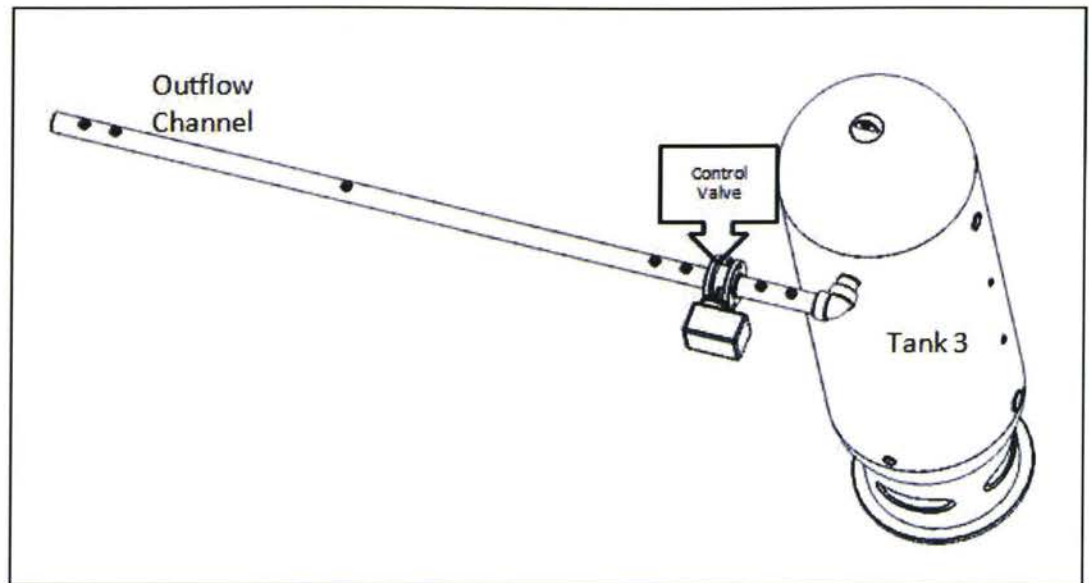


Figure 8: Conceptual View of the Outflow Channel

There is a high part commonality that was intentionally built into the rig to simplify construction. Sensor pads were added to three specific lengths of pipe, the drawings for which are specified in Appendix A: TSSA Approved Drawings. The 86" pipe was designed to meet the installation recommendations for the FMA900 Series flow sensors which requires at least 20 diameters of pipe between an upstream elbow or branch and a flow sensor. Additionally, it is recommended that at least five diameters downstream of the pipe be made available. Therefore the 86" pipe was designed to allow for 40" of clear flow upstream of the flow sensor pad, and 30" downstream. The 30" downstream easily exceeds the required 5 diameters, but it also allows for an additional flow sensor to be mounted in the channel for calibration or redundancy if the research topic demands.

The 12" pipes were simply intended to be used as a general means of adding more sensor positions to the rig, particularly around components of interest, such as the valves and heat exchangers. This was done to avoid the problem of not having the necessary sensor positions that plagued previous rigs whenever the research focus was shifted.

The 8" pipes were late additions, but are intended to provide a mounting position for the RTDs just before Tank #3, as well as the primary temperature control points of the rig. However, the possibility also exists to mount a sensor to the side of the tank.

The pictures shown below were taken on July 30, 2009. All of the valves in the bottom channel are operational, as well as the outflow valve. No heaters have been mounted, and the top channel, and all ram air channels are awaiting actuator mounting. Figure 9 shows the air supply to the rig. Both supply lines are closed in this case. The "Lab" supply line is the normal source of air, and this line is filtered and may also be regulated. The "Building" supply is a backup source and may be used for ram air supply or an initial pressure charge for the tanks. The "Crossflow Valve" is used to allow equalized pressures in both supply tanks for single channel running and it is opened in the picture. The "Supply Valves" located at the bottom, are used to select which tank to charge. In this case, Supply #2, which charges Tank #2, is opened, whereas Supply #1 is closed. However, since the cross-flow valve is opened. Both tanks will be charged.

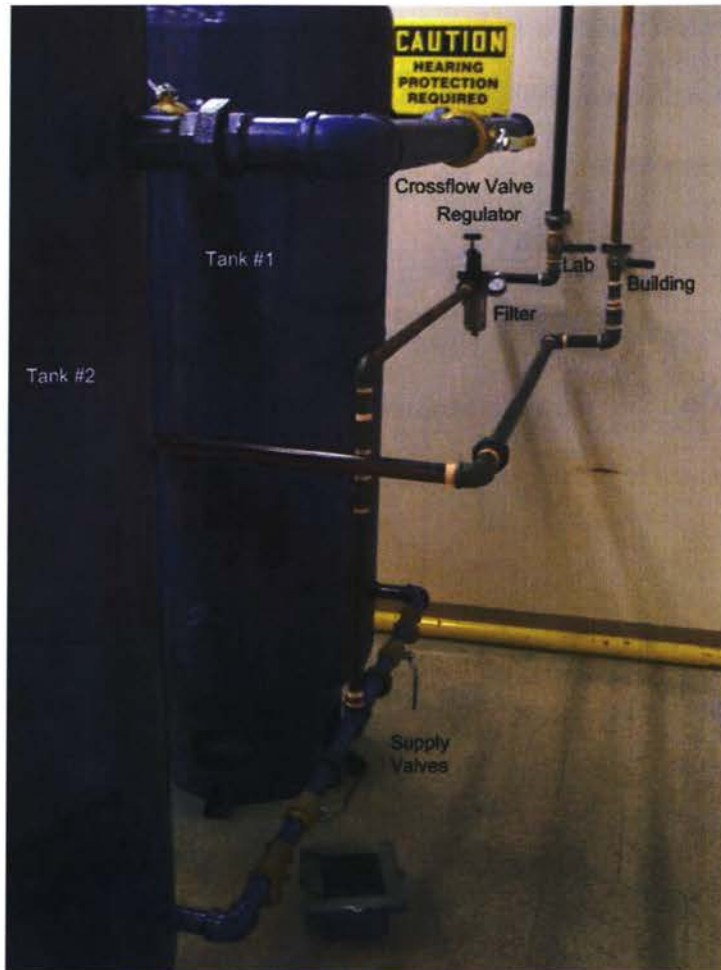


Figure 9: Photograph of Tank Supply Lines

Figure 10 is a picture from the middle of the rig, looking back towards the supply. The tee connection in the center of the photograph is where the building supply enters the rig. The tee valves, such as the "Ram Air Source Selector" allow for either the building supply or air from the tank to be used. "Ram Valve #1" is an addition that was not used in the initial drawings, it aids in completely isolating the supply tanks, rather than depending on the tee valves alone. The actuated valve shown is for controlling the airflow in the channel "Bleed #2" (BA2). The corresponding valve in channel "Bleed #1" (BA1) does not have an actuator mounted in this picture.



Figure 10: Photograph of Supply Side of Test Rig

Figure 11 is another photograph viewing back towards the supply, from closer to Tank #3. Here the ram air channels are clearly seen as well as the heat exchangers and bypass channels. The “Actuated Tee Valve” is located in the BA2 channel and will be used to direct airflow through or around the heat exchanger. This valve also has the actuator mounted. The valves intended to control the ram air channels do not have their actuators mounted. Figure 12 is a photograph of the opposite angle looking towards the load tank and more clearly showing the BA1 channel, as well as the RAM1 channel. At the exit of RAM1 is a reducing elbow. The elbow is intended to serve as a restriction as well as a means of directing flow downwards in a safe direction. Eventually, all of the exit elbows will be painted yellow as a high visibility caution.

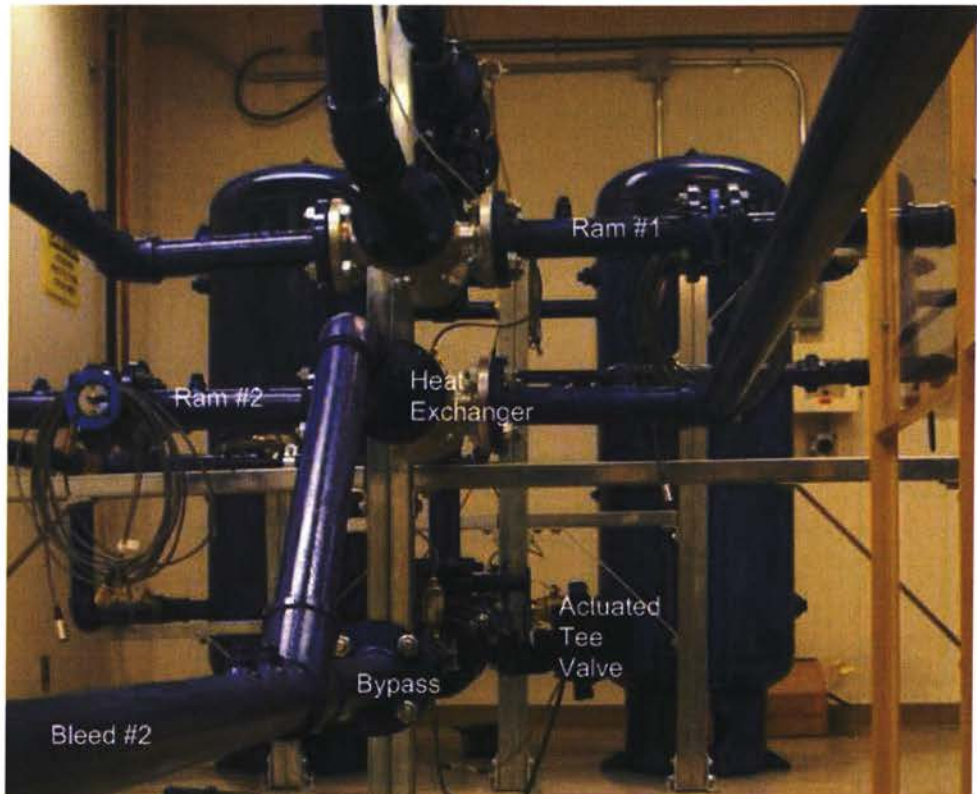


Figure 11: Photograph of Bypass and Heat Exchangers from Below

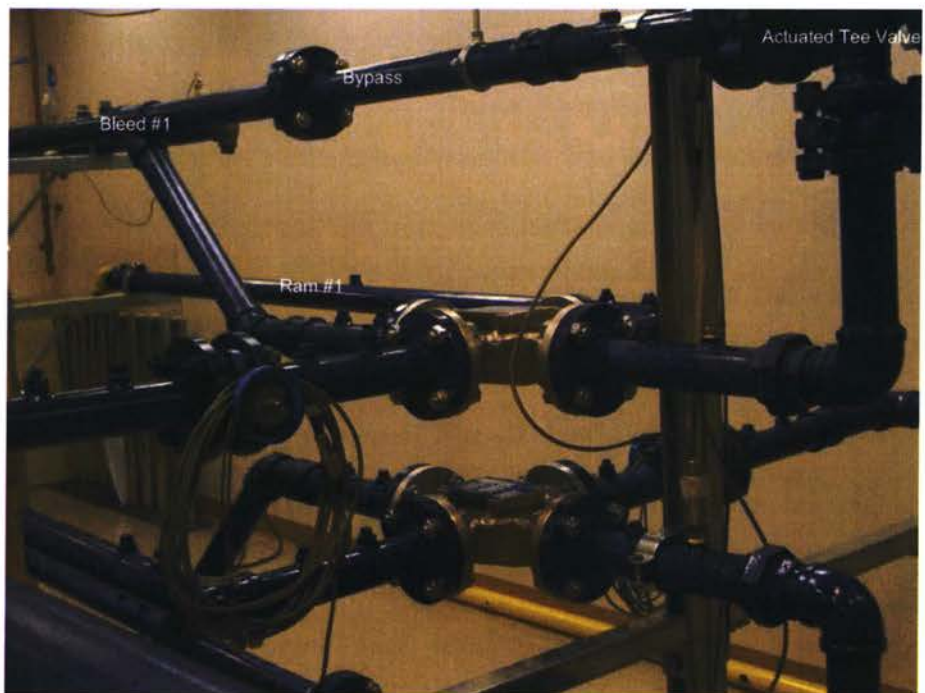


Figure 12: Photograph of Bypass and Heat Exchangers from Above

The exhaust end of the rig is shown in Figure 13. The “Outflow Control Valve” is operational, and the reducer elbow is shown at the exit. Additionally, a bushing has also been installed to further restrict the exit flow and provide back pressure. Sensors mounted in this channel are also visible. They are an Omega PX209 pressure sensors (Laval, Quebec) at the entrance and exit of the channel, with an Omega FMA905 (Laval, Quebec) flow sensor located in the middle.

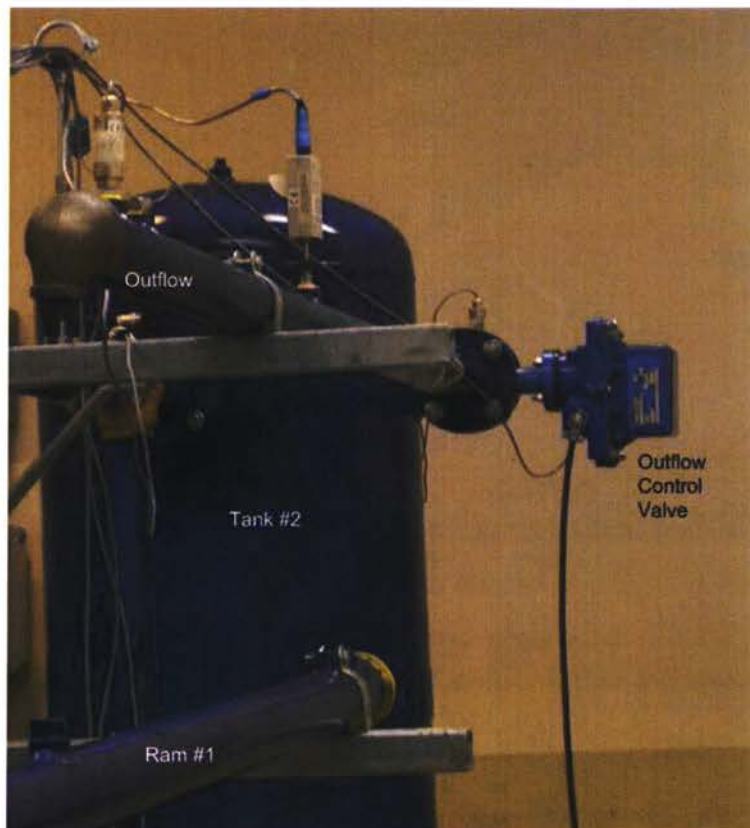


Figure 13: Photograph of Exhaust Side

An overall view of the rig and workstation is shown in Figure 14. As mentioned, the heaters and most of the actuators are not installed at the time this picture was taken. However, the bottom channel and outflow channel are operational for basic flow and pressure control research.

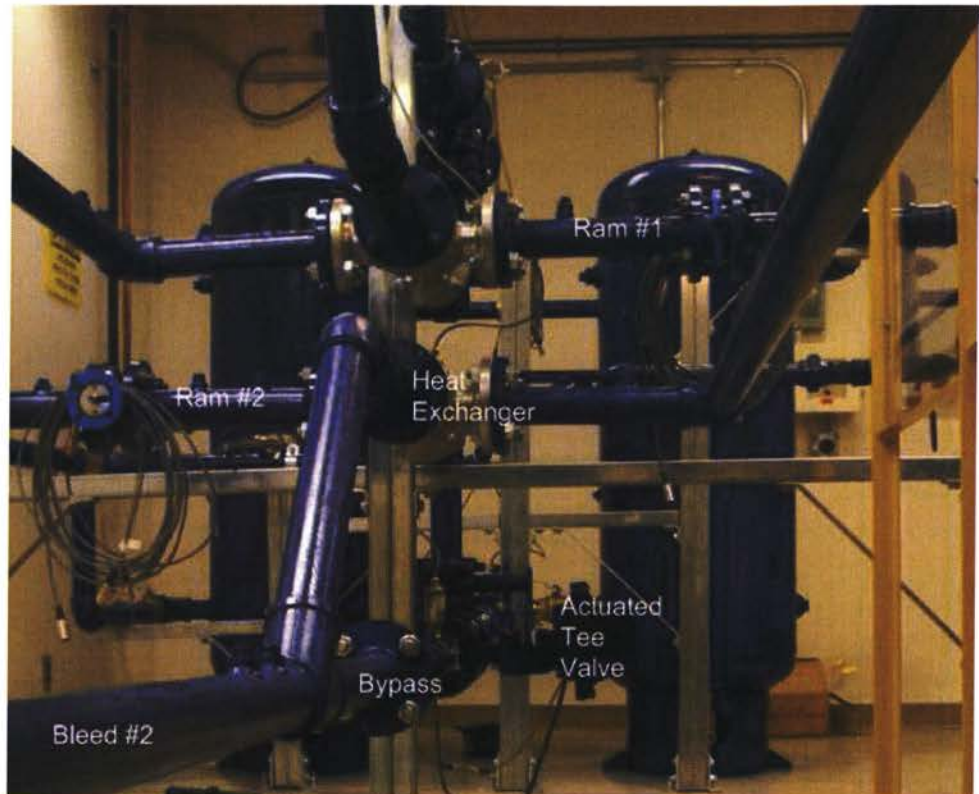


Figure 11: Photograph of Bypass and Heat Exchangers from Below

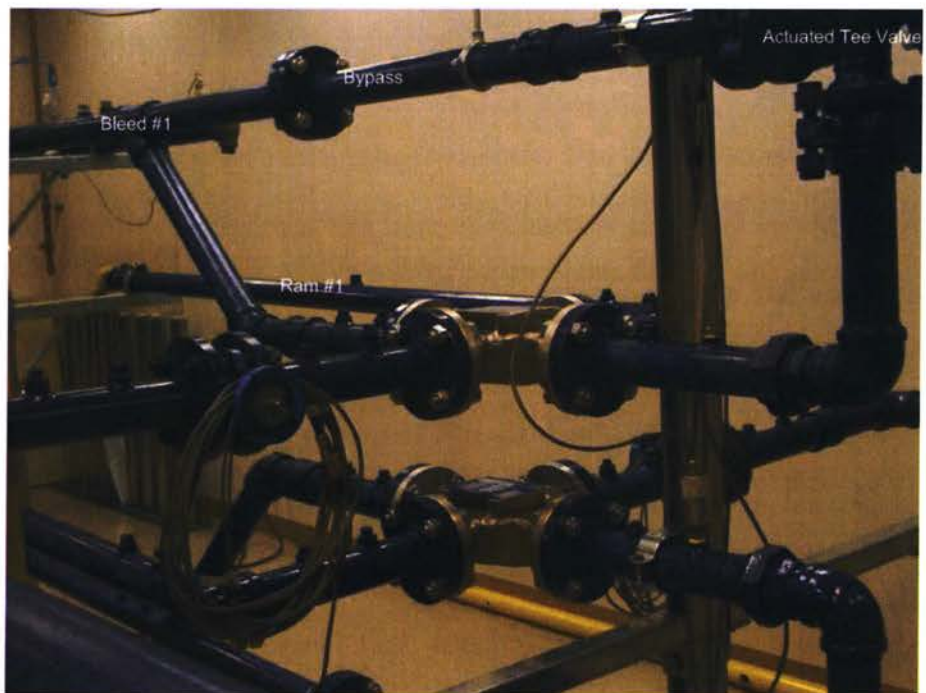


Figure 12: Photograph of Bypass and Heat Exchangers from Above

The exhaust end of the rig is shown in Figure 13. The “Outflow Control Valve” is operational, and the reducer elbow is shown at the exit. Additionally, a bushing has also been installed to further restrict the exit flow and provide back pressure. Sensors mounted in this channel are also visible. They are an Omega PX209 pressure sensors (Laval, Quebec) at the entrance and exit of the channel, with an Omega FMA905 (Laval, Quebec) flow sensor located in the middle.

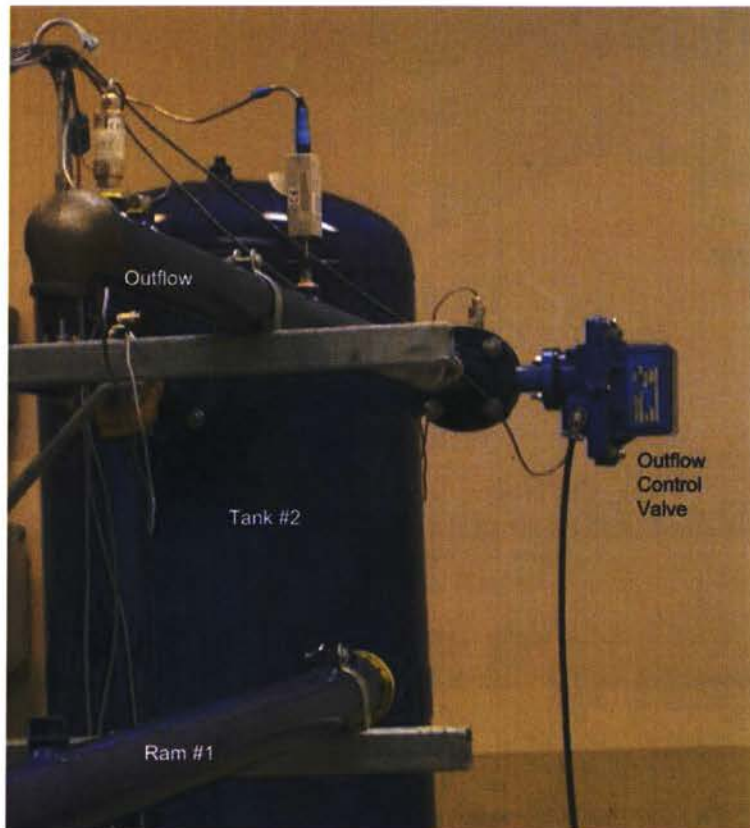


Figure 13: Photograph of Exhaust Side

An overall view of the rig and workstation is shown in Figure 14. As mentioned, the heaters and most of the actuators are not installed at the time this picture was taken. However, the bottom channel and outflow channel are operational for basic flow and pressure control research.



Figure 14: Photograph of Entire Rig

2.2.1 Major Components

The following sections highlight most of the major components of the rig. Component specifications and the reasons as to why a particular component was chosen are provided. For components with poor specifications, whatever information is known will be presented here, as well as any information that was assumed for testing or simulation. Where possible, this assumed information will be verified, and the results recorded here.

2.2.1.1 Tanks

Three new tanks have been incorporated into the new test rig. The two additional supply tanks complement the old tanks mounted in the supply room. According to Bao, each old tank had a volume

of approximately 51,300 in³, or approximately 220 gal. (Bao, 2003) The new tanks each contain 120 gal, so total storage capacity of the new rig is approximately 680 gal of air at 125 psi. The new tanks are able to hold air up to 200 psi, but the compressor seems to supply a maximum pressure of 125 psi. Besides increased supply, the new tanks were also intended to decouple the supply air by increasing the volume directly upstream of the main control valves. The three new tanks, part number A10049, were supplied from Steel-Fab Tanks (Oakville, Ontario). All of the tanks are equipped with drain valves, analog pressure gauges, and pressure relief valves which are set to 90 psig.

2.2.1.2 Heaters

The heaters chosen for this rig are the Farnam HT200 heaters with the Farnam Series 7550-A40 controllers. The 8.0 kW heaters are rated from 19.3 standard cubic feet of air per minute (SCFM) to 100 SCFM, and have a maximum exhaust temperature of 1300°F. This exhaust limit will be reduced to 200°F maximum on the rig, and the flow switch will be used to prevent the heaters from turning on at flow rates less than 19.3 SCFM. The heaters use K-Type thermocouples for controller feedback. The maximum allowable pressure for these heaters is 120 psig (Farnam-Tutco).

Though these heaters are rated to higher flow rates and pressures than the SureHeat Jet inline heater from Sylvania used on the old rig, (OSRAM Sylvania) there were some issues with certification that arose during delivery of the test rig. Specifically, the Farnam controllers did not come with full CSA approval, and the heaters do not have CRN numbers. The previously used SureHeat Jet heater had a maximum allowable working pressure of only 60 psi, so the new heaters can withstand much higher pressures (C-T Products Company). The heater controllers were subsequently CSA certified and their installation registered with the ESA (certification stickers are in place on the controller boxes).

The new Farnam heater controllers do have a number of user specified safeguards in place that the old controller did not have. First, there is a high temperature limit shut-off switch that makes use of the

downstream K-type thermocouple, and second there is a flow input switch that shuts off the unit if low flow is detected. This switch will be signaled from the PC, allowing semi-manual switching from the work station.

However, due to complications certifying these heaters, they have not yet been installed. Proof tests performed on the heaters produced a small crack in the casing in the heat affected zone near the thermocouple mounting junctions at 130 psig; however, this is well above the normal operating range of 20 psig at the heater.

2.2.1.3 Valves

There are nine basic types of manual control valves available, and each type of valve lends itself to particular applications. A brief description of each valve is presented below:

- ❖ **Globe Valves.** These are a closing-down valve type that can be used to throttle flow. However, they do cause a large flow resistance due to their shape.
- ❖ **Piston Valves.** These work similarly to globe valves as they are another type of closing-down valve, but use the sides of the piston as the sealing face. They also may be used to throttle flow, and handle solids in suspension well. They are also subject to a large flow resistance.
- ❖ **Parallel Gate Valves.** These valves are a type of slide valve, where a disc slides across the opening area and gets forced back against the seal by the upstream pressure. Typically, these valves are used as shut-off valves, but due to their small size, they have very low flow resistance when fully open. They do not seal well in low pressure applications.
- ❖ **Wedge Gate Valves.** Similar to the parallel gate valve, the only difference is a wedge-shaped plug that allows for low pressure applications, in addition to the high pressure shut-off application that the parallel gate valve excels in.
- ❖ **Plug Valves.** Generic plug valves are a rotary valve with that is ported to allow flow through. These valves work best as shut-off valves or in flow diverting applications. Though plug valves may be used to throttle flow, leaving a plug valve partially opened may deform the seal, which may either lock the valve in place, or cause it to leak.
- ❖ **Ball Valves.** Ball Valves are a widely used subset of plug valves with a spherical plug.

- ❖ **Butterfly Valves.** These valves use a disc that rotates in the flow, and serve very well at throttling flow. Butterfly valves provide sensitive flow control between 15° and 70° opening angles.
- ❖ **Pinch Valves.** These valves use a flexible body to restrict flow. This allows for a restriction without any obstruction to the flow, which makes them ideal for slurries and other solid suspension flows. However, the flexible body does need to be replaced frequently as it ages to avoid rupture due to aging and wear.
- ❖ **Diaphragm Valves.** These are another type of flexible body valve. However, diaphragm valves restrict flow by deforming a diaphragm towards a rigid surface to restrict flow or create a seal. This method does not require as much deformation as a pinch valve, and therefore can last longer.

All of the above valves may be fitted with actuators for automated control, or handles for manual control. However, some types of valves function automatically and require no user input.

- ❖ **Check Valves.** These mechanically prevent flow in the reverse direction by opening in forward flow and closing in reverse flow.
- ❖ **Pressure Relief Valves.** These valves automatically open at a preset pressure to blow off any excess pressure in the system. Alternatively, they may reduce a vacuum by allowing air into the system. Pressure relief valves protect the entire system from damage due to over-pressure or under-pressure conditions.

Based on the above information from Smith (Smith & Zappe, 2004), the valves discussed below were selected. The butterfly valves were specified by Ryerson University, and they are the primary means of flow control in the test rig. The manual ball valves are used both in shut-off and flow diverting applications. Check valves serve to prevent undesired cross-flow between supply tanks, and the pressure relief valves from Kunkle (Lake Villa, Illinois, USA) were selected by Teng and Associates and set to 90 psi to protect downstream components, specifically the heat exchangers from over-pressurization.

2.2.1.3.1 Electrically Actuated Butterfly Valves

Due to familiarity with controlling Bi-Torq (La Fox, Illinois, USA) valves from the past, they were selected as the supplier for the new valves. The same basic actuator was used, but more options were added. The valve body itself was changed from a ¾" ball valve to a 2" butterfly valve. The specifications for the valves are listed below (Bi-Torq, 2008).

- ❖ BY-WE-2-20-200-E-A-4-VP-P1-TX-SPECIAL.
 - 2" Cast Iron Butterfly Valve
 - Wafer Style
 - Stainless Steel Disc and Stem
 - EPDM Seats
 - Bi-Torq BI-200-A-4 115VAC Electric Actuator
 - 200 in-lb Output Torque
 - 5 s Cycle Time
 - 75% Duty Cycle
 - NEMA 4 Large Enclosure
 - Standard Thermal Overload Protection
 - 0.75A Lock Rotor Current
 - Power Break
 - 4-20 mA Electronic Positioner
 - 0-10 Vdc Feedback Potentiometer
- ❖ TEE-BY-LE-2-20-300-A-4-P1-VP-TX-SPECIAL
 - Two 2" Cast Iron Butterfly Valve (MY-LE-2-020)
 - Lug Style
 - Stainless Steel Disc and Stem
 - EPDM Seats
 - Tee
 - Bi-Torq BI-300-A-4-P1-VP-TX 115VAC Electric Actuator
 - 300 in-lb Output Torque
 - NEMA 4 Large Enclosure
 - Standard Thermal Overload Protection
 - 4-20 mA Electronic Positioner
 - 0-10 Vdc Feedback Potentiometer

Five of the single actuated butterfly valves were purchased along with two of the dual actuated tee-mounted butterfly valves that are planned to be used for bypass control as explained in Section 2.2.

Unfortunately, a certification issue arose concerning these valves. The Bi-Torq valves did not have valid CRN numbers. These valves were switched to an equivalent valve from FNW (Portland, Oregon, USA) that had the necessary certifications.

The butterfly valves were used to modulate, or throttle, flow rates throughout the rig. They can also be used as temporary shut-off valves, though ball-valves have been incorporated to serve as the primary means of supply selection and shut-off.

In the event that the butterfly valves require too small an opening area to provide effective control restrictor plates or reducers can be placed at the outlets of the rig to provide back pressure. The downstream restriction is not that much of an issue however, since it was already planned to have elbows in place for directing the outflow in a safe manner. A 2"x1" reducing street elbow was used in conjunction with a reducing bushing to direct flow exhaust and provide the necessary flow restriction.

Figure 15 shows the controller card mounted on each actuator. There are three variable resistors for tuning the on-board valve controller, and they are labeled in the image. The resistor labeled "Span" is used for setting the fully opened position and the "Zero" resistor is used for setting the fully closed position. The "Deadband" resistor determines the smallest increment in control signal for which the actuator will adjust. If the deadband is set too small, it is possible to destroy the actuator gearing, but if it is set too large, fine control of the valve will be lost. The fuse has also been labeled. Figure 16 shows the valves in roughly closed and opened positions.



Figure 15: Photograph of Actuator Controller Card

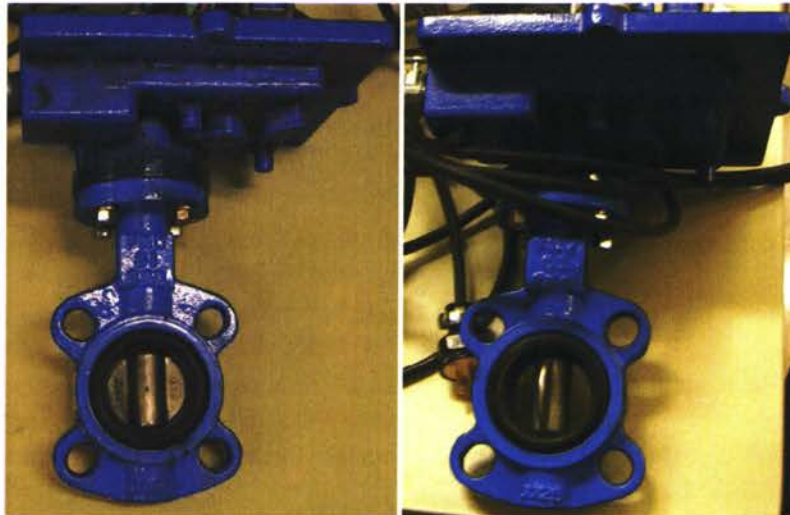


Figure 16: Photograph of Open and Closed Valves

2.2.1.3.2 Manual Ball Valves

These valves were installed to provide a sure means of flow shut-off and air supply selection. Two-port ball valves were used as simple shut-off valves at the inlet and exits of the main supply tanks. This allowed for a clear visual of the present flow arrangement of the rig, and allows any channel to be locked out for maintenance purposes. Tee-type three-port ball valves are used for two purposes: Firstly, the three-port valves serve as a means to select which air supply to use for the ram air channels, and

secondly the valves serve to merge the exhaust flows of the bleed channels before exhausting to the load tank. These valves were not intended to be used to throttle flow, but may be required due to the large butterfly valves being used.

2.2.1.3.3 Check Valves

The check valves were installed just before the inlet of the supply tanks as shown in Figure 5. Check valves allow the tanks to exhaust at different flow rates while being simultaneously filled by the compressor and preventing any cross flow between the tanks. However, for the most extreme case of source decoupling, complete isolation of the tanks via shut-off valves would be the best method.

2.2.1.3.4 Pressure Relief Valves

The pressure relief valves were selected by Teng and Associates, and set for a maximum of 90 psig. It was found that a normal operating pressure of 60 psig with the load tank maintained at 20 psig provided a maintainable flow rate greater than 1000 standard feet per minute (SFPM) for single channel operation.

2.2.1.4 Heat Exchangers

The heat exchangers were designed in cooperation by Ryerson Technical staff and Teng and Associates. They are similar to the heat exchanger used on the previous temperature control rig, but were certified by TSSA. The heat exchangers were found to be limited to 93.3 psig, thereby determining the pressure relief valve setting of 90 psig.

2.2.2 Sensors

A wide variety of sensors were incorporated into the test rig, and the general theory of their operation was explained in Section 1.2.3. The specifications and part numbers of the sensors used on the test rig are shown in the following sections.

2.2.2.1 Thermocouples

The Omega T-Type thermocouples, with part number TC-T-NPT-E-72, were used on the rig along with Omega thermocouple signal conditioners, with part number DRF-TCT-24VDC-0/200C-0/10. The thermocouples are mounted in a ¼" NPT fitting with an exposed junction which allows for faster response. The signal produced by the sensor is very weak and nonlinear, but the conditioner used with the sensor converts the signal to a linear 0-10 Vdc signal that can be easily acquired by the computer. The 0-10V range of the conditioners correspond to a temperature range of 0°C to 200°C, and the conditioners have a response time of 250ms. Additionally, the heater has two K-Type thermocouples that are connected to the heater controller. These K-Type thermocouples are used for temperature feedback by the heater controller as well as the high temperature shut-off sensor. The T-Type thermocouples may be used for measuring temperature throughout the rig as experiments require.

2.2.2.2 Resistance Temperature Detectors

Proprietary suppliers donated aircraft resistance temperature detectors (RTDs) for experimentation at Ryerson University. However, no documentation was given with these sensors so analysis was performed to determine the type of RTD and what wiring method would allow for the best performance. A resistance check was performed across pairs of pins using an Omega CA150 Handheld Calibrator in an ice water bath maintained at 0°C. The readings shown in Table 1 were for the RTDs with serial numbers 113C-0203 and 100C-123. Both sensors performed similarly so only one table is shown.

Table 1: Measured Resistance between Pins for RTDs and Pin Information

	1	2	3	4	5	6
1	-	500Ω	NC	NC	NC	NC
2	-	-	NC	NC	NC	NC
3	-	-	-	500Ω	NC	NC
4	-	-	-	-	NC	NC
5	-	-	-	-	-	NC
6	-	-	-	-	-	-
	+ Excitation 1	- Excitation 1	+ Excitation 2	- Excitation 2	No Connection	No Connection

Therefore, it was concluded that the RTDs each contained two 500 Ω sensing elements, and that each sensing element could be wired as a 4-wire constant current RTD. Another concern was that the excitation current may vary as the resistance of the RTD changes. Therefore, the excitation current from the NI PCI6704 output card was checked and confirmed to remain constant using a 1k Ω precision rheostat. The pin information of the sensor itself is shown at the bottom of Table 1. A custom plastic adapter was made to protect the top of the RTD and provide a Preh connector for easier lead wire connection.

2.2.2.3 Pressure Transducers

All pressure sensors available to be used on the rig are tabulated below.

Table 2: Pressure Sensor Information

Quantity	Part Number	Output Signal (V)	Range
4	PX303-100G10V	1-11V	0-100 psig
2	PX209-100G10V	0-10V	0-100 psig
1	PX303-300G10V	1-11V	0-300 psig
1	PX219-030A10V	0-10V	0-30 psia
4	PX-219-200G10V	0-10V	0-200 psig

The five PX219 Sensors were purchased specifically for this rig. The PX219 series differ from the PX209 and PX303 by the inclusion of a four-pin DIN Connector rather than a lead wire. This allows for easier rewiring of the sensor. The 200 psig range was selected due to the design maximum operating pressure of 120 psig. This was purchased before the maximum operating pressure was found to be 90 psig.

2.2.2.4 Flow Sensors

Two different flow sensor models are used on the rig, though they operate on the same principals. No documentation existed for one of the flow sensor models. However, information on the Omega flow sensors is provided here. Two flow speed sensors from the previous test rig were Omega FMA905 series flow sensors, with an operating range of 0-5000 SFPM (standard feet per minute). Standardized flow

rate may be calculated if the cross sectional area of the pipe is known and it would be given in SCFM (standard cubic feet per minute). Standard denotes that the value corresponds to flow at standard temperature and pressure conditions. The actual mass flow in pounds per second or kilograms per second may then be calculated by dividing by standard atmospheric density, and considering the pipe diameter in which the sensor is mounted.

A new flow sensor with NIST traceability will be purchased and used on the rig to calibrate the other four flow sensors. All sensors will be calibrated to output measurements in SFPM. This allows for the sensors to make accurate readings regardless of the pipe diameter in which the sensor is located. Calibration information is located in Section 2.4.

Once all flow sensors were hooked up and operational, it was found that the actual signal range of the proprietary thermal flow sensors was 0-5 Vdc.

2.2.2.5 Potentiometers

These 10 k Ω potentiometers are found on the controllers and provide 0-10 Vdc output based on the valve angular position. Since they only rotate 90°, readings typically have an approximate range between 3 V and 6 V. They are to be used to provide the actual position of the valve for calculations requiring the valve opening area, rather than assuming the valve opening is equal to the commanded value. The potentiometers may also allow for further valve hysteresis study in the future. (Chan, Actuator Hysteresis Modelling and Compensation with an Adaptive Search Space Based Genetic Algorithm, 2003)

2.2.2.6 Control Computer

The control computer used for the test rig had the following components.

- ❖ Asus P5Q Premium Motherboard
- ❖ Intel Core2Quad Q9300 Processor
- ❖ WesternDigital Velociraptor 150GB Hard Drive
- ❖ Generic IDE Hard Drive
- ❖ 4GB DDR2 Ram
- ❖ Sapphire Radeon HD3850 Video Card
- ❖ LG DVD-RW Drive
- ❖ Multi-Card Reader
- ❖ Windows Vista Business 64bit
- ❖ Rack Mount Rails
- ❖ Two 19" Samsung Flat Panel Displays
- ❖ National Instruments PCI-6224 M-Series Analog-to-Digital Card
- ❖ National Instruments PCI-6704 Analog Digital-to-Analog Card
- ❖ National Instruments PCI-6034 E-Series Analog-to-Digital Card

Conflicts between 64bit Vista and SIMULINK Real-time Windows Target required 32bit Windows XP to be installed on the system. The hard drive has been split into two partitions. One partition is for the operating system and programs, and the other is for data and program files.

2.3 Instrumentation

To connect the sensors to the computer required a large amount of wiring and connections. The connections were sorted between two terminal boxes which have been mounted in the rack. One box handled the pressure sensors, thermocouples, and actuator potentiometers, and the other box handled flow sensors, RTDs, actuator excitation, and the heater controller flow switch.

Both instrumentation boxes and the control computer are mounted in a movable rack, which is shown in Figure 17. The rack is shown with the door both opened and closed.



Figure 17: Rack Mounted Data Acquisition System and Workstation

2.3.1 Wiring Diagrams

The wiring diagrams are attached in Appendix B. Most connections inside of the boxes are simply routing the signal wires to the terminal boards, power sources, or shielding ground. However, fuses, switches, terminal blocks, and pin connections for the Preh connectors are also shown in the diagrams.

2.3.2 Construction

Construction of the boxes spanned from December 2008 to April 2009. Originally the boxes were intended to only be used for shielded connections. However, additional components such as switches and fuses were added to increase protection of the components inside of the boxes, specifically the flow sensor boards and thermocouple conditioners. Short circuit protection was also provided for all power circuits.

The boxes were purchased without any cutouts. The cutouts were machined using drills and hand tools such as a nibbler and files. Large components were then mounted in the boxes, specifically the terminal boards, thermocouple conditioners, screw terminals, and flow sensor boards. Once fit was checked, all connectors and switches were installed, and wiring began.

Some changes in the original wiring were performed, specifically on the RTDs as additional information about their operation was found as shown in Section 2.2.2.2.

Overall, wire color consistency was attempted to be achieved for all connections of a given type. This can be seen from the wiring diagrams of Appendix B and the pictures shown below. Custom connectors were made by Ryerson Technical Staff for the RTDs and Flow Sensors. The pin-outs are also shown in Appendix B.

Access to the box can be achieved via the front panel while the box is mounted in the rack. However, this is limited to observation only. To service the box, it should be fully removed from the rack, and the internal components may be easily accessed from the top panel. No provision has been made for the sides, bottom, or back panel to be removed.

2.3.2.1 Terminal Box #1

The first box is the main data acquisition terminal box. It contains all of the terminal connections for pressure transducers, thermocouples, and potentiometers. Terminal Box #1 (TB1) uses 27 channels of a total capacity of 32 single ended analog data acquisition channels available on the National Instruments PCI-6224 M-Series Board mounted on the computer. Figure 18 shows the front panel of TB1 with main the components labeled. The thermocouple conditioner fuses are rated to 250 mA, and there is one fuse for each conditioner. The two short circuit fuses, TMAIN and PMAIN, require 3 A and 375 mA fuses respectively. The switches allow power to the specified sensors, and the indicator light is lit when the circuit is powered.

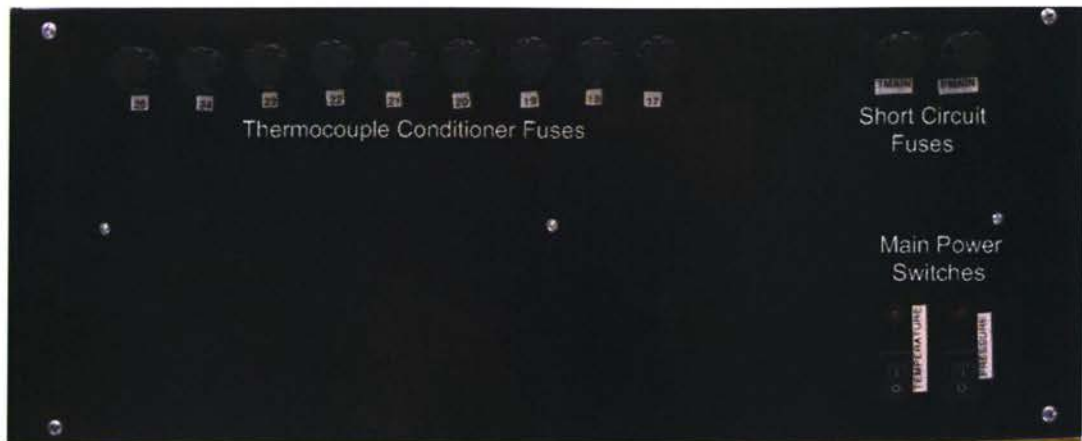


Figure 18: Front Panel Photograph of Terminal Box #1

Figure 19 is a picture of the inside of the box, as it would appear when the top is removed for servicing. At the bottom of the picture is the front panel, with the fuse connections and switches. The large Anderson connector bundle is used to disconnect the front panel when the box is rack mounted. Thermocouple conditioners are DIN rail mounted along the sides of the box. The green boards are both National Instruments CB-68LPR terminal boards used to route signal wires into the 68-pin cable that connects to the computer. Each board can handle 16 channels, with the left board being filled to capacity with nine channels used by thermocouples and seven channels used by potentiometers. The right board has 5 spare channels with 11 used by the pressure transducers.

Internal wiring of the box was kept as consistently as possible. The blue sheathed wire with blue and red conductors is T-Type thermocouple extension wire, used to patch between the connectors and conditioners. Red and black wires are typically used for power or excitation of the pressure transducers and conditioners. Green and black are pressure transducer signal wires, with white and black for thermocouple signals, and blue and black for potentiometer signals. Ground wire colours vary from connector to connector, but are typically brown for pressure transducer connectors, green for potentiometer connectors, and black for thermocouple connectors.

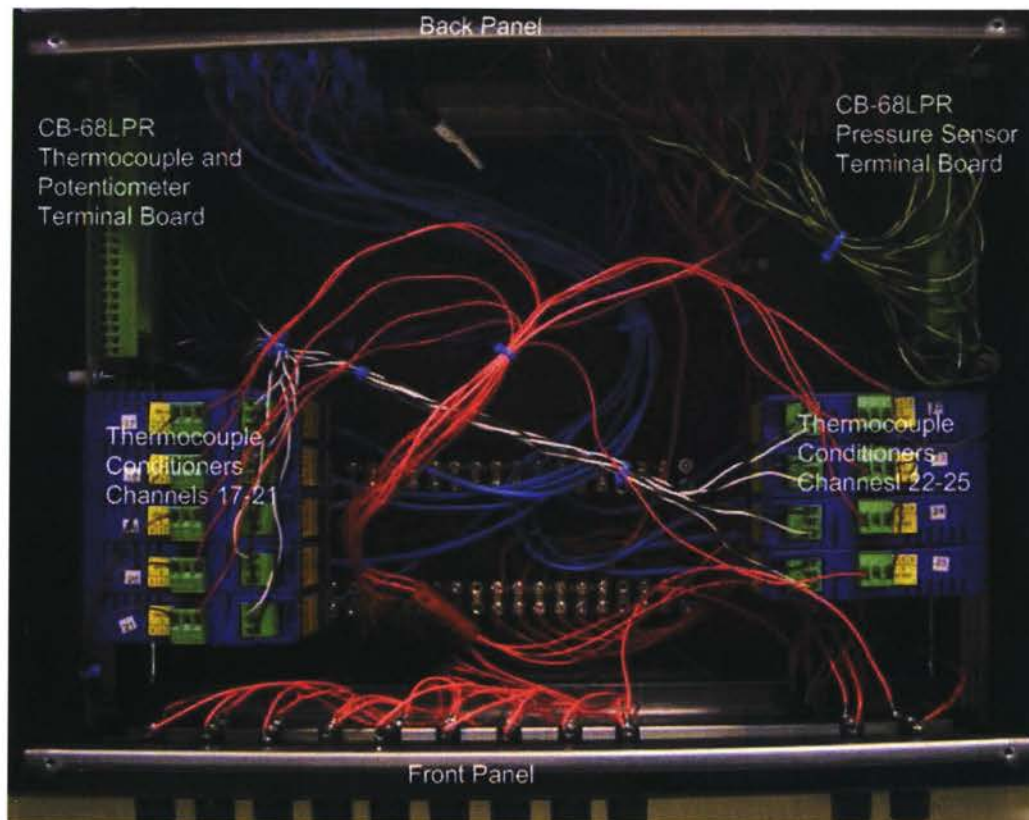


Figure 19: Top Internal Photograph of Terminal Box #1

Figure 20 is a rear view of TB1. It shows three power connections on the bottom left, a 5 Vdc, 24 Vdc, and a spare. The 5 Vdc provides power to the indicator lights on the front panel, as well as a grounding route for all shielding. The 24 Vdc connection provides power for the thermocouple conditioners and pressure transducers. 7-pin Preh connectors numbered 1-11 are the pressure transducer connectors. The blue connectors numbered 17-15 are used for the thermocouples, and the 4-pin Preh connectors numbered 25-32 are used for the potentiometers. There are two spare Preh connectors in this box for future expansion. Thermocouple wire shielding will be connected to ground via the screw terminals labeled with TSHIELD.

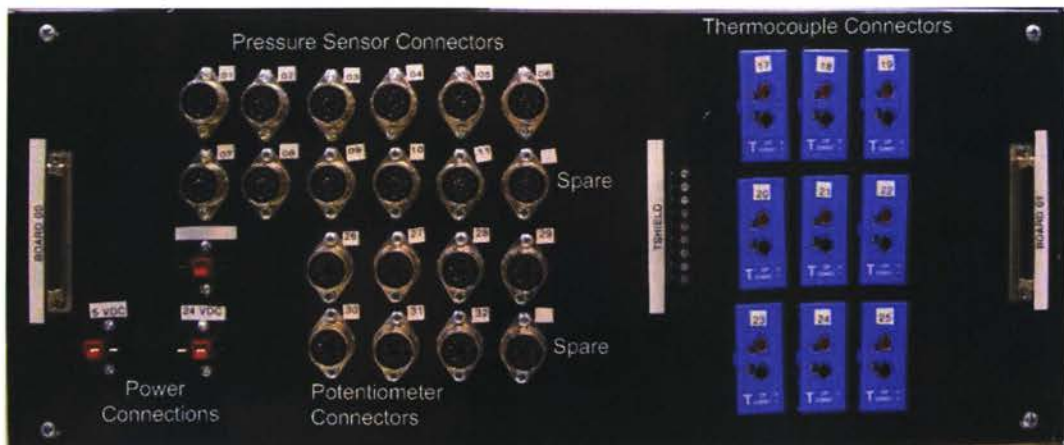


Figure 20: Back Panel Photograph of Terminal Box #1

2.3.2.2 Terminal Box #2

Terminal Box #2 (TB2) is used for actuator excitation and sensors that may require computer controlled excitation, such as the RTDs. Additionally, it also provides data acquisition for all of the flow sensors. It has a capacity of 32 analog outputs split between 16 voltage and 16 current output channels, and eight digital input/output channels. Furthermore, it also has 16 single ended analog data acquisition channels. Eleven of the current output channels are being used, split between seven actuators and four RTD elements. Two digital channels are being used for the heater controller flow switches. Eleven of the data acquisition channels are being used, two for flow sensors, four for RTDs and five for Omega flow sensors.

Figure 21 shows the front panel of TB2. It has a similar arrangement to TB1, but has switches for each flow sensor. The RTDs do not require switches since they are excited by the computer. Provision was made for five Omega flow sensors, though only three are planned to be used currently. The Omega flow sensors are protected by 375 mA fuses, and the other flow sensors are protected by 500 mA fuses. The spare switches and fuses are not currently hooked up.

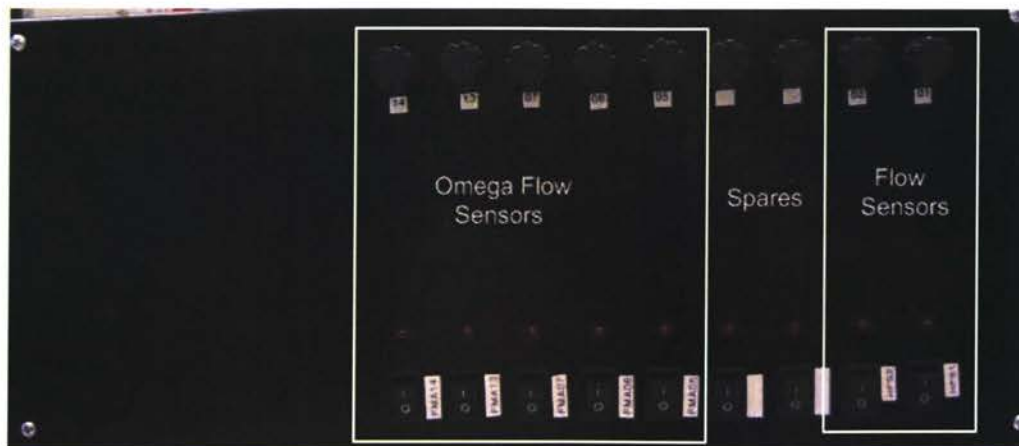


Figure 21: Front Panel Photograph of Terminal Box #2

Similar to TB1, Figure 22 shows the inside of TB2 as viewed when the top access panel is removed. The bottom left is where the flow sensor conditioner cards are located for the proprietary flow sensors. Four cards are mounted though only two are being used. They are numbered one through four, with cards two and four being used. No wiring diagrams are available for these cards. The left green board is the SCB-68 used for signal excitation. Analog excitation wires are blue and white pairs, with digital excitation as black and white. Red and black wires are used for power, while green and black are used for acquired signals.

The back panel of TB2, shown in Figure 23, has been labeled to show the current usage of connectors. The Anderson connectors along the bottom are used for power, with 5 Vdc again being used to power the indicator lights and provide shielding ground, 28 Vdc are used for flow sensor excitation, and five 15 Vdc connectors for each of the Omega flow sensor channels. There are three spare Preh connectors for future expansion. Flow sensor connectors are numbered 1 and 2, with RTDs labeled 3 and 4. Omega flow sensors are numbered 5 through 7, 13, and 14. Actuator Excitation connectors are labeled I17 through I23, with the heater controller flow switch labeled D02/D03. The flow switch connector carries signals for both boxes, so it is required to be split near the controller boxes.

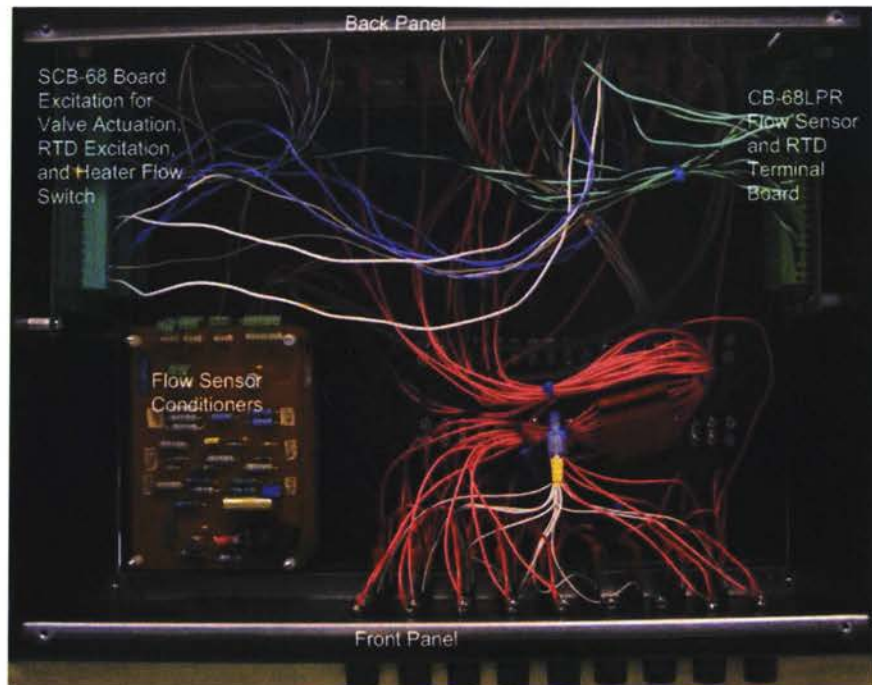


Figure 22: Top Internal View of Terminal Box #2

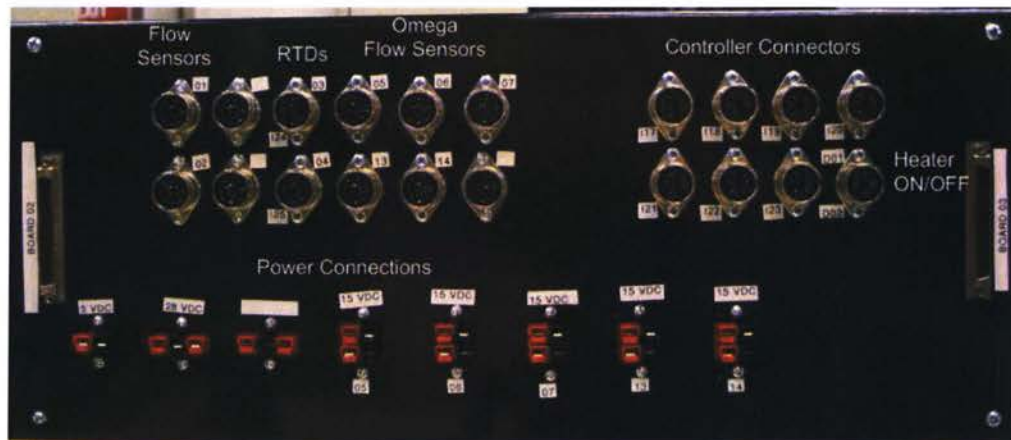


Figure 23: Back Panel Photograph of Terminal Box #2

2.3.2.3 Extension Wires

Potentiometer and control signal connectors are sent to their respective control actuator via a two wire patch cable between the two boxes and a four wire cable to the actuator. Two 4-pin male connectors are used to interface with the box connectors, and are joined in a single 8-pin female connector. An 8-pin male connector connects to the patch cable female 8-pin connector. The six wire lead extension

terminates in an 8-pin female connector near the actuator, which then plugs into the actuator signal lead wire.

The pressure sensor 7-pin female connector on the box is connected to the 7-pin male connector on the six wire lead extension cable. The lead extension terminates in an 8-pin connector which then plugs into the sensor lead wire.

The RTD lead extension is reversible with two 8-pin male connectors and a six wire cable. The connectors plug into the sensor and the box directly. The thermocouple lead wires plug into the lead extensions, all of which are T-Type wire for those that are used in rig control. K-Type sensors are used for the heater controllers, and these are yellow.

The flow sensor wires are composed similarly to the RTD wires, but have an eight wire lead extension cable. However, the Omega flow sensors are connected to the box with an 8-pin connector, but connect directly to the sensor by a 7-pin DIN connector via a six wire lead extension.

All sensors are to be calibrated in the final mounting configuration. For example, the final configuration would be routed from the box via lead extension, to lead wires and finally the sensor. Once calibrated, the final configuration will be labeled so that the wires can be easily reconnected in the same format when necessary. Whenever a sensor is to be used with a lead wire other than what it was originally calibrated with, the new configuration should be recalibrated. Most of the sensors require the lead extensions to be in place to be operational and efforts were made to ensure that if any connector is plugged into the wrong position, no harm would come to the sensor or data acquisition system.

A breakout box was also made for use with the rig to aid in connection, and pin identification. It was comprised of two 9-pin terminal blocks at the top, labeled with shield and pins 1 through 8. Two male and two female 8-pin Preh connectors are used to interface with any of the sensors utilizing an 8-pin

connection. This allows for easy pin identification and voltage measuring for the pressure sensors, flow sensors, and RTDs.

2.4 Calibration

Each sensor was calibrated to a standard as explained in each sensor subsection. When available, a calibrating unit was used, otherwise the sensors were calibrated to a common sensor. All sensors are calibrated with any lead or extension wires in place that will be used when installed in the rig. Once the sensor and its surroundings have reached a given set-point, data is recorded in the form of a running mean and standard deviation. The signal to noise ratio was found by dividing the running mean by the running standard deviation.

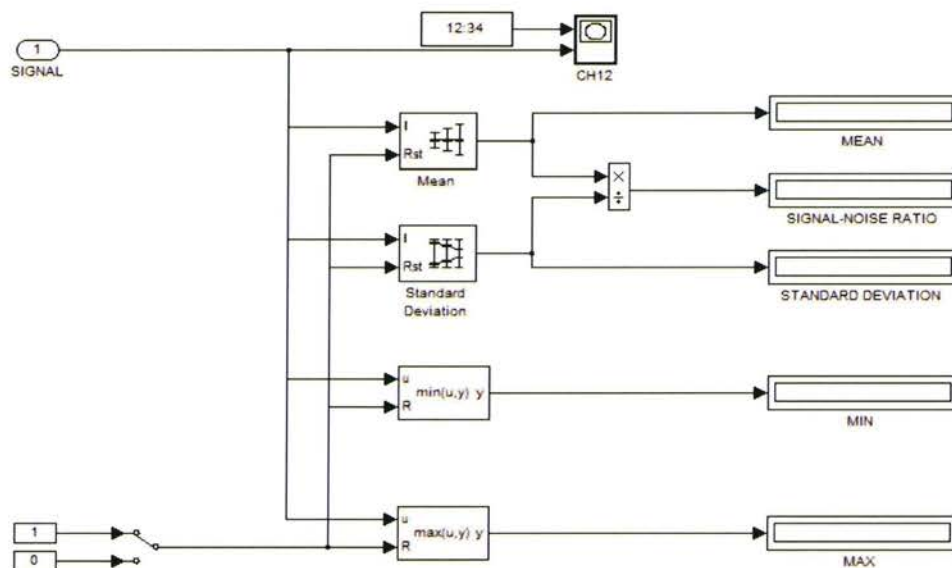


Figure 24: Sample SIMULINK Signal Analysis Subsystem Block

An XY-Graph block, in this case denoted by CH12, is used to show the current sensor reading as a voltage versus time. The sample rate was typically 1 kHz.

2.4.1 Resistance Temperature Detectors

The two resistance temperature detectors (RTDs) were calibrated on May 26, 2009. Each RTD has two sensing elements in the tip, so in effect four sensors were calibrated. The RTDs were calibrated on a Fluke Hart Scientific 9120S Drywell, Serial Number A74084, in the EPH343A Laboratory. Basic steps in obtaining the calibration data involved the following.

- 1) Set temperature of drywell and wait for steady state, approximately 7 min.
- 2) Run SIMULINK with data acquisition signals routed through the signal analysis block for approximately 2 min.
- 3) Stop SIMULINK and take readings.

The RTDs were excited by 1 mA constant current as recommended previously (Keithley Instruments, Inc., 2007). The following data was recorded in Table 3 and Table 4 from the tests.

Table 3: RTD 100C-123 Calibration Data: 1 mA Excitation

Constant 1 mA Excitation	100C-123					
	Channel 4			Channel 12		
Temperature (°F)	Mean (V)	SD (V)	SNR	Mean (V)	SD (V)	SNR
212.0	0.7568	0.0005336	1418	0.7562	0.0005433	1392
211.0	NA	NA	NA	NA	NA	NA
176.0	0.7210	0.0005281	1365	0.7206	0.0005232	1377
140.0	0.6850	0.0005169	1325	0.6849	0.0004999	1370
104.0	0.6491	0.0004994	1300	0.6492	0.0004949	1312
68.0	0.6131	0.0004656	1317	0.6135	0.0004613	1330
32.0	0.5774	0.0004478	1290	0.5780	0.0004446	1300
31.0	NA	NA	NA	NA	NA	NA

Table 4: RTD 113C-0203 Calibration Data: 1 mA Excitation

Constant 1 mA Excitation	113C-0203					
	Channel 3			Channel 11		
Temperature (°F)	Mean (V)	SD (V)	SNR	Mean (V)	SD (V)	SNR
212.0	0.7597	0.0005338	1423	0.7599	0.0005231	1453
211.0	0.7587	0.0005416	1401	0.7589	0.0005470	1387
176.0	0.7232	0.0005136	1408	0.7234	0.0005263	1375
140.0	0.6865	0.0005006	1371	0.6867	0.0005061	1357
104.0	0.6497	0.0004937	1316	0.6499	0.0004564	1424
68.0	0.6129	0.0004869	1259	0.6131	0.0004485	1367
32.0	0.5759	0.0004414	1304	0.5763	0.0004425	1302
31.0	0.5748	0.0004545	1265	0.5751	0.0004283	1343

The data points 211.0°F and 31.0°F were collected to observe the signal difference between 1°F at the low and high end of the calibration range. These readings were not used in the following curve fits shown in Figure 25 through to Figure 28. The polynomial was used for increased accuracy even though there is a very linear response from the sensors.

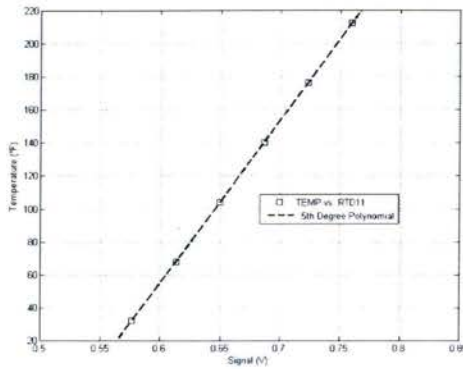


Figure 25: RTD Channel 11 Curve Fit: 1 mA Excitation

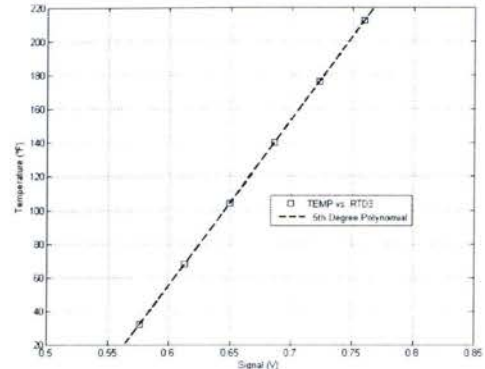


Figure 27: RTD Channel 3 Curve Fit: 1 mA Excitation

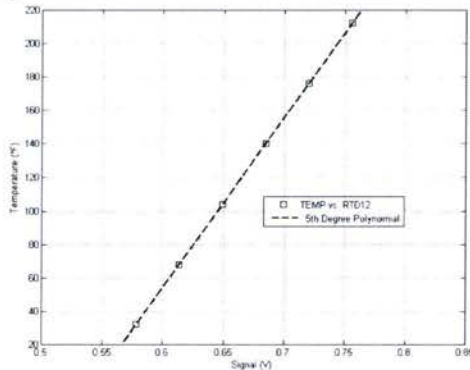


Figure 26: RTD Channel 12 Curve Fit: 1 mA Excitation

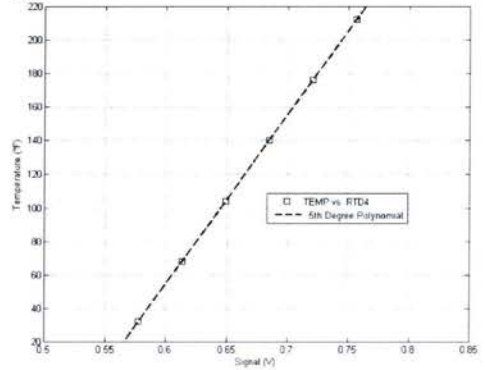


Figure 28: RTD Channel 4 Curve Fit: 1 mA Excitation

A fifth degree polynomial was used for each of the data sets. The polynomial and coefficient values for the relevant channel are given below. The polynomial was found using the MATLAB Curve Fitting Toolset, **cftool**, and the results for each resistor are given in Table 5.

$$T(v) = p_1v^5 + p_2v^4 + p_3v^3 + p_4v^2 + p_5v + p_6 \quad (2.1)$$

- ❖ T Temperature Reading ($^{\circ}\text{F}$)
- ❖ v Signal Reading (V)
- ❖ p Polynomial Coefficient

Table 5: RTD Polynomial Calibration Values: 1 mA Excitation

Coefficient	RTD3	RTD4	RTD11	RTD12
p_1	-37890	72050	42990	100100
p_2	129400	-243600	-141400	-339500
p_3	-176100	328900	185700	459800
p_4	119500	-221800	-121700	-310800
p_5	-39440	75680	40750	105900
p_6	4923	-10590	-5720	-14670

The largest standard deviation from Table 3 and Table 4 is 0.0005470 V \approx 0.00055 V for 211.0 $^{\circ}\text{F}$ measured on Channel 11. For a normal distribution, 99.7% of data lies within three standard deviations to either side of the mean (Rees, 1989). The mean measured was 0.7589 V, and three standard deviations are equal to 0.00165 V. Therefore, 99.7% of the data sampled was between 0.75732 V and 0.7606V. Using the RTD11 polynomial, the mean value was found to be 211.1 $^{\circ}\text{F}$ with a lower value of 209.4 $^{\circ}\text{F}$ and an upper value of 212.7 $^{\circ}\text{F}$. The difference between these values and the mean is -1.6 $^{\circ}\text{F}$ and 1.6 $^{\circ}\text{F}$. Given that the drywell was only accurate to the nearest tenth of a degree Fahrenheit, the uncertainty of a given reading is approximately $\pm 1.6^{\circ}\text{F}$.

After discussion of the results, it was decided to calibrate the sensor with 3 mA and 5 mA excitation to determine if self-heating becomes a factor. The increase of excitation current increases the voltage output of the sensor as well, but it was feared that self-heating would become a problem. On May 28, 2009, the calibration was performed again using the same Fluke Hart Scientific 9120S Drywell, Serial Number A74084, in the EPH343A Laboratory. The following tables, which are numbered Table 6 through Table 9, show the results for the different sensors at different excitations.

Table 6: RTD 113C-0203 Calibration Data: 3 mA Excitation

Constant 3 mA Excitation	113C-0203					
	Channel 3			Channel 11		
Temperature (°F)	Mean (V)	SD (V)	SNR	Mean (V)	SD (V)	SNR
212.0	2.131	0.0005495	3878	2.130	0.0005327	4000
176.0	2.020	0.0005229	3864	2.020	0.0005122	3944
140.0	1.909	0.0005340	3575	1.909	0.0005026	3797
104.0	1.798	0.0004858	3701	1.798	0.0004673	3847
68.0	1.686	0.0004669	3610	1.686	0.0004552	3703
32.0	1.575	0.0004522	3482	1.575	0.0004492	3506

Table 7: RTD 113C-0203 Calibration Data: 5 mA Excitation

Constant 5 mA Excitation	113C-0203					
	Channel 3			Channel 11		
Temperature (°F)	Mean (V)	SD (V)	SNR	Mean (V)	SD (V)	SNR
212.0	3.513	0.0005448	6448	3.512	0.0005545	6333
176.0	3.328	0.0005316	6260	3.327	0.0005332	6240
140.0	3.142	0.0005191	6054	3.142	0.0005155	6095
104.0	2.955	0.0004732	6245	2.955	0.0004836	6109
68.0	2.768	0.0004773	5799	2.768	0.0004667	5932
32.0	2.580	0.0004453	5793	2.580	0.0004491	5745

Table 8: RTD 100C-123 Calibration Data: 3 mA Excitation

Constant 3 mA Excitation	100C-123					
	Channel 4			Channel 12		
Temperature (°F)	Mean (V)	SD (V)	SNR	Mean (V)	SD (V)	SNR
212.0	2.12174	0.000526082	4033.10	2.11904	0.000530564	3993.93
176.0	2.01332	0.000518575	3882.41	2.01133	0.000534421	3763.57
140.0	1.90415	0.000527419	3610.31	1.90280	0.000528689	3599.10
104.0	1.79627	0.000486590	3691.54	1.79567	0.000490508	3660.83
68.0	1.68835	0.000466538	3618.89	1.68859	0.000483805	3490.23
32.0	1.58342	0.000444688	3560.74	1.58465	0.000457959	3460.24

Table 9: RTD 100C-123 Calibration Data: 5mA Excitation

Constant 5 mA Excitation	100C-123					
	Channel 4			Channel 12		
Temperature (°F)	Mean (V)	SD (V)	SNR	Mean (V)	SD (V)	SNR
212.0	3.502	0.0005453	6423	3.497	0.0005475	6387
176.0	3.320	0.0005276	6293	3.316	0.0005436	6100
140.0	3.139	0.0005486	5722	3.136	0.0005489	5713
104.0	2.957	0.0004869	6072	2.955	0.0004941	5981
68.0	2.778	0.0004893	5676	2.777	0.0004986	5570
32.0	2.601	0.0004479	5807	2.602	0.0004412	5899

The signal to noise ratio (SNR) is the clearest indicator of how the increase in excitation current improves the measurements. Additionally, the 5mA excitation gives the lowest line losses when the total resistance is calculated using $R = V/I$, and this is shown below in Table 10 for the Channel 4 Sensor.

Table 10: Total Resistances for Given Temperature and Excitation

Temperature (°F)	Resistance for Given Excitation (Ω)		
	5mA	3mA	1mA
212.0	700	707	757
176.0	664	671	721
140.0	628	635	685
104.0	591	599	649
68.0	556	563	613
32.0	520	528	577

The actual resistance at 32°F is 500 Ω, so the line resistance at 5mA is only 20 Ω, which is much less than the 77 Ω cause by the 1mA excitation current. The fifth degree polynomial coefficients are given in the table below for each sensor at 5 mA excitation in Table 11.

Table 11: RTD Polynomial Calibration Values: 5 mA Excitation

Coefficient	RTD3	RTD4	RTD11	RTD12
p_1	-61.75	-108.6	-64.40	-132.1
p_2	945.0	1647	984.3	2003
p_3	-5767	-9957	-6000	-12110
p_4	17550	29990	18240	36480
p_5	-26430	-44780	-27450	-54540
p_6	15650	26390	16240	32240

The maximum standard deviation for the 5 mA excitation is $0.0005545 \approx 0.00055$, which is similar to the standard deviation using 1 mA excitation. However, the signal is much stronger and the mean value is equal to 212.0°F with the limits given by three standard deviations of 212.3°F and 211.7°F or the overall uncertainty is $\pm 0.3^\circ\text{F}$. With the much smaller uncertainty, the 5 mA excitation will be used for data acquisition on the test rig.

2.4.2 Thermocouples

Calibrating the thermocouples was slightly more complicated than the RTDs. A water bath was used to calibrate the thermocouples, using a calibrated RTD as the reference temperature. The calibration took place from June 25-26, 2009 using a Fisher Hotplate, Model 80 with Serial Number 102. First, an ice bath was made for the low temperature point. Next, the hotplate was used to heat the water to several temperatures, up to the boiling point. Finally, the bath was left to cool overnight so that the entire assembly would be at room temperature in the morning for the final reading. After the calibration was completed, all lead extensions and thermocouples were labeled with the corresponding channel. Serial numbers would have been used, but they are slightly obscured on the sensor.

The data collected is shown below from Table 12 through to Table 16 with the sensors labeled by channel number.

Table 12: Thermocouple Calibration Measurements, Channels 17-18

RTD (°F)	Channel 17 (V)			Channel 18 (V)		
AVERAGE	MEAN	SD	SNR	MEAN	SD	SNR
31	0.0583	0.000627	93	0.1298	0.001051	123
68	1.0476	0.000960	1091	1.0646	0.001592	668
141	3.0334	0.002132	1423	3.1008	0.002864	1082
178	4.0065	0.004112	974	4.0783	0.003237	1259
212	4.9380	0.001035	4769	4.9910	0.002590	1926

Table 13: Thermocouple Calibration Measurements, Channels 19-20

RTD (°F)	Channel 19 (V)			Channel 20 (V)		
AVERAGE	MEAN	SD	SNR	MEAN	SD	SNR
31	0.1363	0.000476	287	0.1140	0.001032	110
68	1.0567	0.001906	554	1.0272	0.001326	774
141	3.1225	0.00227	1376	3.0724	0.002631	1168
178	4.0914	0.003869	1058	4.0365	0.00417	968
212	5.0151	0.000962	5215	4.9413	0.004249	1163

Table 14: Thermocouple Calibration Measurements, Channels 21-22

RTD (°F)	Channel 21 (V)			Channel 22 (V)		
AVERAGE	MEAN	SD	SNR	MEAN	SD	SNR
31	0.1113	0.000787	141	0.1228	0.000679	181
68	1.0276	0.001993	515	1.0643	0.001562	681
141	3.1124	0.002741	1135	3.1224	0.001783	1751
178	4.0882	0.004072	1003	4.0809	0.005336	764
212	5.0090	0.002065	2426	5.0149	0.001141	4370

Table 15: Thermocouple Calibration Measurements, Channels 23-24

RTD (°F)	Channel 23 (V)			Channel 24 (V)		
AVERAGE	MEAN	SD	SNR	MEAN	SD	SNR
31	0.1206	0.000424	284	0.1560	0.001182	132
68	1.0639	0.00147	724	1.0848	0.001598	679
141	3.0977	0.001999	1549	3.1348	0.001215	2579
178	4.0644	0.004184	971	4.0986	0.004326	947
212	4.9865	0.001616	3086	5.0210	0.001251	4013

Table 16: Thermocouple Calibration Measurements, RTD Readings and Channel 25

RTD (°F)			Channel 25 (V)		
3	11	AVERAGE	MEAN	SD	SNR
30.57	30.61	31	0.0936	0.000484	193
68.15	68.16	68	1.0710	0.001156	927
141.2	141.3	141	3.0611	0.002482	1233
177.8	177.9	178	4.0358	0.003528	1144
212.1	212.3	212	4.9633	0.001129	4398

All of the RTD temperature measurements were rounded to the nearest full degree and then each thermocouple channel was calibrated in a similar manner to the RTDs but used a fourth degree polynomial. The irregular standard deviations and signal to noise ratios were due to the inconsistencies of the water bath as well as actual signal noise. The drywell used for calibrating the RTDs would have been used, but the thermocouple probes would not fit in the calibration ports. The polynomial coefficients for all nine thermocouples are shown in the tables below from Table 17 through Table 19.

Table 17: Thermocouple Coefficients: Channels 17-19

Coefficient	17	18	19
p_1	-0.0979	-0.1514	-0.2194
p_2	0.9602	1.7533	2.4931
p_3	-2.8464	-6.5739	-9.1491
p_4	39.5523	45.3785	48.2195
p_5	28.7039	25.2181	24.5935

Table 18: Thermocouple Coefficients: Channels 20-22

Coefficient	20	21	22
p_1	-0.2030	-0.2157	-0.2331
p_2	2.3173	2.4865	2.5405
p_3	-8.5258	-9.2485	-8.7884
p_4	47.7463	48.2337	46.7996
p_5	25.6641	25.7440	25.3814

Table 19: Thermocouple Coefficients: Channels 23-25

Coefficient	23	24	25
p_1	-0.1801	-0.2126	-0.1022
p_2	1.9880	2.3955	1.0538
p_3	-7.0142	-8.6918	-3.3984
p_4	45.2449	47.6539	40.6253
p_5	25.6416	23.7684	27.2268

To determine the actual uncertainty of the thermocouple measurements is slightly more difficult since most of the measurements were not entirely at steady state. The exception to this was at 212°F where the reading was within the uncertainty for the RTD, and clearly had the greatest signal to noise ratio for any thermocouple calibration point. The highest standard deviation at 212°F may be found on channel 20 at approximately 0.0042V. For three standard deviations, the mean value is 212.0°F with an interval between 211.5V and 212.4V, or an uncertainty of approximately $\pm 0.5^\circ\text{F}$. However, considering the additional uncertainty of the RTDs, which is $\pm 0.3^\circ\text{F}$, used to calibrate the thermocouples, a total uncertainty of at least $\pm 1^\circ\text{F}$ would not be unexpected.

The zero and span adjustments available on the conditioners were not used during this calibration. However, in the future, it may be desirable to thoroughly calibrate the conditioners, and use a drywell, if possible, for more accurate calibration points. Thermocouple calibrations are also heavily influenced by lead length, and therefore whenever a sensor is switched from one lead to another a new calibration should be performed.

2.4.3 Pressure Sensors

The pressure sensor calibration was performed on July 23, 2009. Essentially, all of the sensors were mounted on the same channel, and that channel was pressurized to a specified value, in general multiples of 20 psi. One sensor was used as exact and the Omega CA150 handheld calibrator was used to get as near to a multiple of 20 psi as possible. The basic procedure used is shown below:

- 1) Mount and wire all pressure sensors in a single channel.
- 2) Disconnect one sensor, and hook up to the CA150 Calibration Unit.
- 3) Charge channel to 20 psig.
 - a. Slightly Over-Pressurize.
 - b. Reduce Pressure to as close to 20 psig as the Calibration Unit can measure.
 - i. For PX219 Sensors, 1 Vdc = 20 psig
 - ii. For PX303 Sensors, 3 Vdc = 20 psig
 - iii. For PX209 Sensors, 2 Vdc = 20 psig
- 4) Reconnect sensor, and run acquisition system for one minute.
- 5) Disconnect the same sensor as before, and get final reading from the Calibration Unit
- 6) Repeat steps (2) to (5) up to 80 psig at 20 psi increments.

The readings were averaged over a minute, and the PX303 data is given in Table 20 and Table 21. The PX303 sensor signal ranges from 1-11 Vdc, but the NI PC6224 is limited to 10.5 Vdc. Therefore, though the sensors can safely operate at 100 psig, they cannot accurately transmit data at that range due to limitations of the data acquisition system. Since the rig is to be limited to 90 psig this should never be an issue.

Table 20: PX303 Calibration Data: Channels 2 and 3

Nominal (psig)	Channel 2 (V)			Channel 3 (V)		
AVERAGE	MEAN	SD	SNR	MEAN	SD	SNR
20	3.003	0.001495	2009	2.999	0.001328	2259
40	4.981	0.000651	7648	4.993	0.000647	7712
60	6.949	0.001267	5486	6.967	0.001266	5502
80	8.930	0.001042	8570	8.961	0.001065	8413
100						

Table 21: PX303 Calibration Data: Channels 4 and 5

Nominal (psig)	Channel 4 (V)			Channel 5 (V)		
AVERAGE	MEAN	SD	SNR	MEAN	SD	SNR
20	2.991	0.001531	1954	3.006	0.001421	2116
40	4.977	0.000614	8099	4.988	0.000582	8563
60	6.953	0.001268	5484	6.962	0.001284	5423
80	8.942	0.001044	8568	8.949	0.001023	8746
100						

The PX303 sensor signal ranges from 1-11 Vdc, but the NI PC6224 is limited to 10.5 Vdc. Therefore, though the sensors can safely operate at 100 psig, they cannot accurately transmit data at that range

due to limitations of the data acquisition system. Since the rig is to be limited to 90 psig this should never be an issue. The following table, Table 22, shows the calibration data for the PX209 sensors.

Table 22: PX209 Calibration Data: Channels 6 and 7

Nominal (psig)	Channel 6 (V)			Channel 7 (V)		
AVERAGE	MEAN	SD	SNR	MEAN	SD	SNR
20	2.071	0.006742	307	2.082	0.008189	254
40	4.076	0.00802	508	4.072	0.008399	485
60	6.059	0.007112	851	6.051	0.008484	713
80	8.047	0.007058	1140	8.037	0.009759	824
100	9.997	0.010808	924	10.000	0.013343	749

Since the PX209 sensors have a 0-10 Vdc range, the readings at 100 psig were acceptable. However, the PX209 sensors are significantly noisier than the PX303. This trend is continued with the PX219 sensors, the data for which may be seen below in Table 23. Channels 8 and 10 were checked, but the sensors themselves seemed to be flawed, as they would not function with the calibration unit either.

Table 23: PX219 Calibration Data: Channels 9 and 11

Nominal (psig)	Channel 9 (V)			Channel 11 (V)		
AVERAGE	MEAN	SD	SNR	MEAN	SD	SNR
20	1.039	0.005432	191	1.003	0.004463	224
40	2.013	0.006144	328	2.004	0.004973	403
60	3.019	0.004053	745	3.005	0.005037	597
80	4.024	0.004089	984	4.006	0.00464	863
100	5.009	0.005972	838	4.994	0.005502	907

Channels 8 and 10 were checked, but the sensors themselves seemed to be flawed, as they would not function with the calibration unit either. The Handheld Calibration Data is recorded here in Table 24.

Table 24: CA150 Handheld Calibration Unit Pressure Sensor Data

Nominal (psig)	Over 60 Seconds	
AVERAGE	START	FINISH
20	1.006	1.001
40	2.008	2.004
60	3.007	2.995
80	4.006	4.004
100	5.007	4.984

The slight decrease is most likely due to slight leaks, signal noise, and minor temperature changes. Channel 1 was not calibrated and is the PX219 30 psia sensor used for measuring the ambient pressure in the room. A simple linear gain of three will be used with this sensor. For the other sensors, the following polynomial curve fits was used, found in Table 25 through to Table 27.

Table 25: Pressure Transducer Coefficients: 2 to 4

Coefficient	2	3	4
p_1	-0.0003	-0.0015	-0.0007
p_2	0.0011	0.0262	0.0116
p_3	0.0366	-0.1452	-0.0579
p_4	9.8359	10.3029	10.1525
p_5	-9.8733	-10.1825	-10.1055

Table 26: Pressure Transducer Coefficients: 5 to 7

Coefficient	5	6	7
p_1	-0.000085	0.001084	0.001384
p_2	-0.00210	-0.024	-0.032
p_3	0.0538	0.201	0.265
p_4	9.787	9.328	9.183
p_5	-9.839	0.002133	-0.000115

Table 27: Pressure Transducer Coefficients: 9 and 11

Coefficient	9	11
p_1	0.0474	0.0072
p_2	-0.4988	-0.0622
p_3	1.6941	0.1740
p_4	18.0405	19.8097
p_5	-0.0111	0.0009

The largest standard deviation appears to be 0.013343. This would give a measurement uncertainty of ± 0.13 psi for the PX303 and PX209 sensors, and ± 0.27 psi for the PX219 sensors. However, considering that there was typically a loss of 0.10 psi during each 60 second test, the actual uncertainty at a given instant in time is probably less. The accuracy according to Omega, the manufacturer of the pressure

sensors, is 0.25% Full Scale. This would give an uncertainty of ± 0.25 psi for the PX303 and PX209 sensors and ± 0.50 psi for the PX219 sensors.

2.4.4 Flow Sensors

The thermal flow sensors were calibrated to give a similar output to the Omega FMA-905 series thermal flow sensor. However, this is not a true calibration as the actual state of the Omega sensor is unknown, but seems reasonable. A second Omega flow sensor will require some adjustment to function correctly since it seems to be prone to saturation.

The Omega flow sensor was mounted in the center outlet channel port with one thermal flow sensor mounted downstream. Flow was then passed through at a relative constant rate for 20 seconds, and the signals averaged. Since the Omega sensor does not cover the full range of the other sensors, the calibration curve was performed between roughly 250 SFPM to 2700 SFPM, which should cover the range of normal operation.

For flow rates less than 250 SFPM the thermal flow sensor should be turned off, since it is susceptible to thermal heating. The Omega flow sensors do not seem to have an issue with self heating due to protection circuitry. To convert from SFPM to lb/s for a 2" Schedule 40 pipe, use the following relation. Essentially, this is done by multiplying the flow speed and density at standard conditions with the cross sectional area.

$$U_{s.c.} \times A \times \rho_{s.c.} = \dot{m}$$

$$1 \text{ SFPM} = 1 \frac{\text{ft}}{\text{min}} \times \frac{1 \text{ min}}{60 \text{ s}} \times \left(\frac{\pi (2.07 \text{ in})^2}{4} \right) \left(\frac{1 \text{ ft}}{12 \text{ in}} \right)^2 \times \frac{0.074887 \text{ lb}_m}{\text{ft}^3} = 2.9169 \times 10^{-5} \frac{\text{lb}_m}{\text{s}} \quad (2.2)$$

Normal operation is therefore 0.0073 lb/s up to 0.079 lb/s. The measurements are shown below for the Channel 2 flow sensor in Table 28.

Table 28: Thermal Flow Sensor Calibration Data: Channel 2

Channel 05 FMA-905 (SFPM)			Channel 02 Thermal Flow Sensor (V)		
MEAN	SD	SNR	MEAN	SD	SNR
260.5	9.6	27	2.098	0.004766	440
554.7	11.4	49	2.460	0.001932	1273
864.0	12.3	70	2.716	0.001880	1445
1115.1	13.6	82	2.952	0.002670	1106
1351.8	18.0	75	3.177	0.002839	1119
1765.5	26.6	66	3.424	0.007383	464
1986.0	25.2	79	3.604	0.012840	281
2495.8	44.4	56	3.805	0.009967	382
2648.2	31.4	84	3.885	0.003457	1124

Channel 1 was roughly calibrated earlier, but should be recalibrated at a later time. The third flow sensor was not immediately needed for the experiments. The sensor was curve fitted with a fourth order polynomial, for which the coefficients are shown below in Table 29.

Table 29: Thermal Flow Sensor Polynomial Coefficients: Channel 2

Coefficient	2
p_1	277
p_2	-3093
p_3	13163
p_4	-23570
p_5	15413

The accuracy of the measurement for the FMA905 is 1.5% of the full scale. So for a sensor with a range up to 5000 SFPM, it is accurate to ± 75 SFPM. Since there is no manufacturer's data, and the rudimentary flow scheme used, the measurements for the thermal sensor will be assumed to have the same uncertainty as the FMA-905.

2.4.5 Potentiometers

Only two of the actuators were calibrated at this time, and only three were operational at the time of this writing. The bottom channel had a functioning T and bleed channel valve, while the outflow valve was also operational. The top channel and the two ram air channels did not have any operational valves due to poor alignment in the case of the Tee valve, and poor mating adapter sizing for the other three valves. This section explains the method used to calibrate the bottom bleed channel valve and the outflow valve.

The first step was to set the closed position by commanding 4 mA and adjusting the zero setscrew position until the shaft visually appeared to be at 0°. The supply valve was then opened to listen for any leaks past the valve. The full open position was similarly set using a 20mA signal and adjusting the span setscrew until the shaft visually appeared at 90°. The valve was then commanded back and forth between the full open and full closed positions with pauses while the deadband was adjusted. Essentially the smallest deadband possible was used that did not permit jitter.

Since the command signal ranged from 4 mA to 20 mA for an angle of 0° to 90°, the following conversion was used to convert desired angle to the command signal.

$$y[\text{mA}] = x[^\circ] \left(\frac{16[\text{mA}]}{90[^\circ]} \right) + 4[\text{mA}] \quad (2.3)$$

To calibrate the potentiometer, the valve was commanded first to 0°, and a reading was taken over a period of time to collect a mean reading with a standard deviation. The valve was then opened by 10°, and the mean and standard deviation were taken again. The valve was then fully closed before being opened to 20° and more measurements were taken. This process was repeated to 90° at which point readings started to be taken in the closing direction. For example, after the measurements for 90° were taken, the valve was closed to 80° and readings were taken. After which, the valve was fully opened,

before being closed to 70°. The measurements taken for both the outflow and bottom bleed channel valves are shown in Table 30.

The small differences in voltage for the same commanded angle are due to the deadband and hysteresis. With a larger deadband, the differences are much greater, as was noticed on earlier calibration attempts. An average of the opening and closing values was used to develop the polynomial to convert from the signal voltage to degrees and is shown in Table 31..

Table 30: Valve Calibration Data for Bottom Bleed and Outflow Channels

Command	BB (V)			O (V)		
	Mean	SD	SNR	Mean	SD	SNR
0	3.461	0.0002370	14605	2.980	0.0002354	12662
10	3.716	0.0002591	14342	3.228	0.0002388	13519
20	4.017	0.0002422	16587	3.538	0.0002403	14720
30	4.324	0.0002518	17175	3.842	0.0002372	16197
40	4.632	0.0002585	17917	4.148	0.0002320	17876
50	4.939	0.0002697	18313	4.454	0.0002381	18705
60	5.246	0.0002751	19069	4.769	0.0002329	20482
70	5.553	0.0002633	21086	5.067	0.0002382	21269
80	5.859	0.0002507	23375	5.372	0.0002408	22309
90	6.167	0.0002434	25332	5.678	0.0002397	23693
80	5.860	0.0002343	25011	5.368	0.0002422	22161
70	5.555	0.0002329	23855	5.066	0.0002414	20989
60	5.247	0.0002431	21590	4.764	0.0002403	19821
50	4.941	0.0002374	20814	4.459	0.0002595	17180
40	4.635	0.0002360	19643	4.153	0.0002362	17582
30	4.327	0.0002536	17064	3.847	0.0002297	16751
20	4.020	0.0002394	16795	3.543	0.0002375	14919
10	3.714	0.0002420	15345	3.233	0.0002389	13530
0	3.461	0.0002370	14605	2.980	0.0002349	12686

Table 31: Average Calibration Data for Bottom Bleed and Outflow Channels.

	BB(V)	O (V)
Command	Average	Average
0	3.461	2.980
10	3.715	3.231
20	4.019	3.540
30	4.326	3.845
40	4.633	4.150
50	4.940	4.456
60	5.247	4.766
70	5.554	5.066
80	5.860	5.370
90	6.167	5.678

The fifth degree polynomial coefficients that were determined using the MATLAB curve fitting tool are given in Table 32.

Table 32: Polynomial Coefficients for Bottom Bleed and Outflow Valves

Coefficient	Bottom Bleed	Outflow
p_1	0.576	0.545
p_2	-14.451	-12.452
p_3	144.037	112.844
p_4	-712.503	-506.275
p_5	1781.342	1156.647
p_6	-1814.337	-1083.033

The uncertainty of the potentiometers is approximately $\pm 0.25^\circ$. However, the minimum change in command signal, or the deadband, that will move the actuators has a minimum setting of 0.12% of the full scale, which is roughly $\pm 0.108^\circ$. The deadband has been increased slightly above this to eliminate the valve from oscillating rapidly, or jittering, about the set point, which can drastically reduce the lifespan of the motor and gearbox. The uncertainty of the potentiometers may be due to resistor tolerances, hysteresis, inaccuracies of the actuator control, or simply the deadband of the actuator.

2.5 Software

The core of the data acquisition and control software is the MATLAB SIMULINK Real-Time Windows Target Toolbox. This 32-bit virtual toolbox allows SIMULINK to interact with the sensors and actuators via the National Instruments boards installed in the computer. A relatively rudimentary control system has been put in place to aid in calibration and testing of the rig. This control system provides a basic modular structure of the software that can be easily updated or altered by future students. This basic system is composed of four subsystems and is shown in Figure 29:

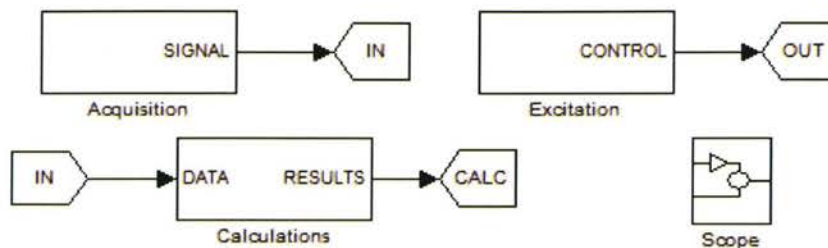


Figure 29: SIMULINK Overall Control System

The acquisition subsystem is responsible for acquiring data from the sensors in the system and converting the measurements from voltage signals to engineering units via the calibration tables from Section 2.4. The engineering values are routed to a common data stream which may then be used for control, calculations, or display. Figure 30 shows the block assembly that retrieves data acquired by the PCI-6034E card.

The Analog Input block is from the Real-Time Windows Target, and controls both the sampling rate and the channels to be sampled. It outputs a multiplexed signal, which is then split before conversion to engineering units via polynomial or gain. Each data stream is then labeled by channel number and a letter prefix that denotes the sensor type and output as a bus with other common measurements.

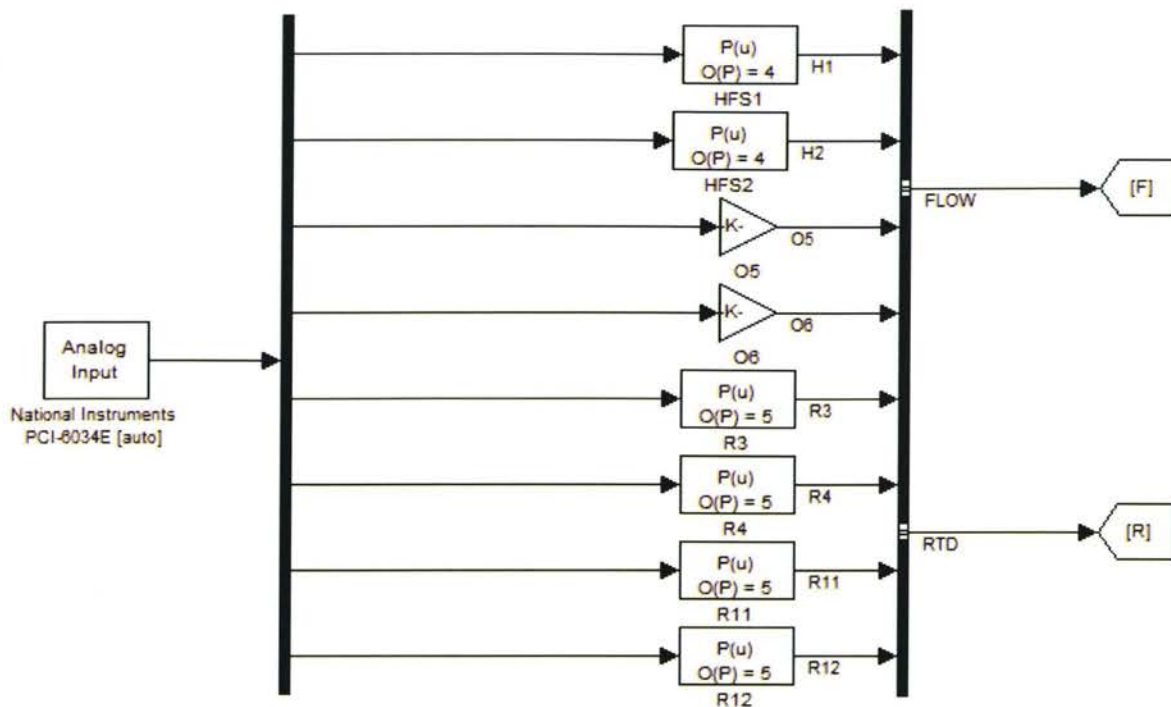


Figure 30: SIMULINK NI PCI-6034E Data Acquisition

The letter prefixes used in the control system are as follows:

- ❖ P – Pressure Sensor
- ❖ T – Thermocouple
- ❖ A – Actuator Potentiometer
- ❖ H – Thermal Flow Sensor
- ❖ O – Omega Flow Sensor
- ❖ R – RTD
- ❖ C – Actuator Control Signal
- ❖ E – RTD Excitation

The acquisition block also contains the NI PCI-6224 Analog Input block and the conversion polynomials or gains for all of its channels. Both cards sample data at a rate of 1000 samples per second on each channel. No filtering or down sampling is performed in this subsystem at this time. Polynomial conversions are typically used where the sensor has been calibrated as was mentioned previously. The gain conversions are used in sensors that have not yet been calibrated, specifically the ambient pressure

sensor and Omega Flow sensors. However, these sensors do have a manufacturer's calibration sheet, and their output seems reasonable.

The excitation block is the primary control of the rig. At the moment, it is comprised of discrete PID controllers for automatic control, and a slider gain for manual control. Selection between automatic and manual is done by a manual control switch. Currently, only the bottom bleed and outflow channels are operational. Work has been done on the top and bottom Tee valves. The other three valves are in place for future use. Figure 31 shows the current block arrangement, with the Real-Time Windows Target Analog Output being used to interface SIMULINK with the NI card, and thus the actuators.

The current setup shown would have the bleed air controlling downstream pressure to 20 psig, and the outflow controlled to 1000 SFPM. Both manual switches are selected to automatic control, but the valves would immediately begin to close if the switch were flipped over to manual. The bottom four constants are used to excite the RTDs with a 5 mA current. All of the data is multiplexed, before being passed through a saturation block that limits the output to 4-20 mA. As more controllers are added, it may be beneficial to place the individual controller and their supporting elements into a subsystem, but leave the switches and manual controls readily accessible.

Data is averaged over the previous ten samples before entering the PID Controller. The bottom bleed controller samples data every 1ms, and has an output limited between 0° and 90° with proportional gain of 2.5 and an integral gain of 1. The outflow controller has a similar layout, but with a proportional gain of 0.003 and an integral gain of 0.001. These gains were tuned experimentally with feedback provided by a PX219 pressure sensor and a FMA905 flow sensor, and control performance will be shown later.

The Scope block essentially allows for the real-time display of data and is highly subject to change based on the test being performed and what variables need to be monitored. Essentially all data channels are connected here in a single bus, such that they can be displayed or recorded as necessary. For display



The DATA scope is used to record and output all desired data as an array to the MATLAB workspace. This data may then be saved permanently using the *xlswrite* or *csvwrite* commands in MATLAB. These commands allow the data to be used by Microsoft Excel. The other four scopes serve as displays that show the current data as a moving plot, but do not record data.

The Calculations subsystem is intended to be the virtual sand box where any calculations or real-time data manipulation may be performed without interfering or confusing the core control blocks. The output of this block may be displayed, recorded, or used for control purposes as needed. This system has the potential to become very complex, so it is important to keep things organized as much as possible.

As mentioned previously, several samples of the control system in action will be shown here. Since the program records blocks of 180s worth of data, the first 180s are used for test initialization and stabilization, with the actual test being performed between 180s and 360s. For all tests, the supply pressure was regulated to 60 psig. The first test, the load pressure was to be maintained at 20 psig, while the outflow was varied from 1000 SFPM to 1500 SFPM and back down to 1000 SFPM. Figure 33 and Figure 34 show the results.

Flow response seems slow, approximately 50s to increase flow to 1500 SFPM and roughly 30s to decrease flow back to 1000 SFPM. However, this is necessary to avoid oscillations about the set point due to the large fluctuations in the flow measurement signal from the FMA905 flow sensor. Additionally, rapid changes in flow rate can result in large pressure losses, which may cause harmful response upstream as it tries to compensate. Therefore, though it is slow and may be improved, the flow control does work.

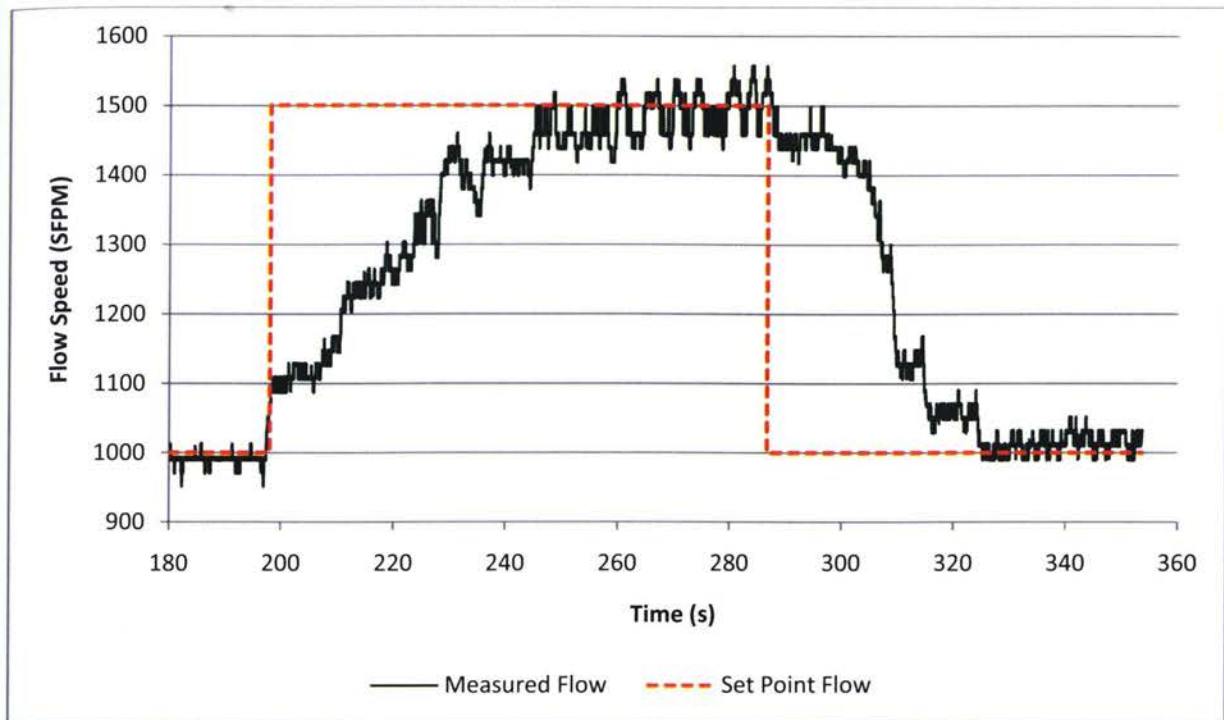


Figure 33: Control System Demonstration: Varying Flow with Constant Pressure, Flow Plot

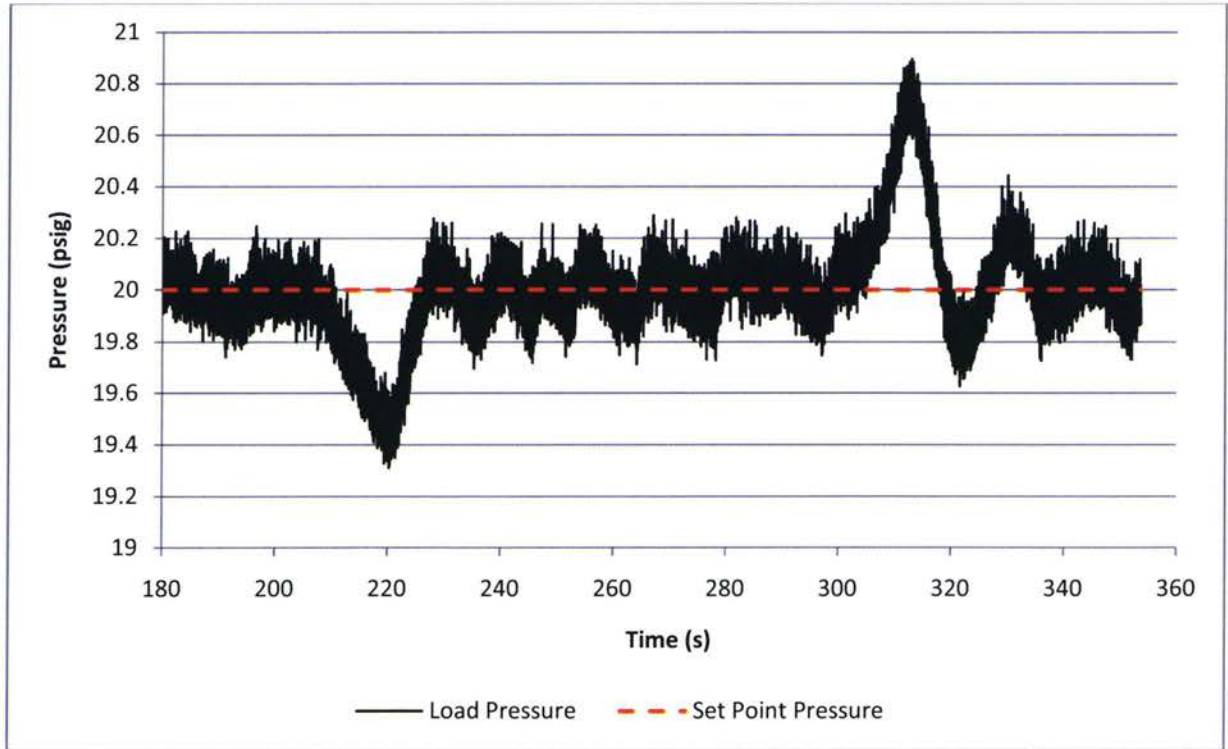


Figure 34: Control System Demonstration: Varying Flow with Constant Pressure, Pressure Plot

Pressure control seems much better, with the controller maintaining 20 psig ± 1 psi for the entire duration of the test. Relatively large changes with under damped response can be seen at times where the outflow valve has changed position to adjust for a new commanded outflow. The bottom bleed valve had to compensate for the corresponding pressure loss when the flow rate increased and pressure gain when the flow rate decreased. Considering the PX219 sensor used for control feedback has a ± 0.25 psi error, the system maintains 20 psig set point very well.

The second test involves maintaining 1000 SFPM while varying pressure from 20 psig up to 25 psig and back down to 20 psig. The plots of the tests are shown in Figure 35 and Figure 36. Pressure responds much faster with respect to changes in flow rate, especially during an increase in pressure. Reducing the pressure is limited to the outflow rate of air, which is why the slope is why the response appears to be linear until the controller responds to the overshoot. Overshoot peaks in both increase and decreasing at approximately 3 psi, with the response damping down to within a range of ± 1 psi within 40 seconds. Overall, the flow rate remains constant within ± 150 SFPM of the set point.

The third test involves changes in both the flow and pressure set points. Initially, flow and pressure are maintained at 1000 SFPM and 20 psig respectively. Next, both are increased to 1500 SFPM and 25 psig nearly simultaneously. Finally, the flow and pressure are decreased to their original values of 1000 SFPM and 20 psig respectively. Overall, from Figure 37 and Figure 38, the response seems very similar to the first and second tests, but it demonstrates that the control system is capable of handling both pressure and flow independently and simultaneously.

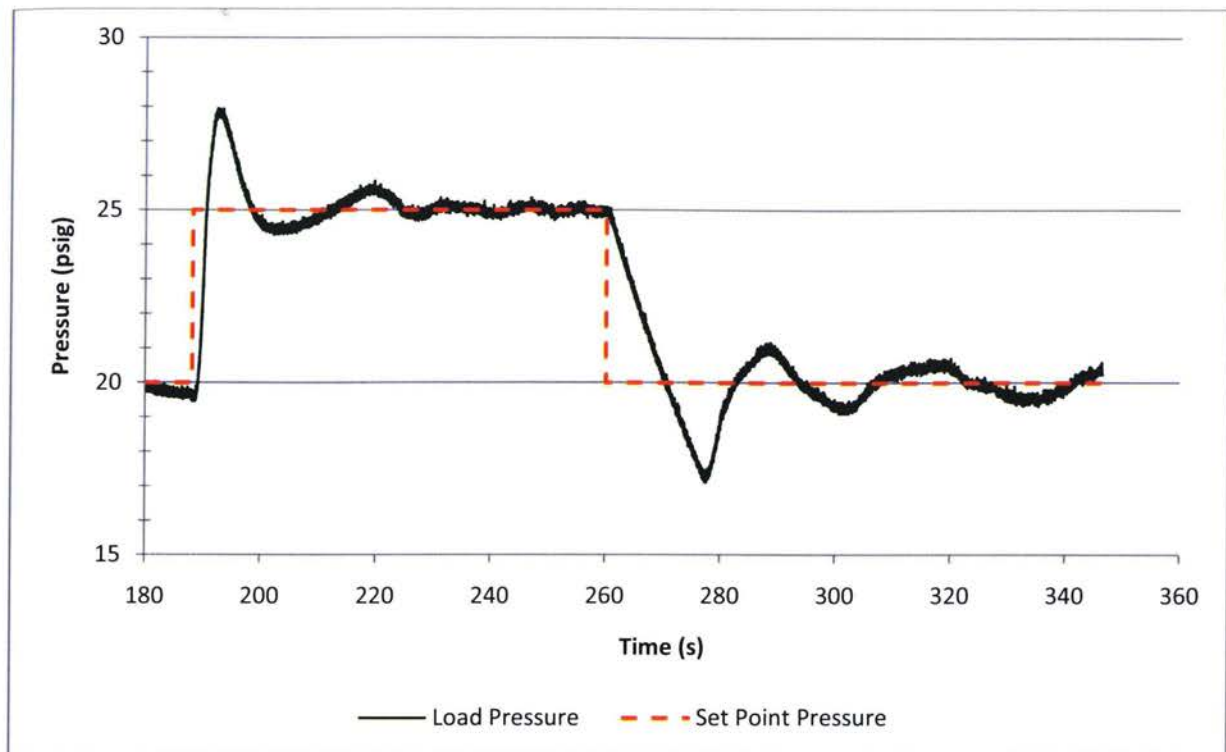


Figure 35: Control System Demonstration: Constant Flow with Varying Pressure, Pressure Plot

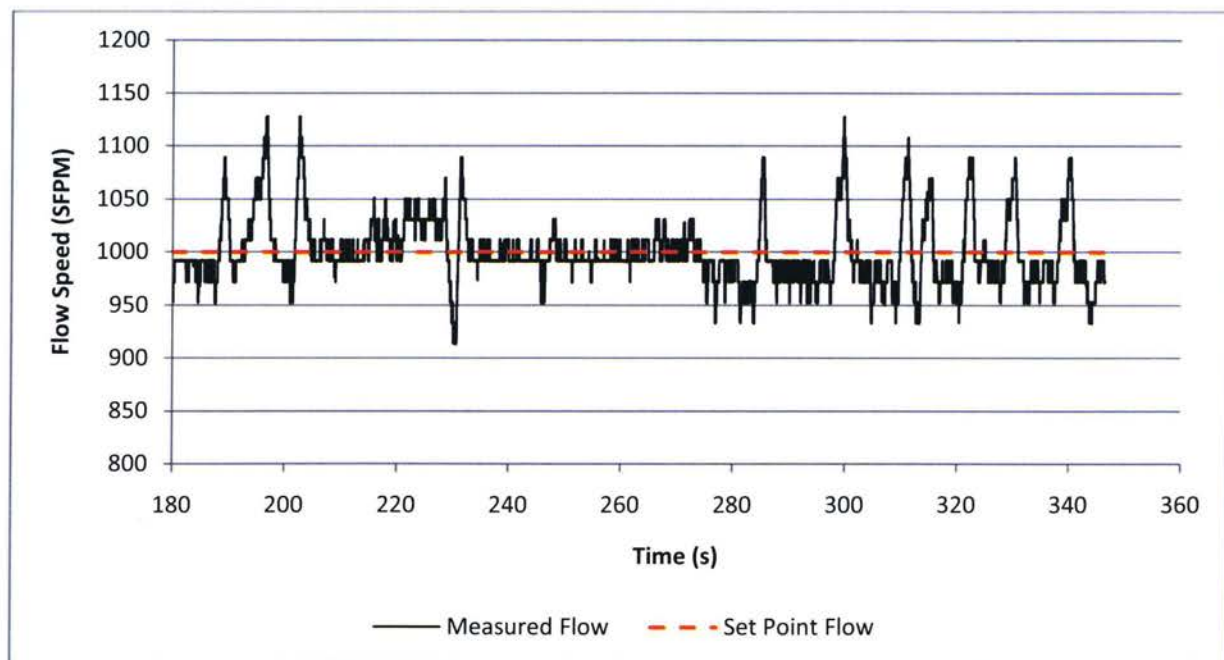


Figure 36: Control System Demonstration: Constant Flow with Varying Pressure, Flow Plot

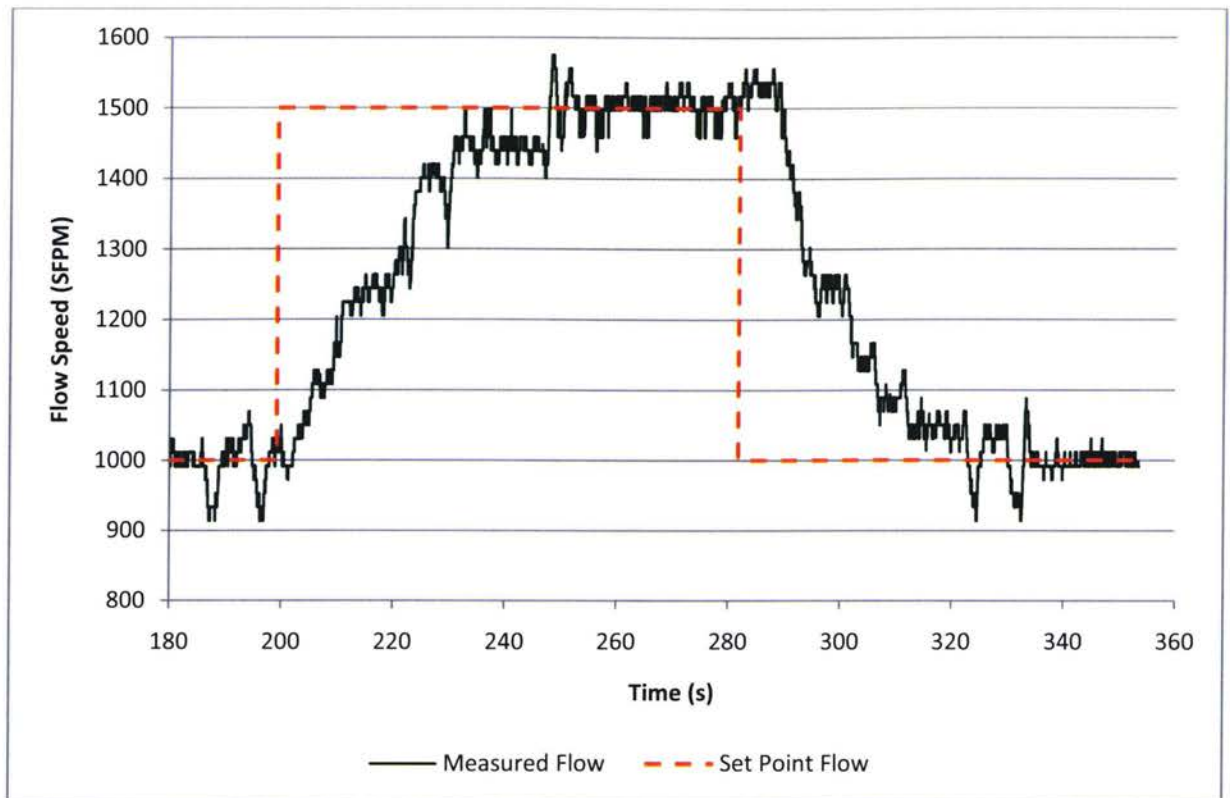


Figure 37: Control System Demonstration: Varying Flow and Pressure, Flow Plot

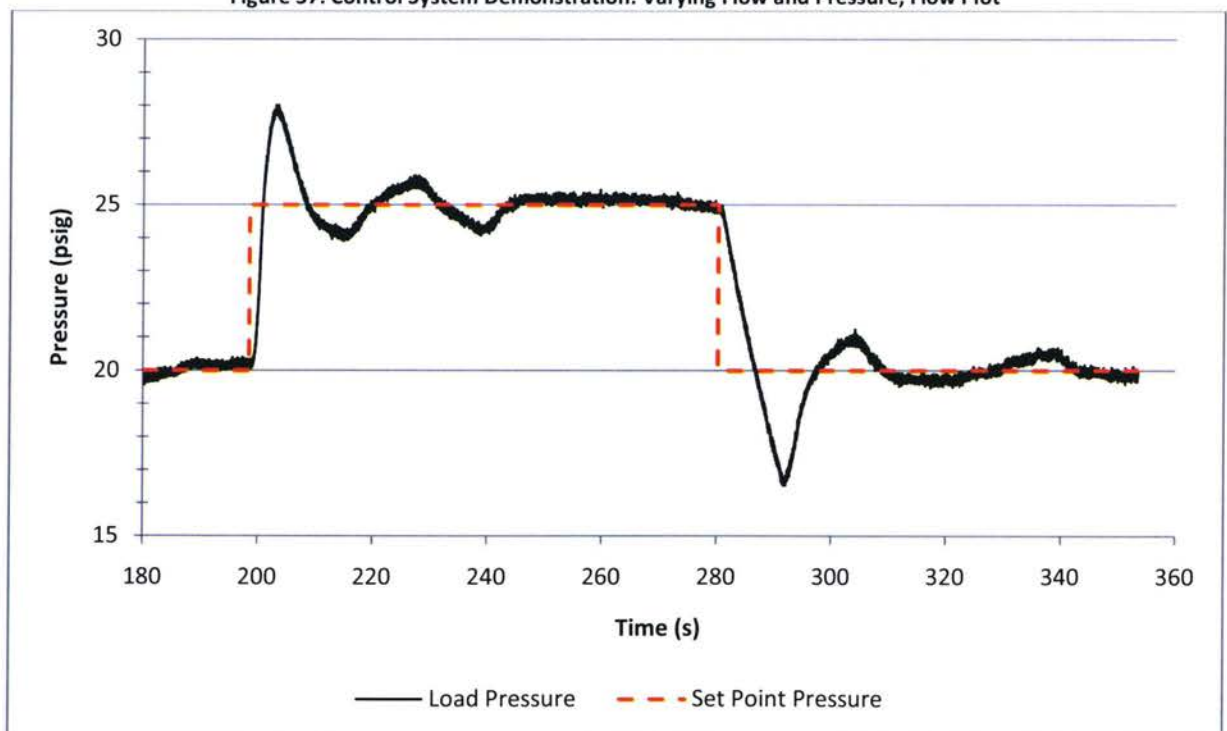


Figure 38: Control System Demonstration: Varying Flow and Pressure, Pressure Plot

3 Theoretical Model

In order to develop a methodology for improving flow measurement using other sensors in a channel, a theoretical model needed to be developed based on the sensors and channel to be used for the experimental test. The primary purpose of improving flow measurement is one means of improving the master-slave flow sharing algorithm developed by Bao (Bao, 2003). This algorithm relies on the measured flow of the master channel as the set-point for the mass flow for the slave channels. The slave channel control signal relies on the difference between the master and slave channel mass flow rates. Any form of sensor lag results in a slower response in the slave channel resulting in errors in flow sharing.

Several steps will be taken in the development of a theoretical model. First, the thermal flow sensor will be modeled since it is the chief sensor involved in the master-slave control scheme. Second, an orifice plate flow meter model will be developed to compare to the thermal flow sensor. When these models are completed, the errors relevant to each model will be explained and the estimation algorithm will be developed that takes advantage of the performance of each sensor. Third, a simple model of the channel to be used will be developed, and this model will be used to mimic an orifice plate flow meter. Finally, the estimation algorithm will be modified to accept the channel model.

A line diagram of the bleed air channel is shown below in Figure 39. It shows the relevant locations of the sensors and valves to be used as well as the notation that will be used hereafter.

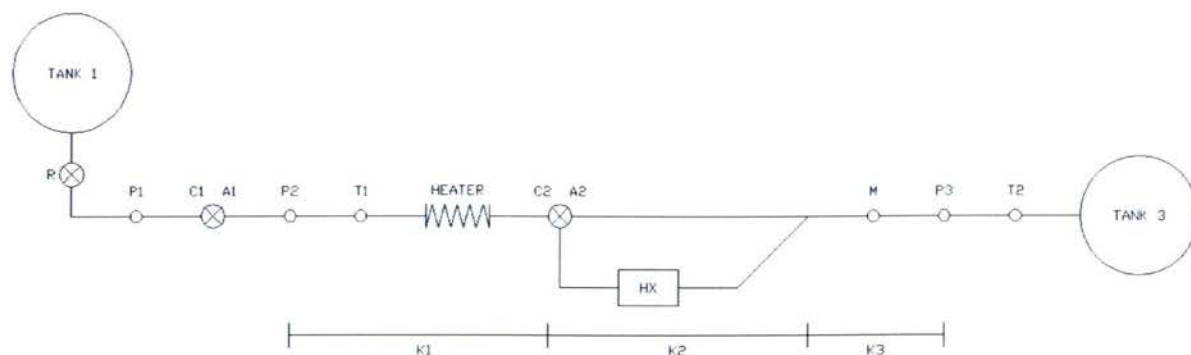


Figure 39: Bleed Line Diagram with Notation

R	Manual Valve	HX	Heat Exchanger
P1	PX219-200G10V	M	Flow Sensor
C1	Control Valve Command Signal	P3	PX303-100G10V
A1	Control Valve Output Signal	T2	Resistance Temperature Detector
P2	PX303-100G10V	TANK 1	Supply Air Tank
T1	Thermocouple (T-Type)	TANK 2	Load Air Tank
HEATER	Inline Heater	K1	Section 1 Pressure Drop Coefficient
C2	Splitter Valve Command Signal	K2	Section 2 Pressure Drop Coefficient
A2	Splitter Valve Output Signal	K3	Section 3 Pressure Drop Coefficient

The portion of the line to be modeled falls between P2 and P3. The flow is assumed to be isothermal, and is assumed to be equal to the temperature found at T2. The heater, if present, is simply used as an additional resistance. For experiments C1 will be used for controlling the flow rate through the channel, and C2 will be used to vary the pressure drop in the channel. This essentially means that the pressure drop coefficient of Section 2 will be variable depending on the position of valve C2. The pressure drop coefficients across Sections 1 and 3 should be relatively constant. If the position of valve C2 remains constant, the problem essentially could be simplified as an equivalent orifice plate flow meter.

3.1 Thermal Flow Sensor Model

The thermal flow sensor was thoroughly studied at Ryerson University by Yiu in 2004 (Yiu, 2004). The model developed here is derived from previous work at the University with consideration to the work by Olin (Olin). Olin considers convection and conduction as relevant means of heat loss from the flow

sensors, whereas Yiu considered convection alone. However, Olin requires several empirical calibration values in his final result which does not make his method conducive to theoretical model. However, he does specify that in well designed sensors, conduction losses range between 10 and 15% of the power applied to the sensor, and that these losses are reduced as the flow speed increases.

Figure 40, which is shown below, is a simplified view of how a thermal flow sensor is mounted in a channel. The mass of air flowing past the sensor will directly affect the temperature of the heated sensor. More power will be added to the heated sensor until a set temperature difference is maintained between the ambient temperature sensor, which measures the actual flow temperature, and the heated temperature sensor. The power required to maintain the temperature difference can be directly correlated to the mass flow rate, as the theory of this section demonstrates.

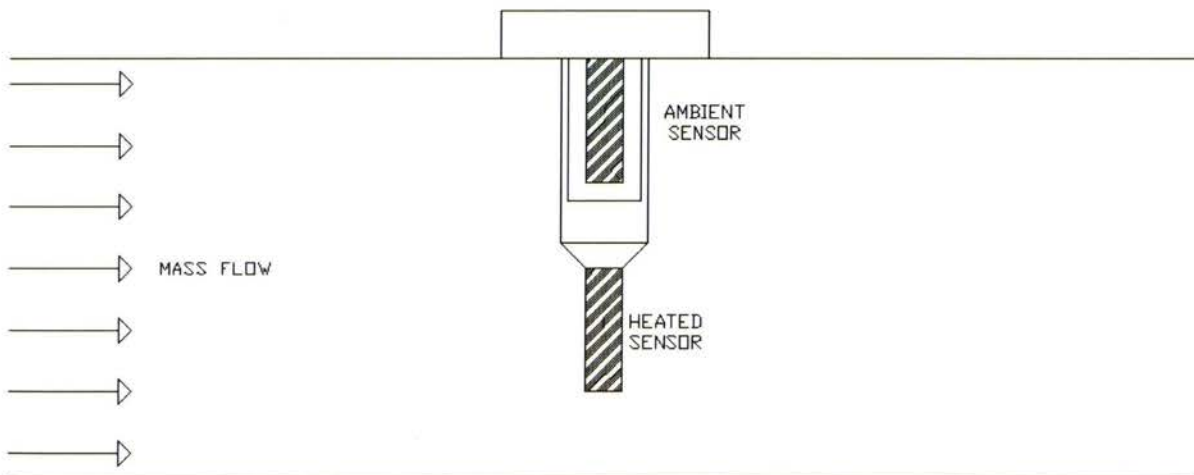


Figure 40: Diagram of a Thermal Flow Sensor

The basic equation defining the heat losses due to convection and conduction of the heated sensor is shown below. The sensor is mounted on the end of a probe which is assumed to be the same diameter of the sensor.

$$P - \left(\frac{kA_C}{L_1} + A_S h_\infty \right) (T_H - T_\infty) = mc \frac{dT_H}{dt} \quad (3.1)$$

- ❖ P Electrical Power [W]
- ❖ $A_S = \pi d L_S + \pi d^2/4$ Heated Sensor Surface Area [m^2]
 - d Sensor Diameter [m]
 - L_S Sensor Length [m]
- ❖ h_∞ Convective Heat Transfer Coefficient [$\text{W}/(\text{m}^2 \cdot \text{K})$]
- ❖ k Thermal Conductivity of Probe Material [$\text{W}/(\text{m} \cdot \text{K})$]
- ❖ $A_C = \pi d^2/4$ Sensor and Probe Cross-Sectional Area [m^2]
- ❖ L_1 Length from sensor to base [m]
- ❖ T_H Heated Sensor Temperature [K]
- ❖ T_∞ Free Stream Temperature [K]
- ❖ m Mass of Sensor Body [kg]
- ❖ c Specific Heat Capacity of Sensor Body [$\text{J}/(\text{kg} \cdot \text{K})$]
- ❖ dT_H/dt Rate of Change of Heated Sensor Temperature with respect to time [K/s]

The design of the flow sensor attempts to thermally isolate the ambient sensor from the heated sensor.

Conduction will be considered to be negligible for the ambient sensor.

$$A_S h_\infty (T_A - T_\infty) = mc \frac{dT_A}{dt} \quad (3.2)$$

- ❖ $A_S = \pi d L_S + \pi d^2/4$ Ambient Sensor Surface Area [m^2]
- ❖ T_A Ambient Sensor Temperature [K]

❖ dT_A/dt Rate of Change of Ambient Sensor Temperature with respect to time [K/s]

In following the methodology by Yiu, the Laplace transforms of Equations (3.1) and (3.2) are taken and the resulting equations rearranged to solve for the sensor temperature.

$$T_H = \frac{P}{mc \cdot s + \frac{kA_C}{L_1} + A_S h_\infty} + \frac{\left(\frac{kA_C}{L_1} + A_S h_\infty \right) T_\infty}{mc \cdot s + \frac{kA_C}{L_1} + A_S h_\infty} \quad (3.3)$$

$$T_A = \frac{A_S h_\infty T_\infty}{mc \cdot s + A_S h_\infty} \quad (3.4)$$

The temperature difference between the two sensors is in turn given by the following equation.

$$\Delta T = T_H - T_A = \frac{P + \left(\frac{kA_C}{L_1} + A_S h_\infty \right) T_\infty}{mc \cdot s + \frac{kA_C}{L_1} + A_S h_\infty} - \frac{A_S h_\infty T_\infty}{mc \cdot s + A_S h_\infty} \quad (3.5)$$

If conduction is neglected then the thermal conductivity would equal zero, which would give the following equation.

$$\Delta T = \frac{P + A_S h_\infty T_\infty}{mc \cdot s + A_S h_\infty} - \frac{A_S h_\infty T_\infty}{mc \cdot s + A_S h_\infty} = \frac{P}{mc \cdot s + A_S h_\infty} \quad (3.6)$$

This is the same result used by Yiu.

The above equations all rely on the convective heat transfer coefficient, which is not readily available and is heavily reliant on the experimental conditions. However, there are methods of approximating the coefficient to roughly 20% accuracy. Incropera provides an equation relying only on the Reynold and Prandtl numbers of the flow being measured. Note that the flow is considered to be around a circular

cylinder in cross flow. The actual sensor has a complex shroud and is no way an ideal cylinder. The equation shown below provides the mean Nusselt number for the flow (Incropera & DeWitt, 2002).

$$\overline{Nu}_d = 0.3 + \frac{0.62 \cdot Re_d^{1/2} \cdot Pr^{1/3}}{\left[1 + (0.4 / Pr)^{2/3}\right]^{1/4}} \left[1 + \left(\frac{Re_d}{282,000}\right)^{5/8}\right]^{4/5} \quad (3.7)$$

This equation was developed by Churchill and Bernstein, according to Incropera, and may be used when $Re_d \cdot Pr > 0.2$. If the relation is false, it was assumed that forced convection was negligible for the given flow condition, and the Nusselt number was set to zero. The Nusselt number may be converted to the convective heat transfer coefficient using:

$$h_\infty = \bar{h} = \frac{\overline{Nu}_d \cdot k_f}{d} \quad (3.8)$$

To calculate the Nusselt number, Reynolds number with respect to the sensor diameter is needed. This is given by the following equation.

$$Re_d = \frac{\rho U d}{\mu} \quad (3.9)$$

❖ U Bulk Flow Velocity [m/s]

SIMULINK was used to model the sensor using a step mass flow input. Most of the physical values used were discussed by Yiu. The relevant values are reproduced below. The lengths are approximated since the sensor is proprietary. The sensor has a range up to 0.5 kg/s, and is mounted in a 2" Schedule 40 steel pipe which has an actual internal diameter of 2.07" (0.0526m). The following information about the mounting of the sensor incorporates data from Incropera at a temperature of 300 K. For the purpose of

this model, the airflow is assumed to be close to atmospheric pressure and at a constant temperature of 300 K. The heated sensor probe is assumed to be mounted on nylon insulator.

Table 33: Flow Sensor Physical Parameters Relevant to Model

Parameter	Quantity	Units
Sensor Mass m	1.2320e-4	kg
Specific Heat Capacity c	393.9	J/(kg · K)
Sensor Length L_s	1e-2	m
Sensor Diameter d	3e-3	m
Distance from Heated Sensor to Base L_1	1e-2	m
Gas Conductivity k_f	26.3e-3	W/(m · K)
Air Density ρ	1.1614	kg/m ³
Air Viscosity μ	184.6e-7	(N · s)/m ²
Sensor Probe Conductivity k	0.25	W/(m · K)
Prandtl Number Pr	0.707	
Actual Pipe Cross-Sectional Area A_p	2.17e-3	m ²

For modeling the sensor in SIMULINK, Equations (3.1) and (3.2) were integrated with respect to time, which gave the following equations:

$$T_H = \int \frac{1}{mc} \left[P - \left(\frac{kA_c}{L_1} + A_s h_\infty \right) (T_H - T_\infty) \right] dt \quad (3.10)$$

$$T_A = \int \frac{1}{mc} \left[A_s h_\infty (T_A - T_\infty) \right] dt \quad (3.11)$$

From Yiu, the maximum power allowable is 5.42 W, with a maximum current of 0.333 A across a resistance of 48.8Ω. A 0-5V output signal was assumed, normalized with the power output of the controller. This signal was calibrated to the standardized flow speed from the steady state samples shown in the table below. Note that it was assumed that ambient temperature remains constant at 300 K. Standard conditions used in the conversion to flow speed are ISA+20°C or 293.15 K, 1.2041 kg/m³, and 101325 Pa. Since ambient temperature remains constant, the ambient sensor reading does not

experience any temperature change due to convection. Therefore no heat loss or net temperature change is observed in the ambient sensor in this simulation.

Table 34: Simulated Thermal Flow Sensor Data

Mass Flow (kg/s)	Flow Speed (SFPM)	Reynolds Number	Heated Sensor (W)			Signal (V)
			Conduction	Convection	Power	
0.002	151	150	0.007	0.222	0.229	0.2122
0.005	377	374	0.007	0.347	0.354	0.3277
0.015	1129	1123	0.007	0.600	0.607	0.5622
0.020	1506	1497	0.007	0.695	0.702	0.6496
0.025	1882	1871	0.007	0.779	0.786	0.7274
0.045	3388	3368	0.007	1.056	1.063	0.9845
0.135	10170	10100	0.007	1.906	1.913	1.7710
0.225	16940	16840	0.007	2.538	2.545	2.3569
0.315	23720	23580	0.007	3.083	2.090	2.8615
0.410	30870	30690	0.007	3.604	3.611	3.3433
0.500	37650	37420	0.007	4.062	4.069	3.7678
0.720	54210	53890	0.007	5.091	5.098	4.7203

According to Yiu, the maximum flow rate is reported to be approximately 200 lb/min for a 3" diameter duct, which converts to a standard flow speed of approximately 54,200 SFPM. From the table above, this approximation appears to be verified by the model. However, the model by Yiu reports a full signal of 5.4 W at 1.1 lb/s which is roughly 0.5 kg/s for a 2" diameter duct, but it is believed that the pipe diameter was used in calculations where sensor diameter should have been used. Interesting to note is the linear relationship between the maximum power of the sensor at 5.42 W and the maximum flow speed of 54,200 SFPM. Regardless, if the numbers are correct, the error of the model at maximum flow speed is only 6.4%, which considering the uncertainty of the Churchill-Bernstein equation is remarkably acceptable.

The losses due to conduction in the model are steady throughout, which makes sense considering the temperature difference is constant at steady state. However, the loss of 0.007 W is low, considering a well designed sensor is expected to have 10 to 15% heat loss due to conduction. A larger heat loss due

to conduction could easily push the required power beyond 5.42 W. However, the low heat loss due to conduction is considered acceptable when compared to past assumptions regarding flow sensors. Also, losses due to conduction seem to only offset the required power for flow at steady state.

Additionally, due to the proprietary nature of the sensor, extremely detailed thermal analysis of the probe was avoided as can be seen by the approximate nature of the physical dimensions of the sensor. Other sources of error include neglect of conduction on the ambient flow sensor. Intuitively, if no flow is passing across the sensor, conduction then becomes the dominant form of heat transfer and since no insulation is completely ideal, the probe body will gradually heat up, thus resulting in the ambient sensor also heating up. This forms a positive feedback loop that will force the heated sensor to a higher temperature, thus raising the probe temperature further through conduction. This could potentially cause sensor burnout if the sensor is left on without flow for significant periods of time.

The calibration was performed on a sixth order polynomial, the coefficients and plots are shown below in Table 35 and Figure 41.

Coefficient	Flow Speed Model
p_1	-0.0226
p_2	-1.1028
p_3	39.6568
p_4	-507.7506
p_5	4103.8517
p_6	-144.2816
p_7	0.5059

Table 35: Flow Sensor Model Signal Calibration

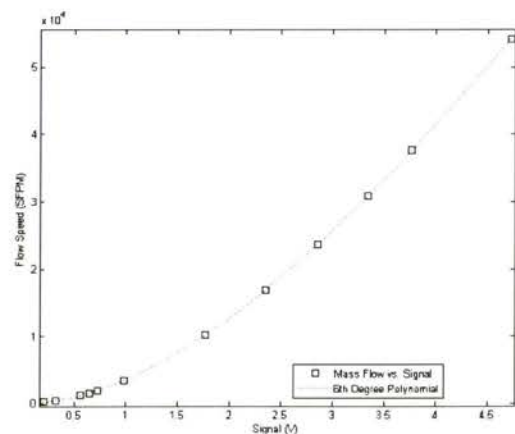


Figure 41: Flow Sensor Model Calibration Curve

At steady state this model settles to within ± 10 SFPM of the actual mass flow experienced by the sensor. The exact dynamic response of the real flow sensor is unknown for a step input. However, other sensors, such as the FMA-900 Series, typically have response times of roughly 0.4s to 63% of the final value, and according to Yiu, thermal flow sensors typically overshoot the steady state value by approximately 6% before damping down to the correct value. Using this information, the model was manually tuned to give similar results. This resulted in a proportional gain of 0.4 with an integral gain of 1.4. The following figure shows a mass flow step at 5s from 0.002 kg/s to 0.500 kg/s.

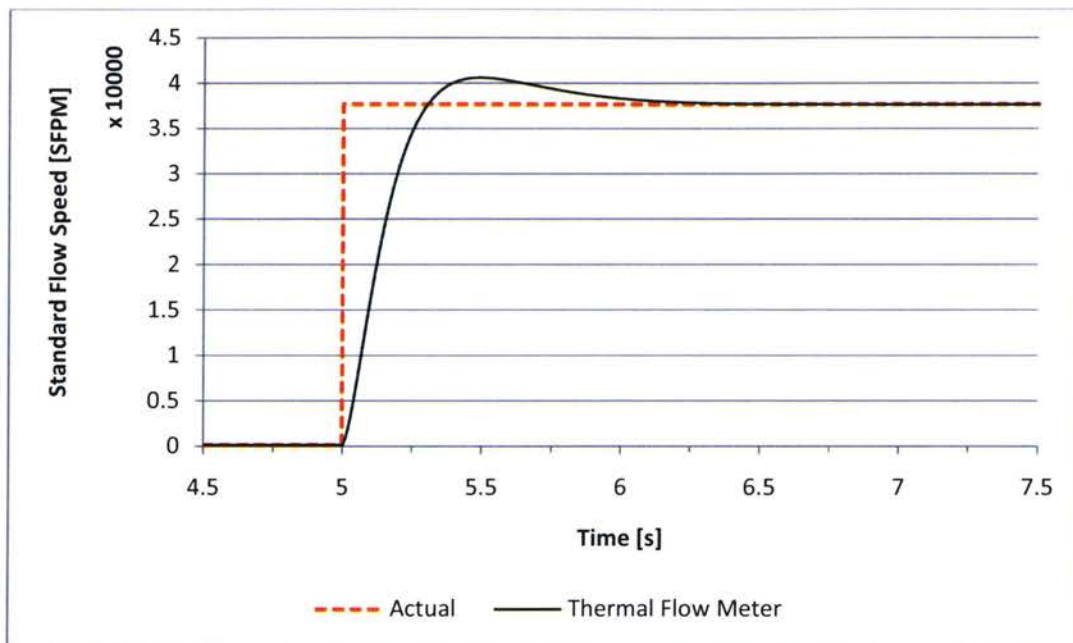


Figure 42: Thermal Flow Meter Response to a Mass Flow Step Change

From above, the maximum overshoot of approximately 8% occurs at 0.5s after the step change, which is acceptable for the purposes of this analysis.

3.2 Orifice Plate Flow Sensor Model

To develop the sensor fusion theory, a sharp edged orifice plate flow meter was used as another means of measuring the mass flow rate. In this case, the actual mass flow will be specified and the pressure

drop across the plate will be calculated. The calculated pressure drop will then be used as if it were an actual measured pressure drop, and the flow rate will be re-calculated. Figure 43 shows a basic orifice plate flow meter installation, with pressure taps located at 1 diameter upstream and 0.5 diameters downstream. Temperature of the flow is assumed to be either known or measured elsewhere.

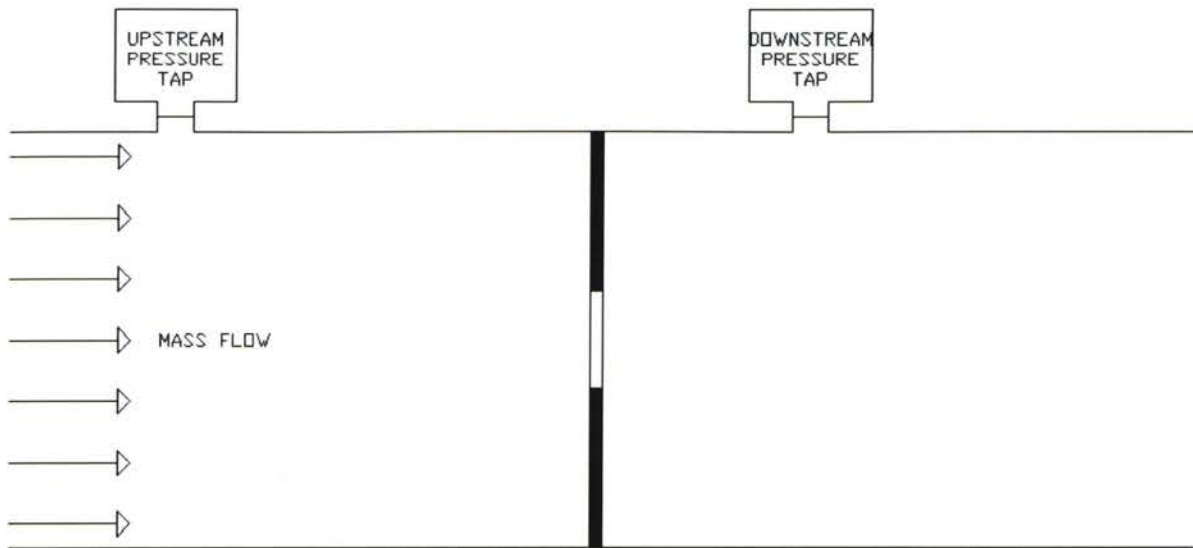


Figure 43: Diagram of an Orifice Plate Flow Meter

White and Perry both give the following equation for compressible flow calculation of an orifice plate (White, 2003)(Perry & Green, 2008).

$$\dot{m} = C_d Y A_t \sqrt{\frac{2 \rho_1 (p_1 - p_2)}{1 - \beta^4}} \quad (3.12)$$

- ❖ \dot{m} Mass Flow [kg/s]
- ❖ C_d Discharge Coefficient
- ❖ Y Expansion Factor for Compressible Gasses
- ❖ ρ_1 Upstream Air Density [kg/m³]
- ❖ p_1 Upstream Static Air Pressure [Pa]

❖ p_2 Downstream Static Air Pressure [Pa]

❖ $\beta = D_t/D$ Diameter Ratio: Throat Diameter divided by Pipe Diameter

The discharge coefficient may be approximated via curve fit presented by White, and is shown below for an orifice with sensors D upstream and $0.5D$ downstream.

$$C_d = 0.5959 + 0.0312\beta^{2.1} + 0.184\beta^8 + 91.71\beta^{2.5} \text{Re}_D^{-0.75} + \left(\frac{0.09\beta^4}{1-\beta^4} \right) 0.4333 - (0.0337\beta^3) 0.47 \quad (3.13)$$

The Reynolds number in the equation above differs from that in the previous section. This is the Reynolds number referenced to the internal pipe diameter approaching the orifice plate.

Perry presents an equation for calculating the expansion factor, and it is shown below.

$$Y = \sqrt{r^{2/k} \left(\frac{k}{k-1} \right) \left(\frac{1-r^{(k-1)/k}}{1-r} \right) \left(\frac{1-\beta^4}{1-\beta^4 r^{2/k}} \right)} \quad (3.14)$$

❖ k Specific Heat Ratio

❖ $r = p_2/p_1$ Pressure Ratio: Downstream Pressure divided by Upstream Pressure

In order to calculate the above equations, some values need to be fixed, and are tabulated below.

Table 36: Physical Parameters for Orifice Plate Flow Meter

Parameter	Quantity	Units
Pipe Internal Diameter D	0.052578	m
Throat Diameter D_t	0.0254	m
Upstream Pressure p_1	1,400e3	Pa
Temperature T	300	K
Air Viscosity μ	184.6e-7	(N · s)/m ²

Mass flow will be defined, and downstream pressure will be calculated iteratively. The steady state results are tabulated below in Table 37.

The orifice meter as a sensor requires three input signals, upstream pressure, downstream pressure, and temperature. Temperature is assumed to be constant, and pressure sensors respond very quickly to changes in flow. Therefore, orifice plate flow meters should respond much faster than the thermal type flow meter, but they are highly subject to calibration errors specifically with respect to the discharge and expansion coefficients.

Another source of error is the accuracy of the pressure sensors. For this model, the pressure sensors are assumed to be perfectly accurate. However in reality, all sensors have inherent errors. Compound these inherent errors with calibration errors, and the orifice plate flow meter will most likely have much more uncertainty over the full flow range than the thermal flow sensor.

Table 37: Orifice Plate Flow Meter Results

Mass Flow (kg/s)	Flow Speed (SFPM)	Reynolds Number	Discharge Coefficient	Expansion Factor	Pressure Ratio	Downstream Pressure (Pa)
0.002	151	2624	0.6432	1.0000	1.0000	1399998
0.005	377	6559	0.6230	1.0000	1.0000	1399992
0.015	1129	19677	0.6115	1.0000	1.0000	1399932
0.020	1506	26236	0.6098	0.9999	0.9999	1399878
0.025	1882	32796	0.6087	0.9999	0.9999	1399809
0.045	3388	59032	0.6065	0.9997	0.9996	1399376
0.135	10170	177096	0.6043	0.9977	0.9959	1394321
0.002	151	2624	0.6432	1.0000	1.0000	1399998
0.005	377	6559	0.6230	1.0000	1.0000	1399992
0.015	1129	19677	0.6115	1.0000	1.0000	1399932
0.020	1506	26236	0.6098	0.9999	0.9999	1399878
0.025	1882	32796	0.6087	0.9999	0.9999	1399809

While the discharge coefficients and expansion coefficients were calculated via iteration during the calculation to solve for the downstream pressure, these values are generally approximated in actual

flow sensors. In general, a single value is selected for the entire range. In this case the discharge coefficient will be set to 0.61. Since the expansion factor only requires the pressure ratio, which is assumed to be measured, it will be calculated for the actual measurement.

Since it was assumed that the dynamic response of the pressure sensors was instantaneous, the plot essentially shows a step change in the orifice plate flow. However, interesting comparisons can be drawn from the dynamic response of the orifice plate flow meter when compared to the thermal flow meter measurements and the actual flow rate as shown below for the same step in Figure 42.

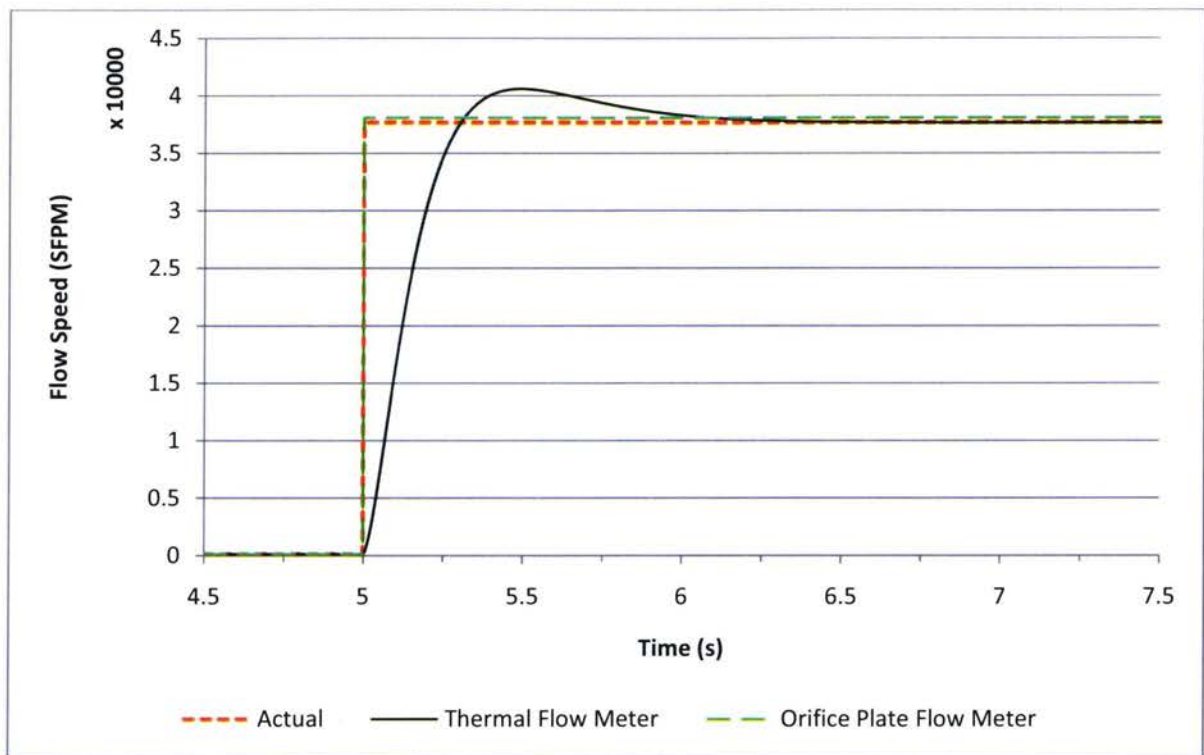


Figure 44: Dynamic Response of Thermal and Orifice Plate Flow Sensors

From this figure, the calibration error of the orifice plate flow meter is clearly observed, and it is approximately $\pm 2\%$ of the actual flow measurement. Even with the assumption of ideal pressure sensors, calibration errors still crop up due to assumptions of a constant discharge coefficient. The thermal flow meter tends towards the actual flow speed, but has a large overshoot and slow response

compared to the orifice plate flow meter. This leads into the primary research of this thesis, which is to improve flow measurement capabilities by fusing data from multiple sensors. Ideally, it would be desirable to have the response of the orifice plate flow meter with the accuracy of the thermal flow sensor.

3.3 Sensor Fusion between Thermal and Orifice Plate Flow Meters

From Figure 44, it appears as though the thermal flow sensor reaches steady state about 1.5s after the initial step input. However, in fusing the signals it is not as easy as just switching between the 'more accurate' signals since the actual flow rate, and therefore the actual error, is unknown. Additionally, in the real world case, there are not only calculation errors with the orifice plate flow meter, but also measurement uncertainties from several sensors. Most methods of sensor fusion are based heavily on these measurement uncertainties.

The hybrid sensor is actually composed of the two flow sensors discussed above. Figure 45 shows that both the thermal flow sensor and the orifice plate flow meter are mounted in the same channel and experience the same mass flow of air. It is expected that the orifice plate flow meter will respond to changes in mass flow faster, but the thermal flow sensor will be more certain at steady state.

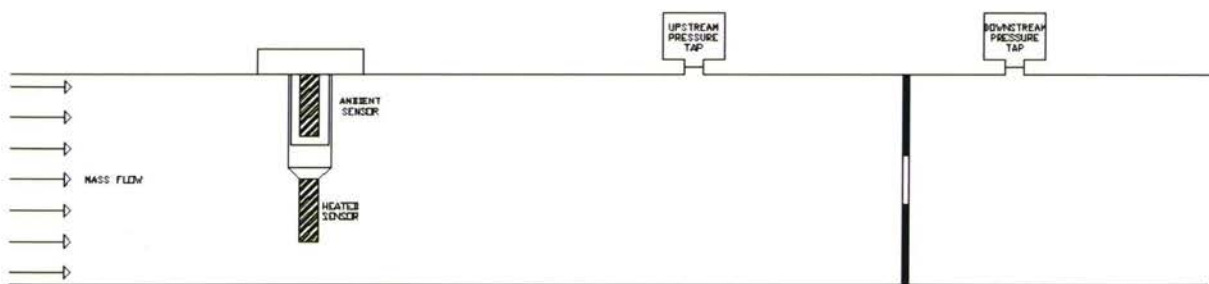


Figure 45: Diagram of Physical Hybrid Sensor

Multi-sensor multi-temporal data fusion is one method outlined by Mitchell. This method uses data from two or more sensors to form a common output based on measurement uncertainties. However, it

relies heavily on predictions from Kalman filters for correction and fusion weights (Mitchell, 2007). A method similar to this was used by Al-Dhaher in conjunction with fuzzy logic. The results were good, but due to the mathematically intensive nature it was expressed in the paper that the method would not be feasible for use on a real-time system (Al-Dhaher, Farsi, & Mackesy, 2005). Kong demonstrates a rather simple method of weighting, which may be applicable to this research. Essentially at each sampling time, the data from eight similar sensors is averaged and the value furthest from the mean is voted out. After which the remaining data is averaged between two groups, and the standard deviation is found. The following equation is then used to find the fused reading for a given sample time (Kong, Chen, Xie, & Zhou, 2005).

$$\hat{T}^+ = \frac{\hat{\sigma}_{(2)}^2}{\hat{\sigma}_{(1)}^2 + \hat{\sigma}_{(2)}^2} \bar{T}_{(1)} + \frac{\hat{\sigma}_{(1)}^2}{\hat{\sigma}_{(1)}^2 + \hat{\sigma}_{(2)}^2} \bar{T}_{(2)} \quad (3.15)$$

Day, from Ryerson, used the difference between the orifice plate calculation and the thermal flow sensor measurement to determine a correction factor (Day, 2005). This does seem to improve the response, but it fails to account for measurement uncertainties, and is heavily biased towards the orifice plate results. This goes against most of the theory, which tends to favor the measurement with the lowest uncertainty, which for the vast majority of the time is the thermal flow sensor. However, during a sudden transient, the uncertainty of the thermal sensor temporarily increases dramatically until steady state is reached.

The method developed below uses assumed steady state uncertainties for the orifice plate and thermal flow sensors. If the mass flow undergoes a relatively large change in a short period of time, the mass flow sensed by the thermal flow sensor will lag behind the actual value. For changes in sensed mass flow larger than the standard deviation, the orifice plate flow meter measurement will be used. For

changes less than the standard deviation, the following equation which has been modified from Equation (3.15) will be used.

$$\hat{w} = \begin{cases} w_o & \text{for } e = |w_T - w_o| > \sigma_T + \sigma_o \\ \frac{\sigma_o^2 + \dot{w}_o^2}{\sigma_o^2 + \dot{w}_o^2 + \sigma_T^2 + \dot{w}_T^2} w_T + \frac{\sigma_T^2 + \dot{w}_T^2}{\sigma_o^2 + \dot{w}_o^2 + \sigma_T^2 + \dot{w}_T^2} w_o & \text{for } e = |w_T - w_o| \leq \sigma_T + \sigma_o \end{cases} \quad (3.16)$$

- ❖ \hat{w} Estimated Mass Flow [SFPM]
- ❖ \dot{w} Average Rate of change of Mass Flow [SFPM/s]
- ❖ σ Measurement Uncertainty
- ❖ w_T Mass Flow measured by Thermal Flow Sensor [SFPM]
- ❖ w_o Mass Flow calculated by Orifice Plate Flow Meter [SFPM]

The steady state measurement uncertainties for the orifice plate and thermal flow sensor for the purposes of this model are assumed to be ± 500 SFPM and ± 50 SFPM respectively. This weighting requires that at steady state the readings from both flow sensors are within the sum of the uncertainty of both sensors.

The difference between mass flows is used to determine whether to force the equation to equal the orifice plate calculation, or the weighted average based on the rate of change. This is used to remove a spikes caused by oscillations of the flow sensor. The spikes are caused when the sensed mass flow rate of change goes to zero, removing the weighting entirely. This method improves the initial response time, and only slightly increases the settling time to the final value. The results for a step from 0.002 kg/s to 0.5 kg/s are shown below in Figure 46.

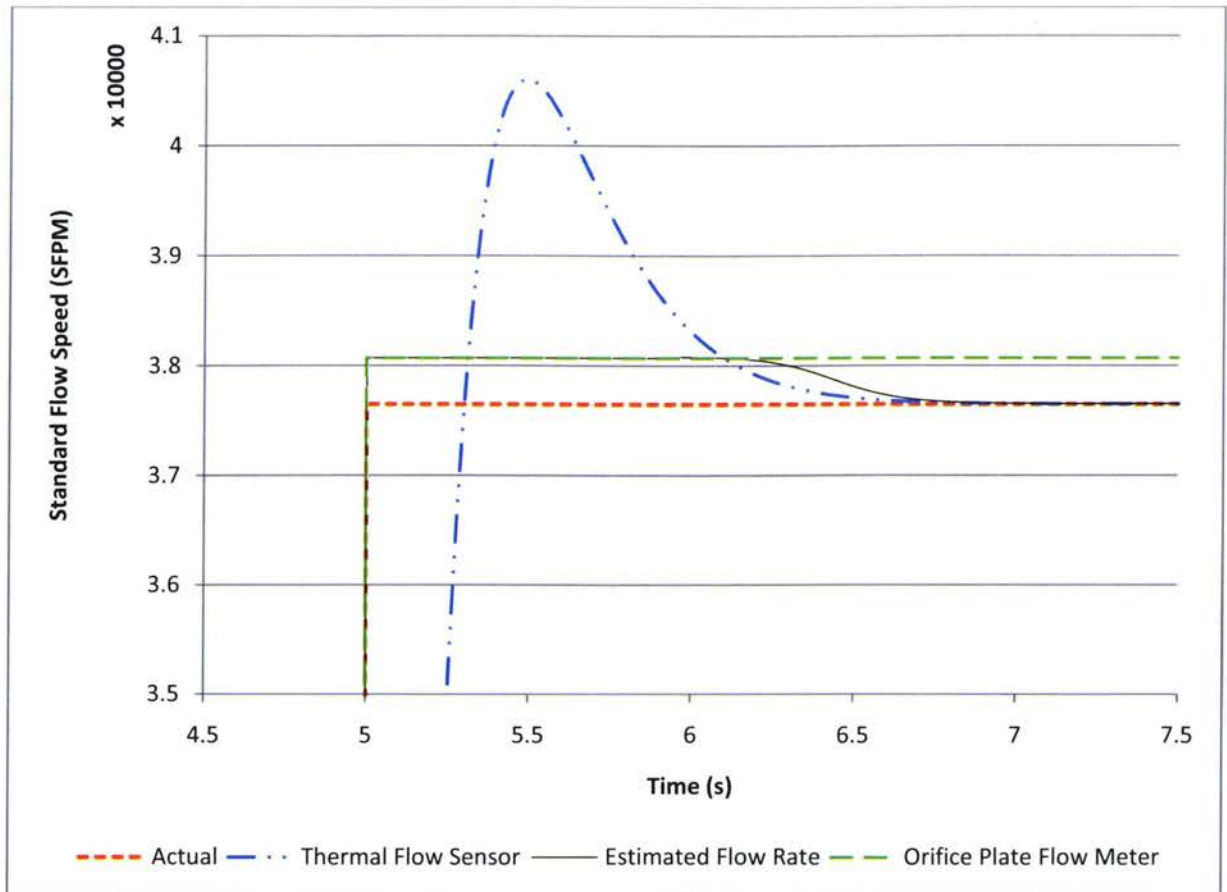


Figure 46: Model Results for Hybrid Sensor, Step from 0.002 kg/s to 0.5 kg/s

These results show that the hybrid sensor output does not exceed the flow rate calculated by the thermal flow sensor. Also, after a rapid initial response from the orifice plate flow meter, it gradually decreases to the measured steady state value of the thermal flow sensor.

However, due to the very large uncertainty with respect to the orifice plate flow calculation a step from 0.5 kg/s to 0.002 kg/s does not give very satisfactory results as shown in Figure 47. The step results in all power being turned off from the heated sensor such that zero flow would be detected by the thermal flow sensor. The hybrid signal matches the erroneous thermal flow sensor due to the large uncertainty of the orifice flow meter measurement and the fact that the rate of change of the thermal flow sensor signal is equal to zero.

Possible remedies involve refining the orifice plate uncertainty to be a variable depending on the calculated flow speed, or placing a minimum flow rate below which the data from the thermal flow sensor will be ignored. Additionally, calibrating the orifice plate using varying discharge coefficients could also reduce the uncertainty at smaller flow rates. These fixes will be considered in the next section which involves pressure loss across a channel, rather than just an orifice.

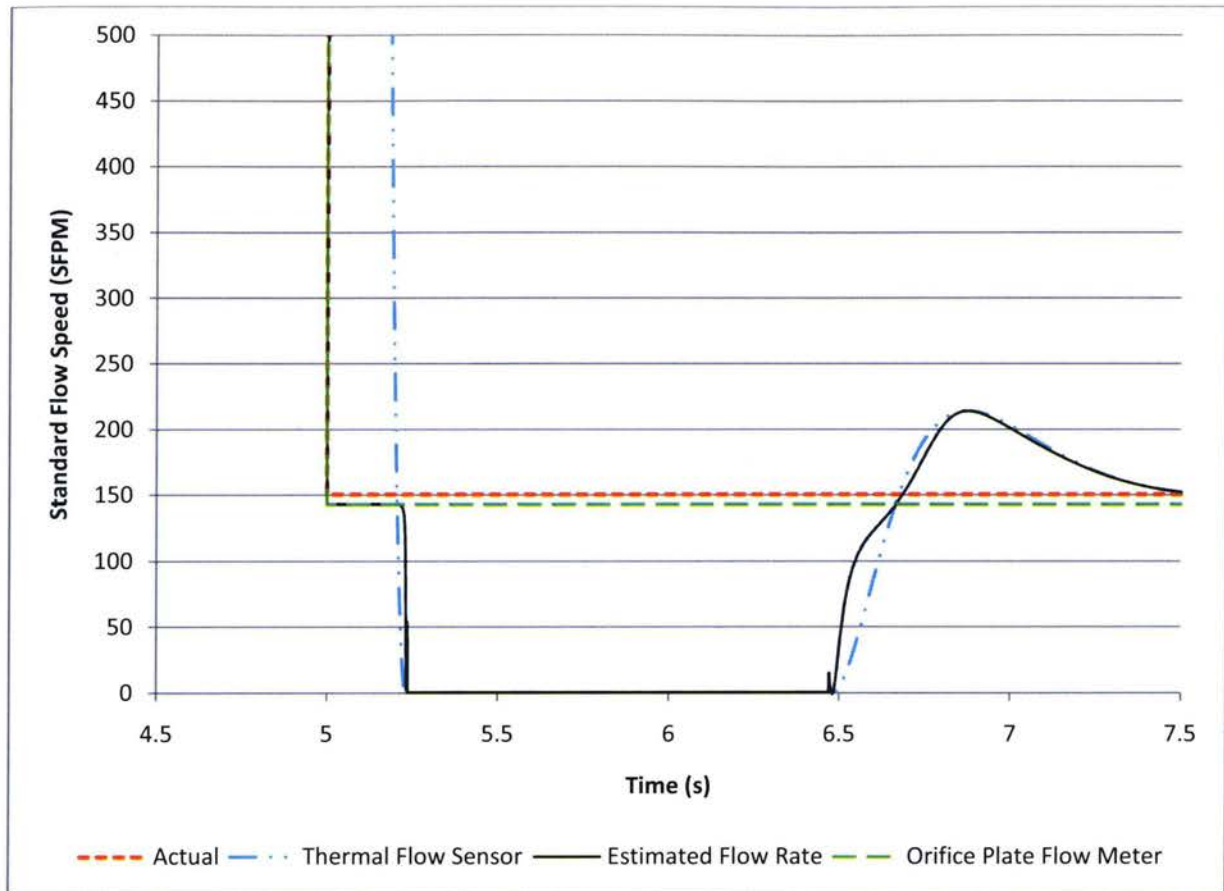


Figure 47: Model Results for Hybrid Sensor, Step from 0.5 kg/s to 0.002 kg/s

3.4 Pressure Drop along a Channel

This section is intended to develop the hybrid sensor theory to utilize the pressure drop along the channel, rather than using the pressure drop across an orifice plate. However, the largest difficulty in

doing this is the pressure coefficient changes as the valves open or close. Therefore, a two part problem develops.

- 1) What affect does changing the valve opening area have upon the mass flow calculation using pressure drop?
- 2) Will the hybrid flow sensor algorithm still hold true for different valve positions?

Most differential head meters, such as orifice plates, have similar problems, specifically poor accuracy and range (Upp & LaNasa, 2002), which was shown in the orifice plate flow meter model. The flow measurement accuracy varies due to the actual change of the discharge coefficient when compared to the constant flow measurement coefficient.

In order to model how the channel pressure drop which will be used as a secondary flow measurement, a simplified pressure drop model must be created that will give a downstream pressure for a given mass flow, upstream pressure, and temperature, similar to the calculation used for the orifice plate. Based on the pressure differential and upstream pressure, a calibration curve will be developed to calculate the loss coefficient, and thus measured mass flow. This will be calibrated to the thermal flow sensor, as it would be on the actual rig. Sensor assumptions from the orifice plate flow meter will be used here, specifically ideal sensors that response instantly and accurately.

From Figure 39, the pressure drop will be measured between P2 and P3 to calculate mass flow measurement. The modeled pressure loss coefficient is shown developed below based on theory from White (White, 2003). Essentially, this may be simplified graphically as a group of flow resistors, similar to electrical or heat transfer theory, and is shown in Figure 48.

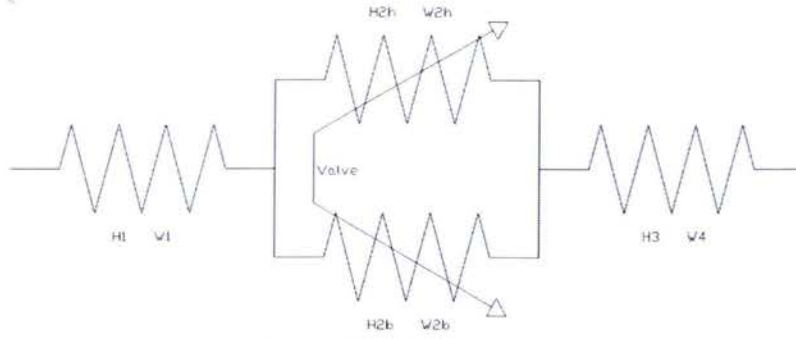


Figure 48: Simplified Flow Resistance Sketch

The T-valve essentially functions as a variable resistor in the flow channels 2_h and 2_b, which denote heat exchanger and bypass channels respectively. The symbol 'H' denotes the head loss in meters, and the symbol 'W' denotes the mass flow rate. The total flow rate and head loss equations are given below.

$$w_T = w_1 = w_{2b} + w_{2h} = w_3 \quad (3.17)$$

$$\Delta h_T = \Delta h_1 + \Delta h_2 + \Delta h_3 \text{ where } \Delta h_2 = \Delta h_{2h} = \Delta h_{2b} \quad (3.18)$$

Head loss is related to the pressure loss coefficient by (3.19). The pressure loss coefficient in (3.20) includes both minor losses and frictional flow losses and is essentially a rewrite of (3.18).

$$\Delta h = \frac{V^2}{2g} \left(\frac{fL}{D} + \sum k \right) = \frac{V^2}{2g} K \quad (3.19)$$

$$K_T = K_1 + K_2 + K_3 \quad (3.20)$$

K_1 and K_2 are essentially frictional flow losses given by (3.21), K_2 is a parallel flow pressure loss calculation that can vary depending on the bypass valve position and given by (3.22).

$$K_1 = \frac{fL_1}{D} + K_{Heater} \quad \text{and} \quad K_3 = \frac{fL_3}{D} \quad (3.21)$$

- ❖ L_1 is the length of Section 1 [m]
- ❖ L_3 is the length of Section 3 [m]
- ❖ K_{Heater} is the minor pressure loss coefficient due the heater
- ❖ f is the friction factor, which for simplicity will be assumed constant
- ❖ D is the pipe internal diameter [m]

$$K_2 = \frac{1}{\frac{1}{\left(K_{VH} + 2K_{90} + K_{HX} + 2K_{45} + \frac{fL_{2H}}{D} \right)} + \frac{1}{\left(K_{VB} + \frac{fL_{2B}}{D} \right)}} \quad (3.22)$$

- ❖ L_{2H} is the length of pipe of the heat exchanger channel [m]
- ❖ L_{2B} is the length of pipe for the bypass channel [m]
- ❖ K_{Heater} is the minor pressure loss due the heater
- ❖ K_{VH} pressure loss coefficient due to the valve diverting flow to the heat exchanger
- ❖ K_{VB} pressure loss coefficient due to the valve diverting flow to the bypass
- ❖ K_{90} pressure loss coefficient due to a 90° elbow
- ❖ K_{45} pressure loss coefficient due to a 45° elbow

As the bypass valve opens, K_{VB} will decrease, and K_{VH} will increase, the values for which were estimated from Figure 6.18b of White. The smaller the valve opening area is, the larger the corresponding pressure drop coefficient. The consideration of two 90° elbows and two 45° elbows is an attempt to account for pressure drop resulting from the change in direction of the T and Y fittings. Table 38 lists the assumed values used for this model, most of the values are from White, the heater coefficient was calculated from data about the heater. The heat exchanger coefficient is a guess.

Table 38: Assumed Coefficients for Channel Model

Friction Factor	0.0024
Section 1 Length	1.2192m
Section 3 Length	1.3716m
Section 2h Length	1.3716m
Section 2b Length	1.2192m
Diameter	0.052578m
Heater Pressure Drop Coefficient	50
90° Elbow Coefficient	0.95
45° Elbow Coefficient	0.30
Heat Exchanger Coefficient	50

To calculate the pressure drop, for a given mass flow the following equation was used. White does note that this is only a first approximation when considering compressible flow. For the actual rig, the pressure drop values will be measured at steady state at several different operating points, but this will be further explained in the experimental section.

$$\Delta P = \frac{1}{2} \rho K_T V_A^2 \quad (3.23)$$

The calculation determines the actual pressure drop. Assuming ideal pressure sensors, this would be equal to the measured pressure drop. To effectively calculate a pressure loss coefficient based on measured data, the mass flow and valve opening positions must be altered so that an average coefficient may be determined. This pressure loss data is shown in Table 39 and Table 40.

Pressure drop coefficients will be calculated based on the measured flow rate from the thermal flow sensor, pressure drop from upstream and downstream sensors, and temperature. Equation (3.23) is rearranged to calculate the measured pressure drop coefficient, K_M .

$$K_M = \frac{\Delta P}{\frac{1}{2} \rho V_M^2} \quad (3.24)$$

Table 39: Pressure Drop with respect to Flow Rate and Opening Angle - 0° to 40°

Actual Mass Flow [kg/s]	Measured Flow Speed [SFPM]	Opening Angle [°]				
		0	10	20	30	40
0	0	0	0	0	0	0
0.002	150	36	36	35	30	25
0.005	376	227	225	217	190	155
0.015	1130	2050	2024	1952	1710	1398
0.020	1506	3644	3598	3471	3040	2485
0.025	1883	5694	5623	5423	4750	3883
0.045	3388	18447	18217	17570	15389	12580
0.135	10166	166024	163954	158128	138502	113224
0.225	16949	461177	455427	439243	384729	314511
0.315	23728	903906	892638	860917	754069	616441
0.410	30878	1531334	1512243	1458504	1277491	1044331
0.500	37648	2277415	2249024	2169102	1899897	1553139
0.720	54210	4722448	4663576	4497850	3939627	3220591

Table 40: Pressure Drop with respect to Flow Rate and Opening Angle - 50° to 90°

Actual Mass Flow [kg/s]	Measured Flow Speed [SFPM]	Opening Angle [°]				
		50	60	70	80	90
0	0	0	0	0	0	0
0.002	150	21	19	18	18	18
0.005	376	132	119	114	113	113
0.015	1130	1187	1073	1027	1013	1018
0.020	1506	2110	1907	1826	1800	1809
0.025	1883	3297	2979	2853	2813	2827
0.045	3388	10681	9653	9242	9113	9159
0.135	10166	96130	86877	83179	82014	82428
0.225	16949	267026	241326	231054	227817	228966
0.315	23728	523372	472999	452865	446521	448773
0.410	30878	886660	801322	767212	756464	760280
0.500	37648	1318649	1191734	1141006	1125021	1130695
0.720	54210	2734351	2471180	2365979	2332844	2344610

The pressure drop coefficient is calculated for each flow rate as measured by the thermal flow sensor at steady state and then averaged for each opening angle and plotted against the bypass opening angle.

Note that 0° means the flow is entirely diverted through the heat exchanger, and at 90° the flow entirely

bypasses the heat exchanger. As can be seen in Figure 49, between 20° and 55° the valve effect is nearly linear. This roughly corresponds with the literature that claims butterfly valves throttle flow best between 15° and 70° (Smith & Zappe, 2004). A curve fit was applied so that the pressure drop coefficient could be easily inferred from the valve angle. For a good fit, the end points were excluded, such that the fit is between 10° and 80°. To compare the change in angle calculation of mass flow to the thermal flow sensor measurement, a constant mass flow rate of 0.5 kg/s was measured for 10s with the angle changing 10°/s over 10s from 0° to 90°. On Figure 50, 0° occurs at 5s, with the angle increasing to 90° at 15s. The flow calculation seems to be most accurate between 6.5s and 12.5s or 15° and 65° bypass valve open area. From a control standpoint, it would be best to operate the bypass valve at a maximum range of 15° to 65° for best effectiveness.

For the bypass valve operating range of 15° to 65°, the error magnitude tends to scale with the actual mass flow rate. The percentage error was in the range of $\pm 0.3\%$ of the signal. The key being is that using this method of flow calculation, the error is constant and repeatable, which should aid in the further development of the hybrid sensor.

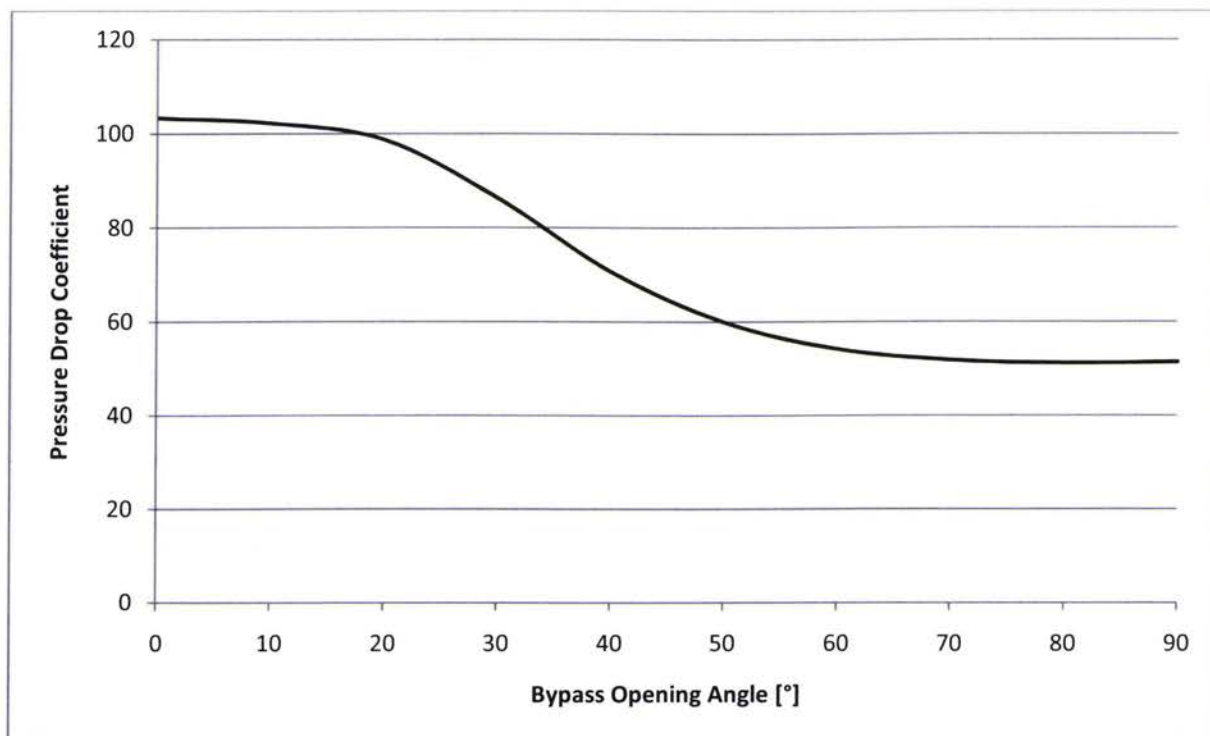


Figure 49: Change in Pressure Drop Coefficient due to Bypass Valve Position

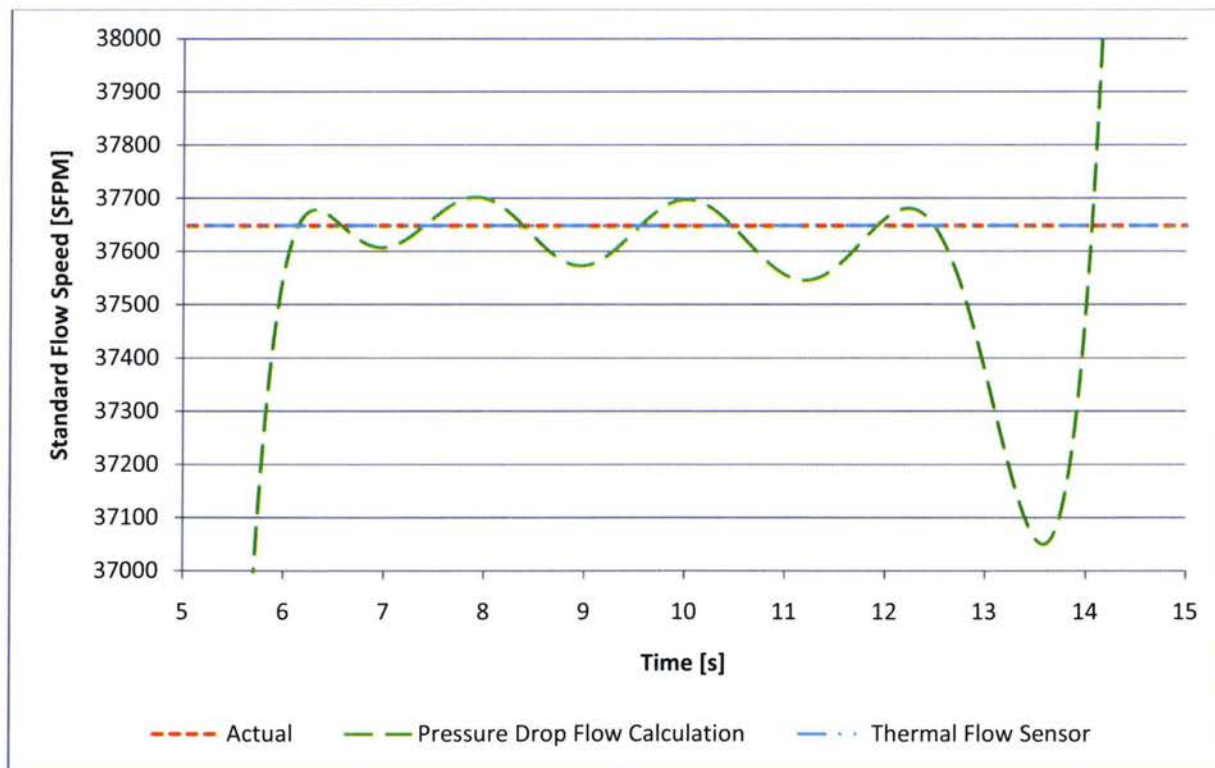


Figure 50: Effects of Bypass Valve Position on Flow Calculation

Using a bypass angle of 30° , the flow was stepped 0.002 kg/s to 0.5 kg/s in Figure 51 by using the algorithm from the previous section. However, the error range has been corrected to what is seen by the newly developed flow calculation model. Additionally, the uncertainty of the thermal flow sensor is assumed to be around ± 2 SFPM. Of course, these are all theoretical signals and measurements, experimental signals are expected to have much higher uncertainty and noise. However, as expected with more thoroughly expressed uncertainties, a lot of the problems seen using a simple orifice plate have worked themselves out. Most of the previous problems had to do with inconsistent or variable errors that did not follow a set pattern.

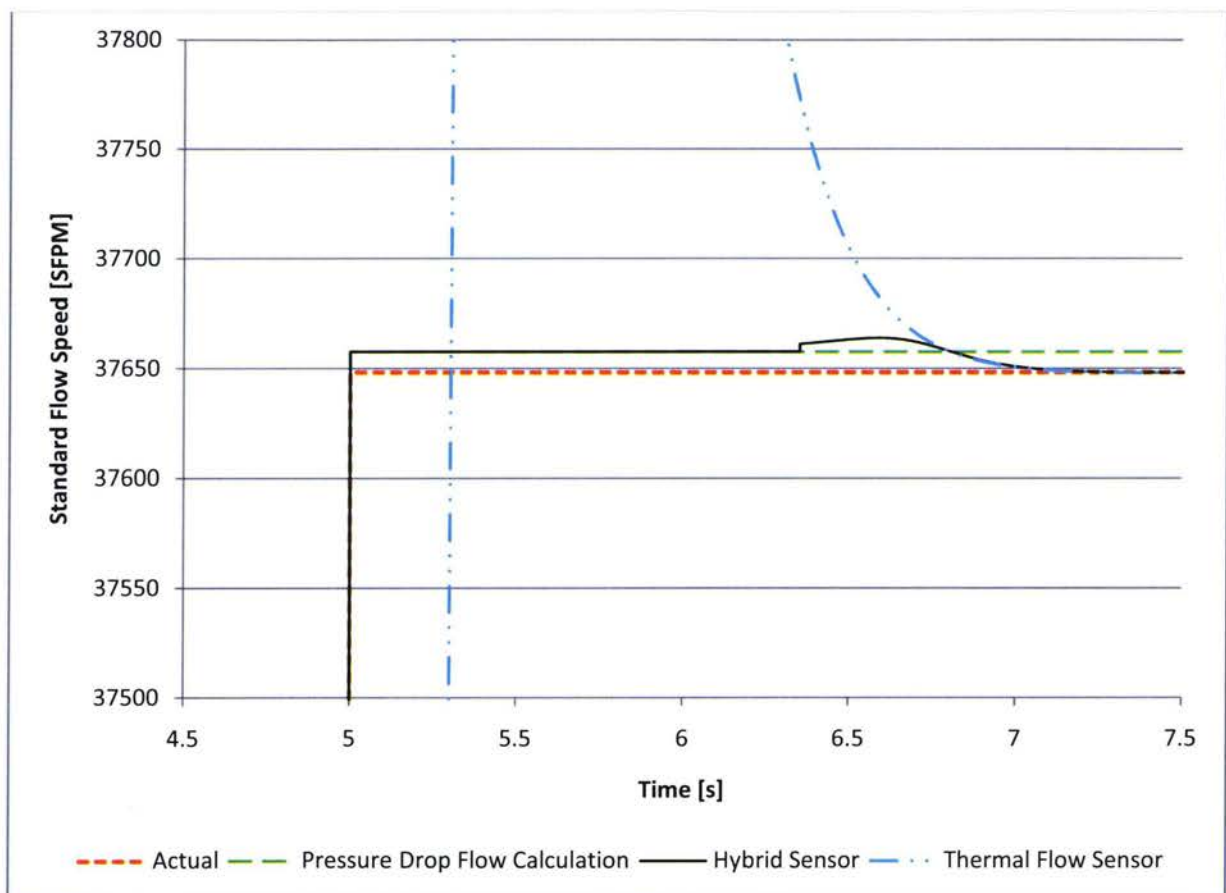


Figure 51: Hybrid Sensor 0.002 kg/s to 0.5 kg/s

The empirical method used to calculate the pressure drop coefficient seems to allow for a more accurate, or at least more predictable, uncertainty for the pressure drop calculation. This allows for the reverse step, from 0.5 kg/s to 0.002 kg/s, to be feasible as shown in Figure 52.

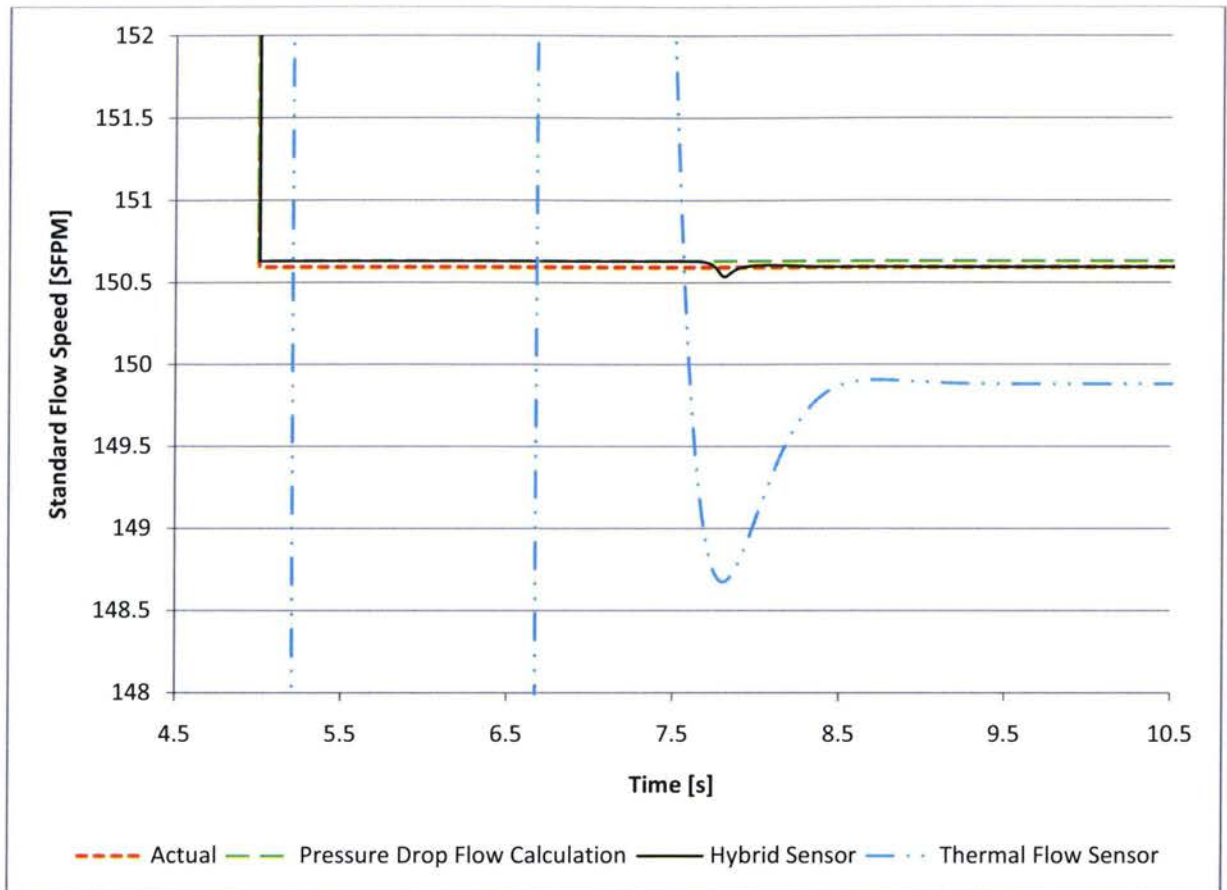


Figure 52: Hybrid Sensor 0.5 kg/s to 0.002 kg/s

In the above plot, the step occurs at 5s, and the thermal flow sensor reduces power dramatically such that it effectively detects zero flow. Around 6.75s the heater on the thermal flow sensor turns back on, resulting in an overshoot and oscillation before damping out by 9.5s. The hybrid sensor effectively eliminates the large overshoots of the thermal flow sensor, but in this case the hybrid settles close to the pressure drop calculation due to the relative high degree of accuracy at low flow speeds. However,

this might create an issue in the experimental case due to the extremely small pressure drop and sensor noise.

The other concern is the effect of the valve moving on the hybrid sensor, and whether it will affect a steady state reading. From the figure below, it can be seen that the hybrid sensor works between 6 and 12.5s, corresponding to 10° and 65° , it fails outside of these limits due to the curve fit used, though for proper throttling, the valve should be operating in this range anyways. Essentially, at steady state mass flow, changes in the bypass angle, provided it is within the operating range, will not affect the calculated hybrid sensor output.

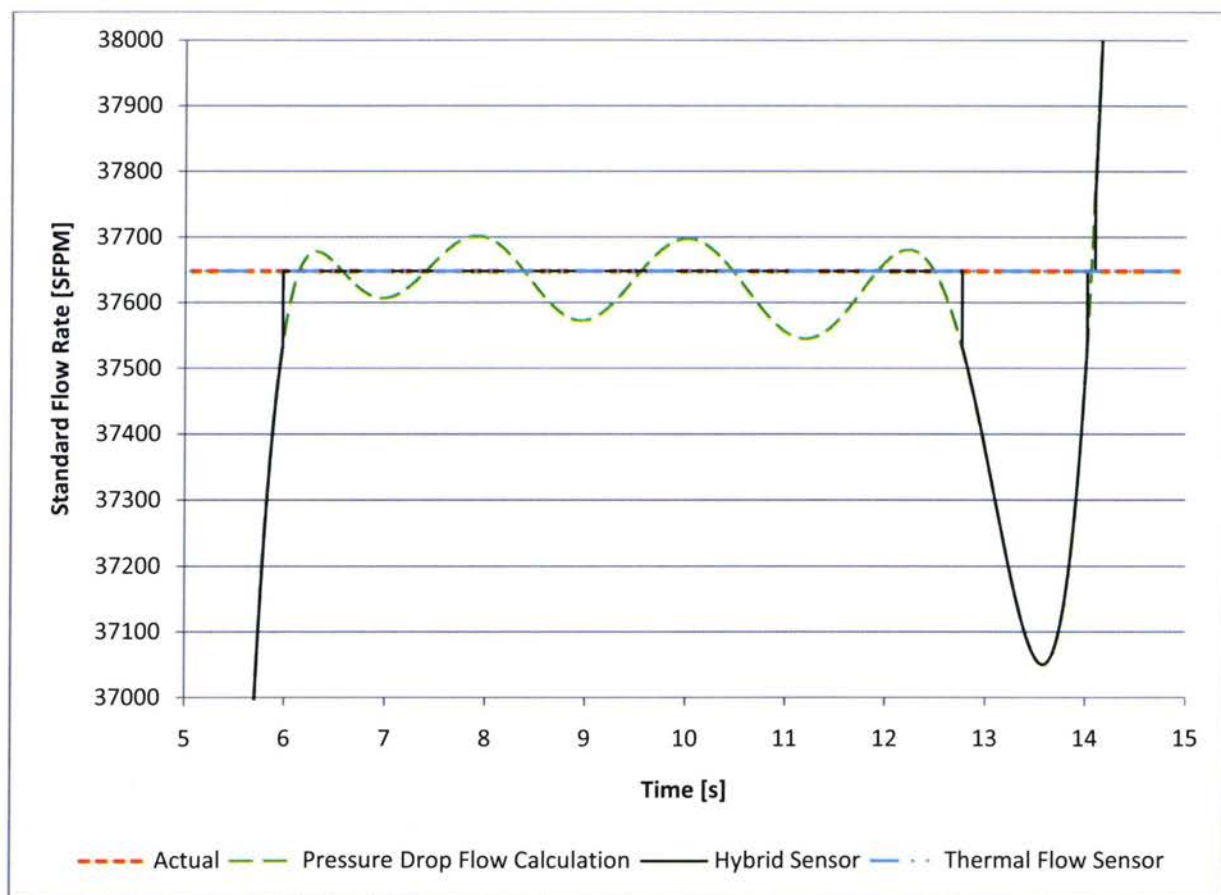


Figure 53: Effects of Bypass Valve Position on Hybrid Sensor

In conclusion, the theory for the hybrid sensor is reasonable. Foreseeable difficulties in proving this theory via experiment include the following:

- ❖ Getting a strong step change in mass flow
- ❖ Accurate pressure drop measurements
- ❖ Accurate flow sensor calibration
- ❖ High signal noise

The next chapter outlines the experiments used to validate the theory of this chapter.

4 Experimental Work

The experimental work of this thesis was limited due to construction delays and setup. However, enough was performed to validate the hybrid flow sensor algorithm. The bottom bleed air and outflow channels were used for experiments. Pressure in the load tank was controlled using the bottom bleed valve, and flow out of the tank was controlled using the outflow valve.

Setup for the experiments involved closing off the exits of the right hand tank, while leaving the cross-flow valve open for a larger volume of supply air. For the left hand tank, the inlet and bottom bleed channel manual valves are fully opened with the actuators supplying all control.

Sensors are located in the bottom bleed channel at the positions shown in Figure 54 . However, before the hybrid flow sensor testing could be accomplished, the pressure drop across the rig needed to be measured to determine if it could be used to calculate flow rate. This process was attempted in the flow calculation section.

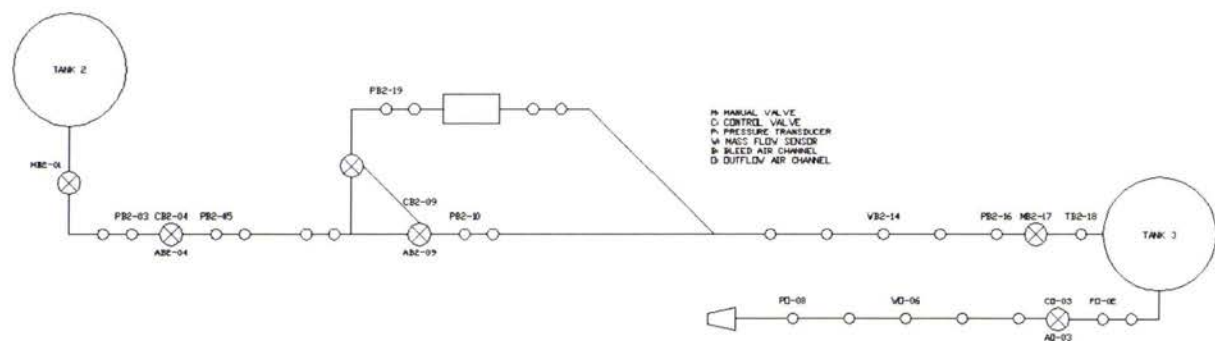


Figure 54: Sensor Configuration for Experiments

After a method of calculating the flow rate was found, it was calibrated to the Omega flow sensor. The response between the thermal flow sensor and the flow calculation should be checked to see if there is a noticeable difference in response. If the response difference is significant, then the hybrid flow algorithm may be applied and tested.

4.1 Flow Rate Calculation

For the flow rate calculation, data was taken from all sensors at several different flow rates and Tank 3 pressures to determine if the pressure drop can be measured across a channel of the rig. Flow rates were varied between 1000 SFPM up to 3000 SFPM for brief periods, but no appreciable pressure drop could be measured between sensors PB2-05 and PO-02 which forms the pressure drop value similar to that used in the theoretical section for the flow calculation. A fifteen second sample of the test is shown in Figure 55. The flow rate during this time was approximately 1500 SFPM with a Tank 2 pressure of 50 psig and the flow fully diverted through the heat exchanger.

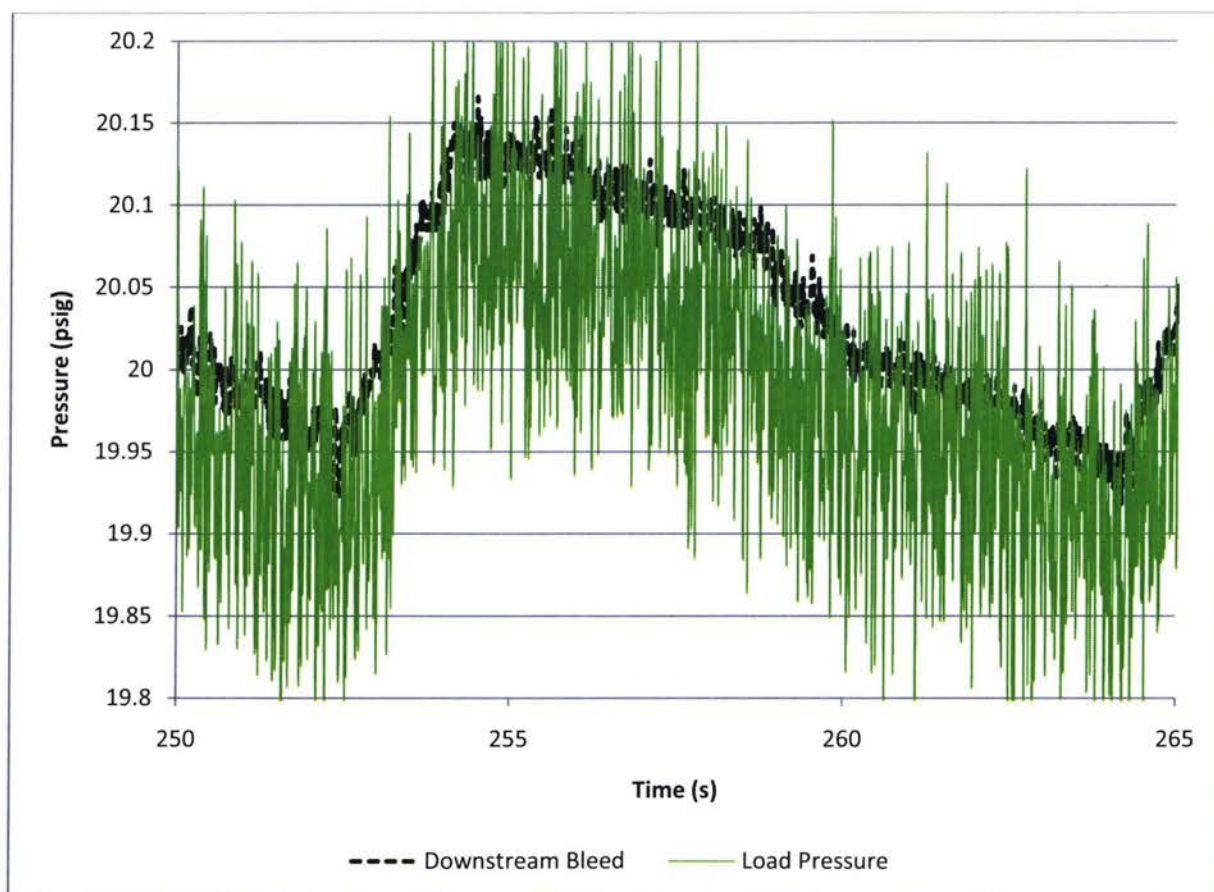


Figure 55: Pressure Drop across the Bottom Bleed Channel

It is difficult to distinguish between the two signals, but the downstream bleed, measured just after the bleed channel valve at PB2-05, seems to be slightly higher on average than the PO-02 or the load pressure measurement on average. However, the difference between both signals is clearly within the operating error of the sensors. The difference between these two sensors is much too small to be used for a flow approximation.

Referring back to Table 39, for a bypass opening angle of 0° with a flow speed of roughly 1500 SFPM, the pressure drop was calculated to be 3644 Pa, or 0.5285 psi, including the heater. The heat exchanger does not seem to be a very significant contributor of pressure drop as was assumed in the theoretical calculation. It is understandable that the pressure drop is difficult to measure when considering the uncertainty of the sensors, absent heater, and low pressure drop from the heat exchanger. It may be possible to achieve a measureable pressure drop with the heater installed and a very large flow rate, in the range of 3500 to 4200 SFPM. This range is roughly 80 to 100 SCFM, which is the upper operating limit of the heater.

However, noticeable pressure drops do occur across the control valves located at B2-04 and O-03. This is an obvious and relatively straight forward means of obtaining a pressure drop for a flow calculation. A similar process may be used as discussed in Section 3.4. Essentially, the upstream and downstream static pressures will be measured, along with flow and valve opening angle. A pressure drop coefficient will be determined from this information and related to the opening angle. This will be performed on both the bleed channel control valve and the outflow valve, so that the hybrid sensor algorithm might be compared to two different flow sensors.

After several days of testing, no repeatable pressure drop coefficient related to the opening angle of the valve could be found. Any values that were found seemed to be accurate for only a very small range, and even then only on certain occasions. Most likely this is due to the very small opening angles at

which the rig operates. The rubber valve seal interacts with the edge of the valve disc in a random manner at small opening angles.

An easily reproducible pressure drop coefficient was found across the exhaust restriction. It was setup with a PX219 sensor and calibrated to the FMA905 flow sensor. Since it is so close to the exhaust, the density was assumed constant at 1.2041 kg/m^3 which is the standard density at 20°C and standard pressure of 101325 Pa . The pressure drop coefficient was calculated at approximately 2646 ± 100 .

Figure 56 is an image of the SIMULINK code used to calculate the pressure drop coefficient.

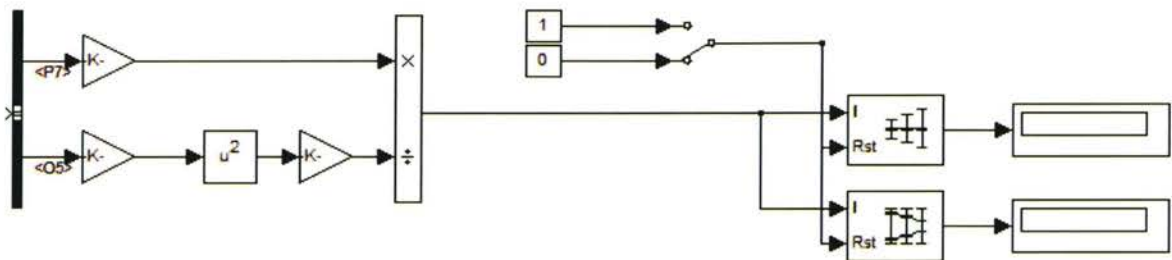


Figure 56: SIMULINK Pressure Drop Calculation

The pressure and flow data, P7 and O5 respectively, were converted to metric units in real-time. The pressure drop coefficient was then calculated and averaged over a steady state flow rate of 1000 SFPM. P7 refers to the pressure sensor located at PO-08, which is just upstream the final exhaust restriction. Since it is a gauge pressure sensor, it effectively measures the pressure difference between the outlet and inlet of the flow restriction.

Using the pressure drop coefficient that was calculated in the steps above, the flow rate was estimated in real time and compared to the flow rate measured by the Omega flow sensor. Another test was performed to determine the response of the restriction flow estimation. For this test, the load tank pressure was maintained at 20 psig. The outflow valve was manually commanded for the test, with the

valve being commanded open and closed to achieve as fast of a response as possible. The valve command and actual valve response are shown in Figure 57.

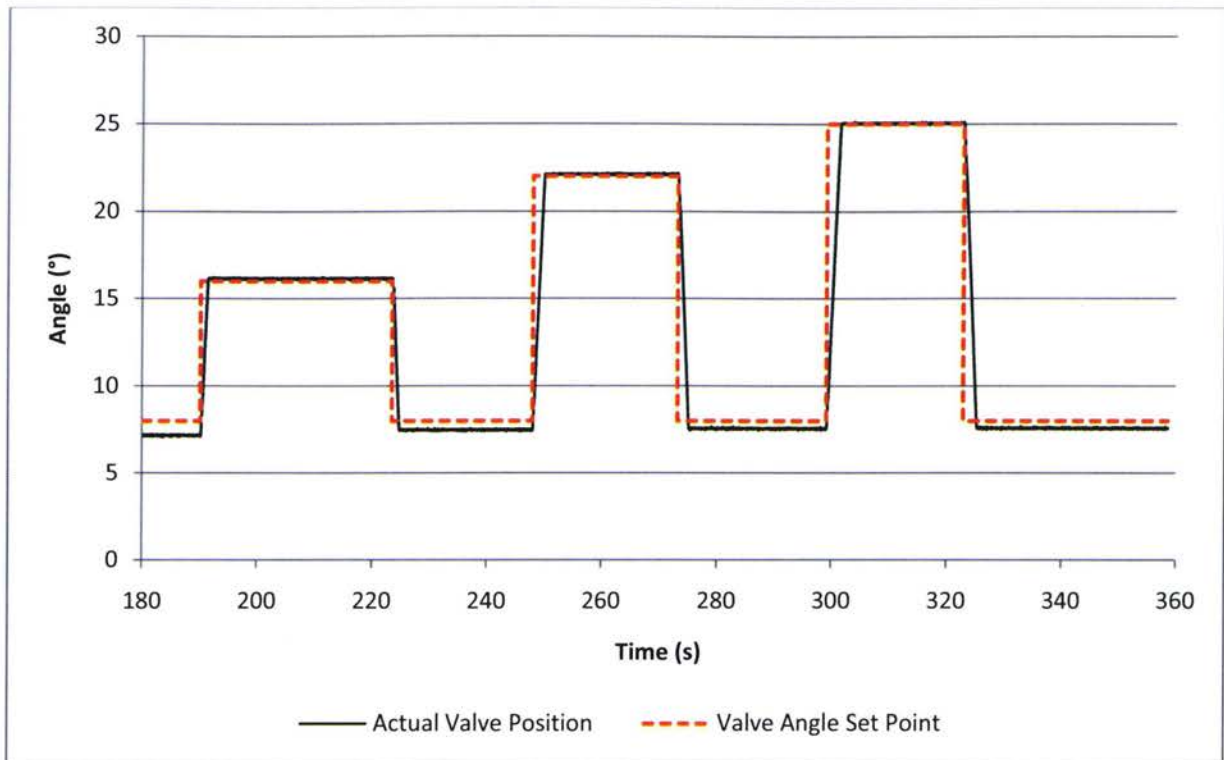


Figure 57: Command and Actual Valve Positions for Omega Flow Sensor Response Test

At small opening angles, less than 10° , there is a slight offset error, but above 15° the commanded angle and the actual angle are very close to being equal. This resulting step pattern affected flow rates as shown in Figure 58. Here the necessity of the hybrid flow sensor is not apparent. Flow response is almost instantaneous from the Omega flow sensors, and from Figure 59 it can be seen that the flow sensor signal lags roughly 0.5s behind the pressure calculation. This is very close to the 400ms quoted by the manufacturer for the Omega flow sensor response time.

Other observations gleaned from the step response plot are the large overshoot of the fast responding flow sensor, and the offset error of the restriction flow calculation. Both of these errors were predicted in the theoretical section. However, the flow signal is not as steady as expected. The fluctuating flow

signal and quick response does not lend the Omega sensor to the hybrid algorithm. Therefore, the Omega sensor was switched with the thermal flow sensor, for which the theoretical work was based. Essentially, the experiment is following the same process as Section 3.3, but with a simplified head loss flow calculation.

Another interesting observation may be gleaned by comparing Figure 57 to Figure 58. Even though the valve returns to the same position of roughly 8° each time, the flow never returns to the same rate. This is the reason that the correlation between the valve opening angle and pressure drop coefficient across the valve was unreliable.

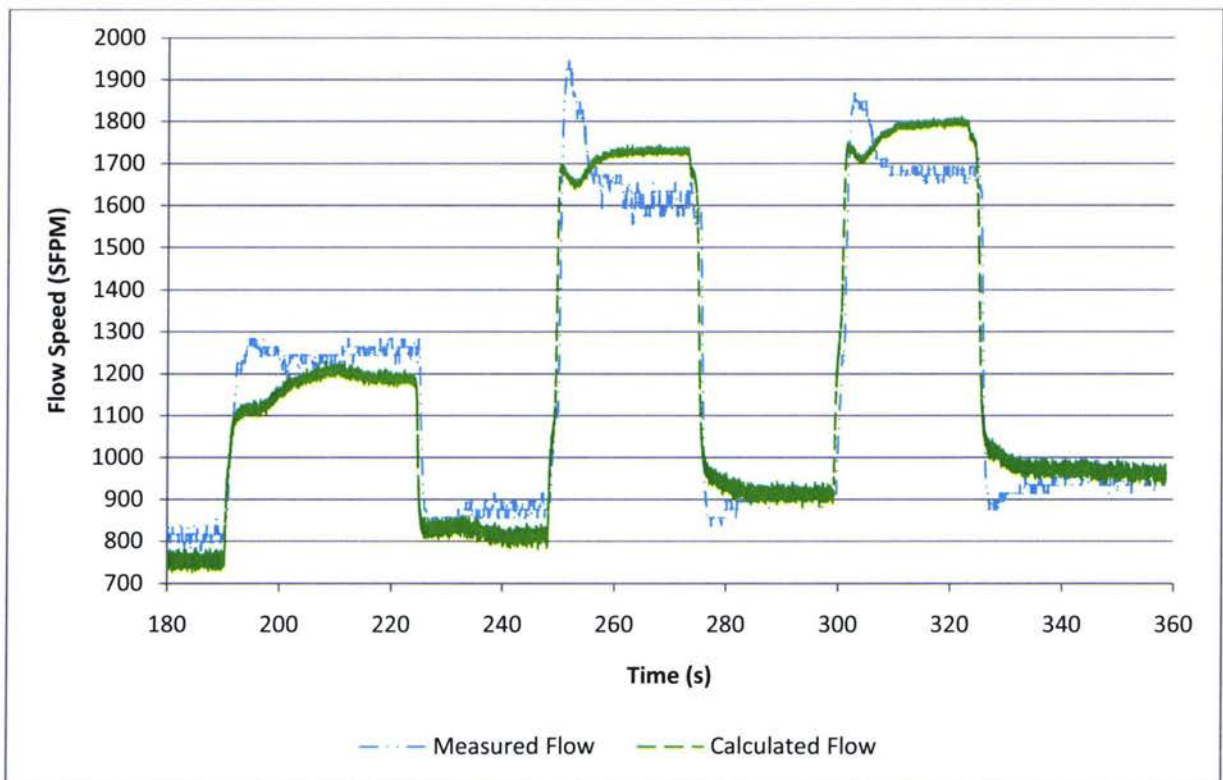


Figure 58: Omega Flow Response Test Results

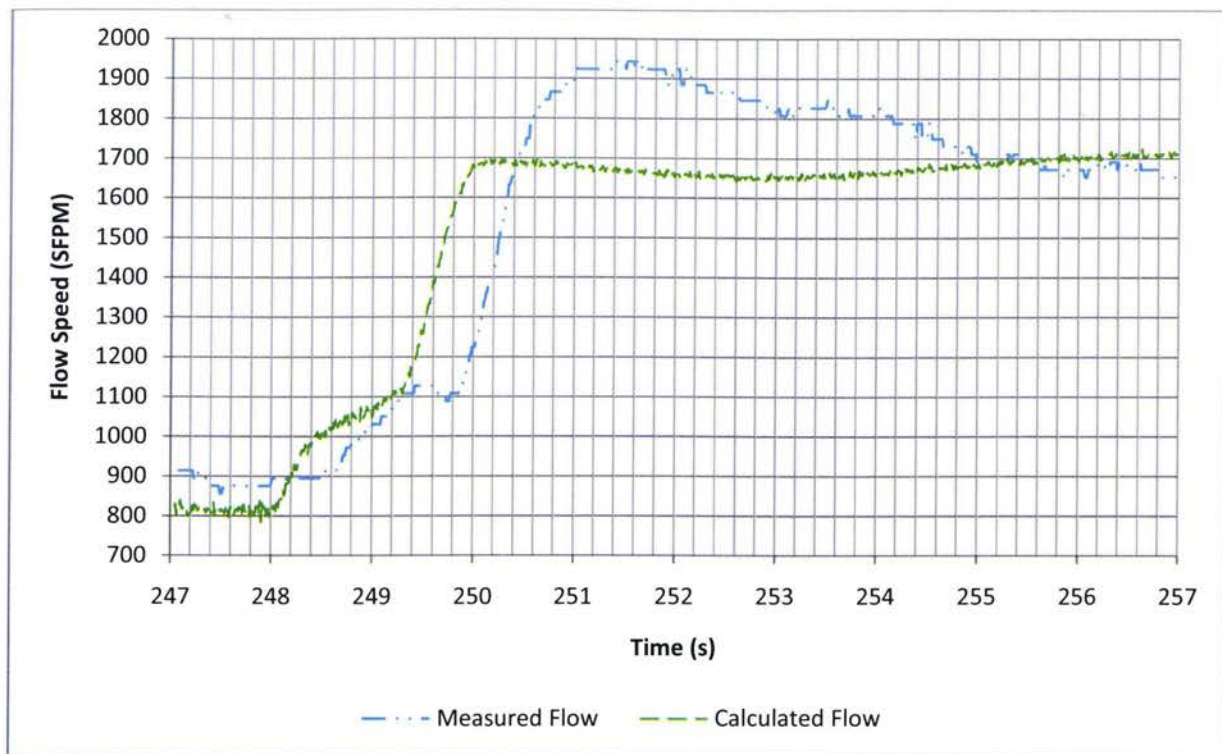


Figure 59: Omega Flow Sensor Step Response

After the flow sensors were switched, another control system test was performed to ensure proper response. Pressure was again maintained at 20 psig while the flow was stepped from 1000 SFPM to 1500 SFPM and then back down to 1000 SFPM. The results are shown in Figure 60, and the differences between the two thermal flow sensors are immediately apparent. The Omega flow sensor response is rapid, but the signal fluctuates heavily at steady state. Conversely, the thermal flow sensor has a very slow response, but seems to be very smooth.

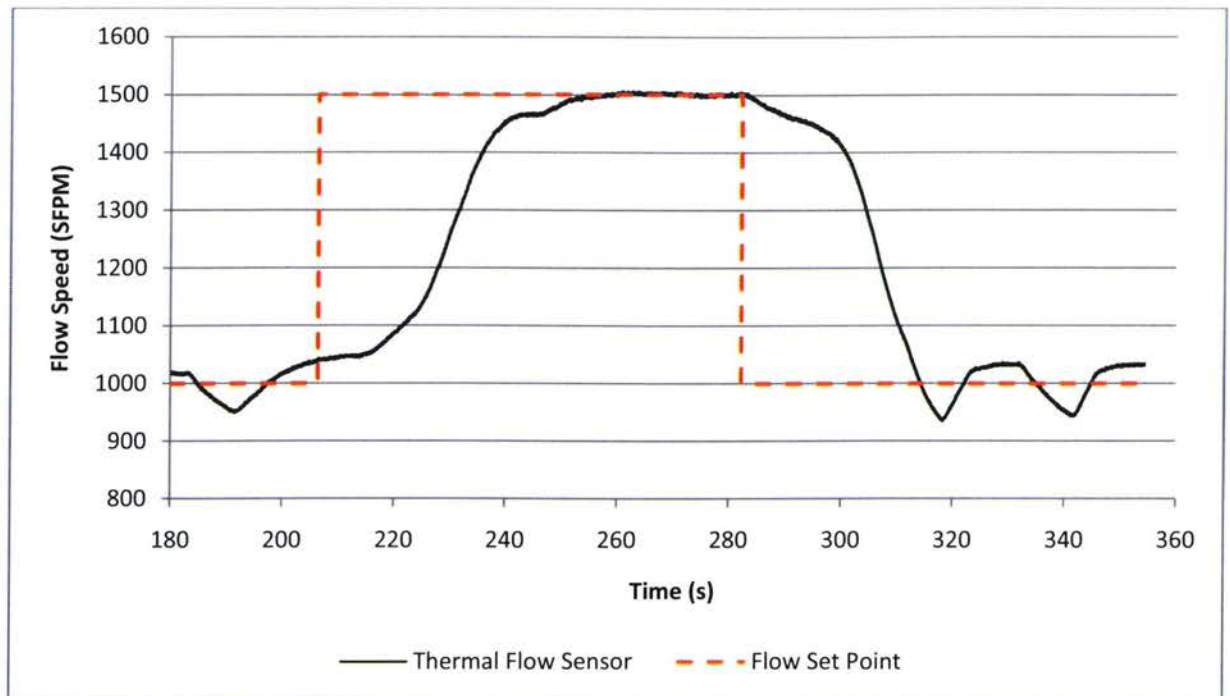


Figure 60: Varying Flow with Constant Pressure, Thermal Flow Sensor Plot

Another flow sensor response test was performed to determine the actual response of the thermal flow sensor. No change was made to the restriction flow calculation, since it was set up using the same flow meter as the thermal flow sensor. Again, the valve was manually commanded opened and closed for fast response. The commanded and actual valve positions are shown in Figure 61, and the flow sensor response compared to flow calculation is shown in Figure 62. As before, the variability of flow rate at the same valve position is apparent. Additionally, the smooth response of the thermal flow sensor shows the offset error of the flow calculation at larger flow rates. However, the most noticeable difference between the thermal flow sensor and the Omega responses are the settling times. Settling time for the Omega sensor is roughly 5s, but for the thermal sensor is closer to 20s. Additionally, the slow response time of the thermal sensor is much more apparent, and the sensor takes roughly 1.5s to even begin showing significant changes in flow rate.

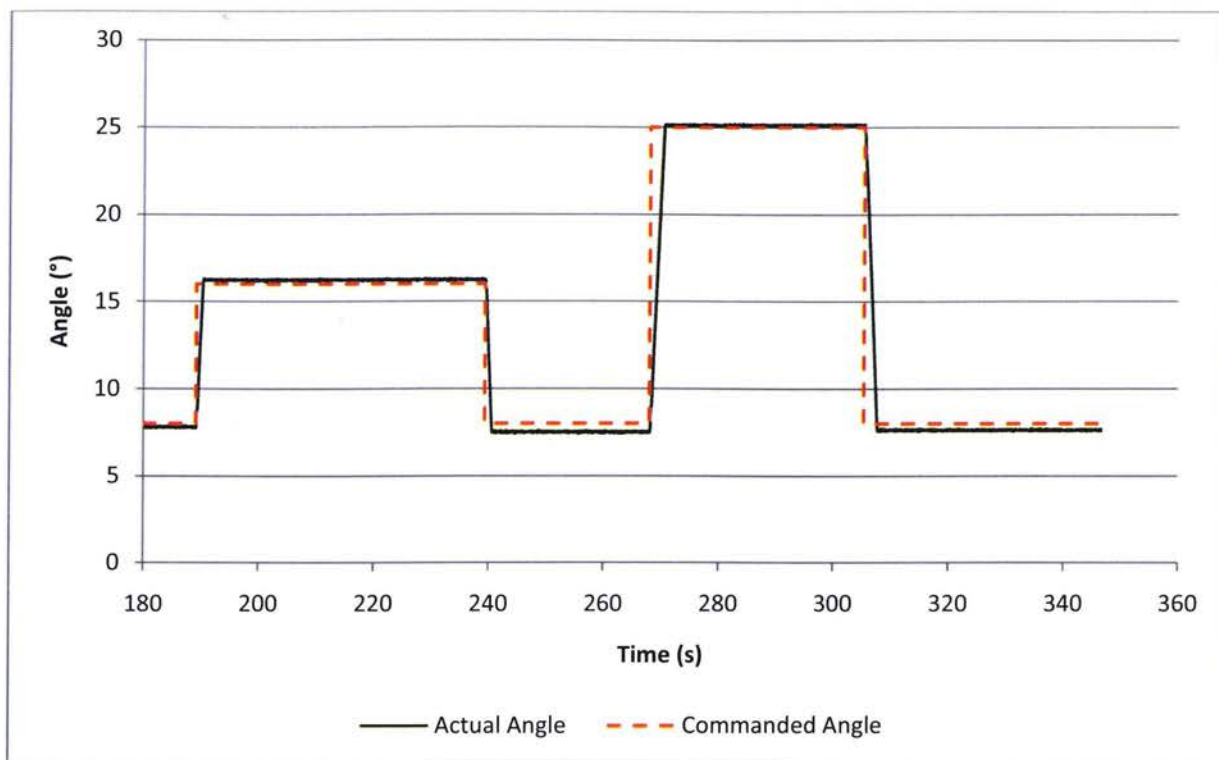


Figure 61: Command and Actual Valve Positions for Thermal Flow Sensor Response Test

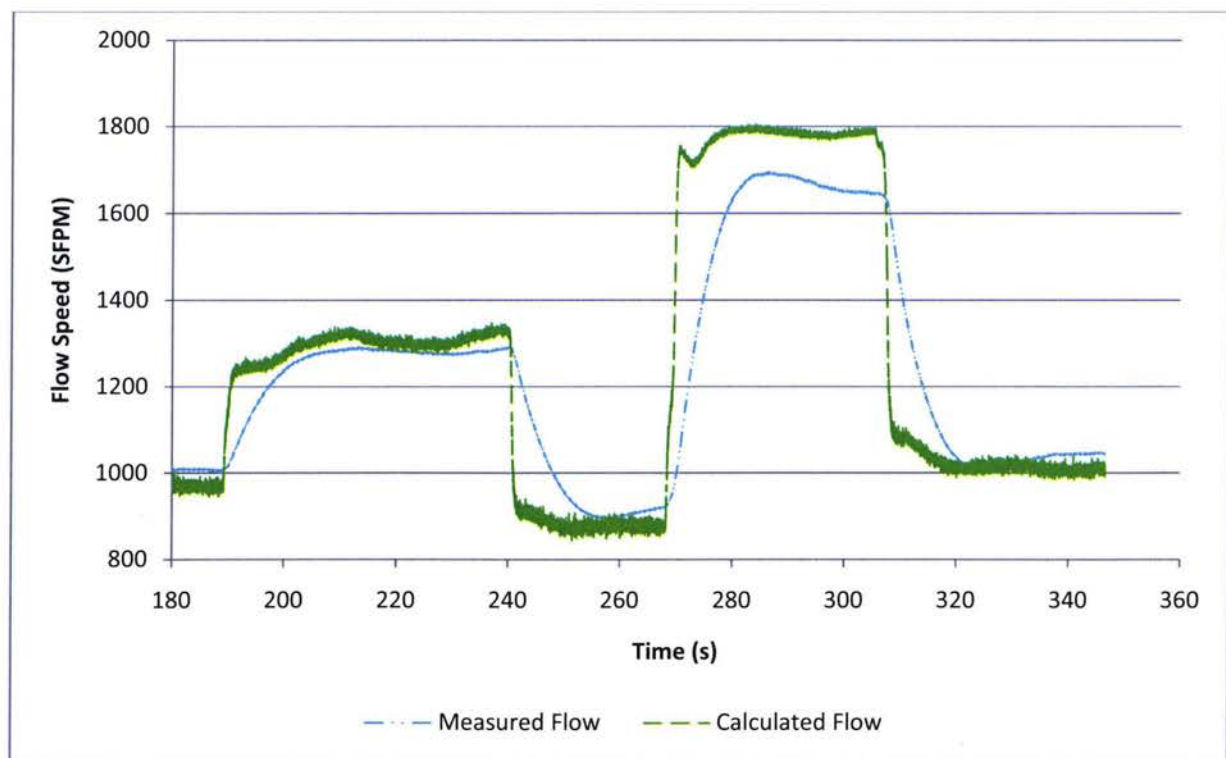


Figure 62: Thermal Flow Response Test Results

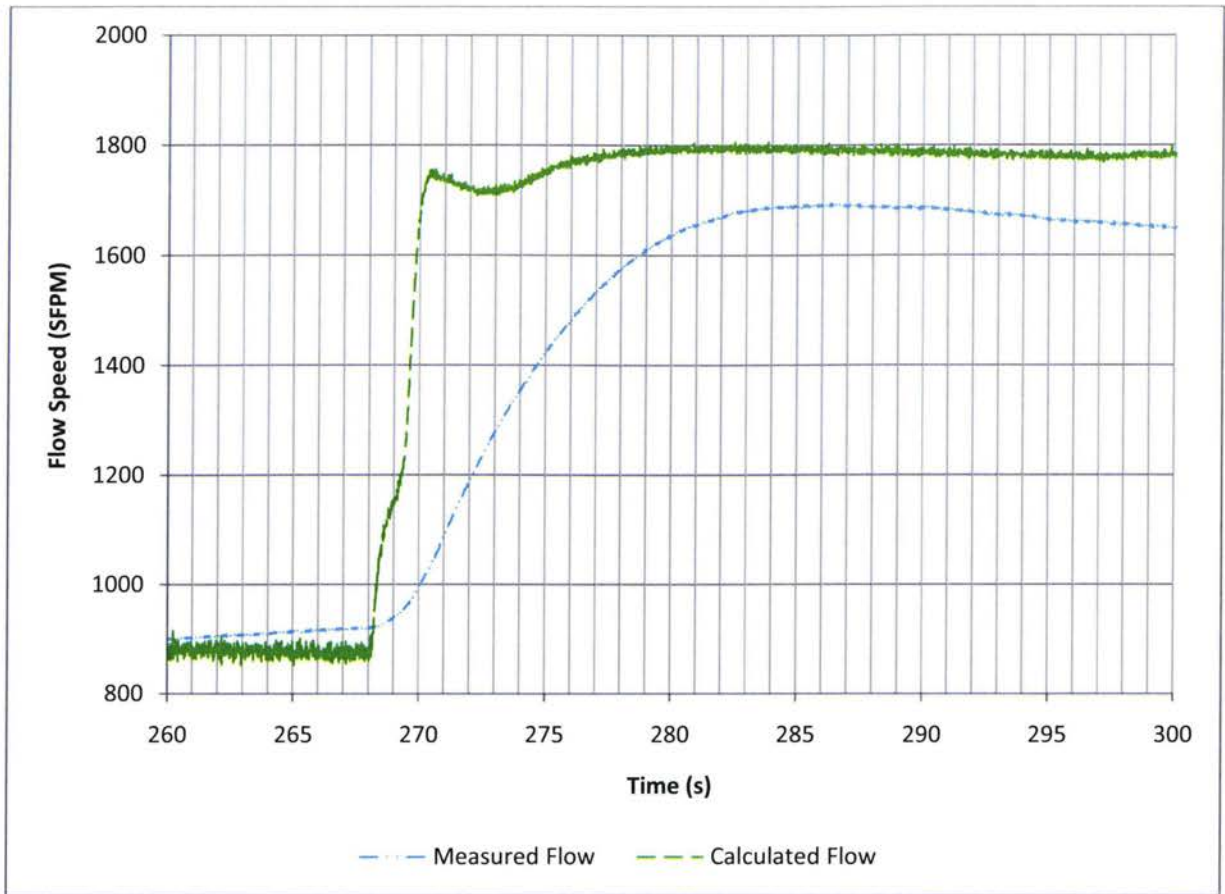


Figure 63: Thermal Flow Sensor Step Response

Therefore, the thermal flow sensor could greatly benefit from the hybrid algorithm. This algorithm is intended to use the redundant sensors to get the fast response of the head loss flow calculation but retain the accurate steady state performance of the thermal flow sensor.

4.2 Hybrid Sensor Algorithm Validation

The hybrid algorithm developed in Section 3.3, was further simplified to only include the weighting function. Furthermore, heavy filtering and down sampling was required to allow the discrete derivative of the signal to be found. Thus Equation (3.16) is simplified to Equation (4.1) since it was found that the hybrid would still operate satisfactorily without the switch at high mass flow differences.

$$\hat{w} = \frac{\sigma_C^2 + \dot{w}_C^2}{\sigma_C^2 + \dot{w}_C^2 + \sigma_M^2 + \dot{w}_M^2} w_M + \frac{\sigma_M^2 + \dot{w}_M^2}{\sigma_C^2 + \dot{w}_C^2 + \sigma_M^2 + \dot{w}_M^2} w_C \quad (4.1)$$

The SIMULINK code is shown in Figure 64. Since the uncertainties are constants, they are simply squared and serve for the steady state weighting. Following the actual sensor signals, pressure or thermal, the signals are first down sampled to 100 samples per second. Next, both signals are individually averaged over ten consecutive samples, or 0.1s. The sample rate is then increased back up to 1000 samples per second. The discrete derivative is then taken with a gain of 0.0001 and 4 applied to the pressure and thermal discrete derivative blocks respectively. At this point, the four weightings and flow signals are used in Equation (4.1). The output is again down sampled, averaged, and then up sampled to create a smoother curve.

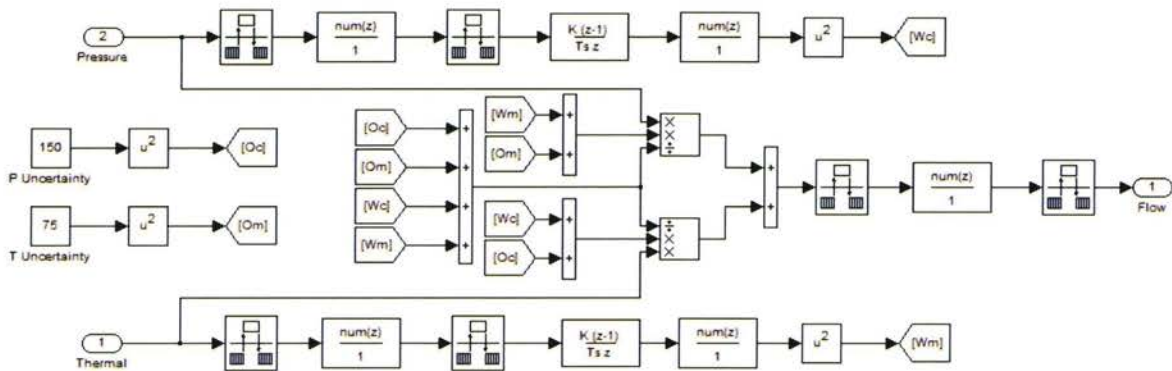


Figure 64: SIMULINK Hybrid Sensor Subsystem

The results of this equation are shown in Figure 65, which undergoes a similar response test as the Omega and thermal flow meters.

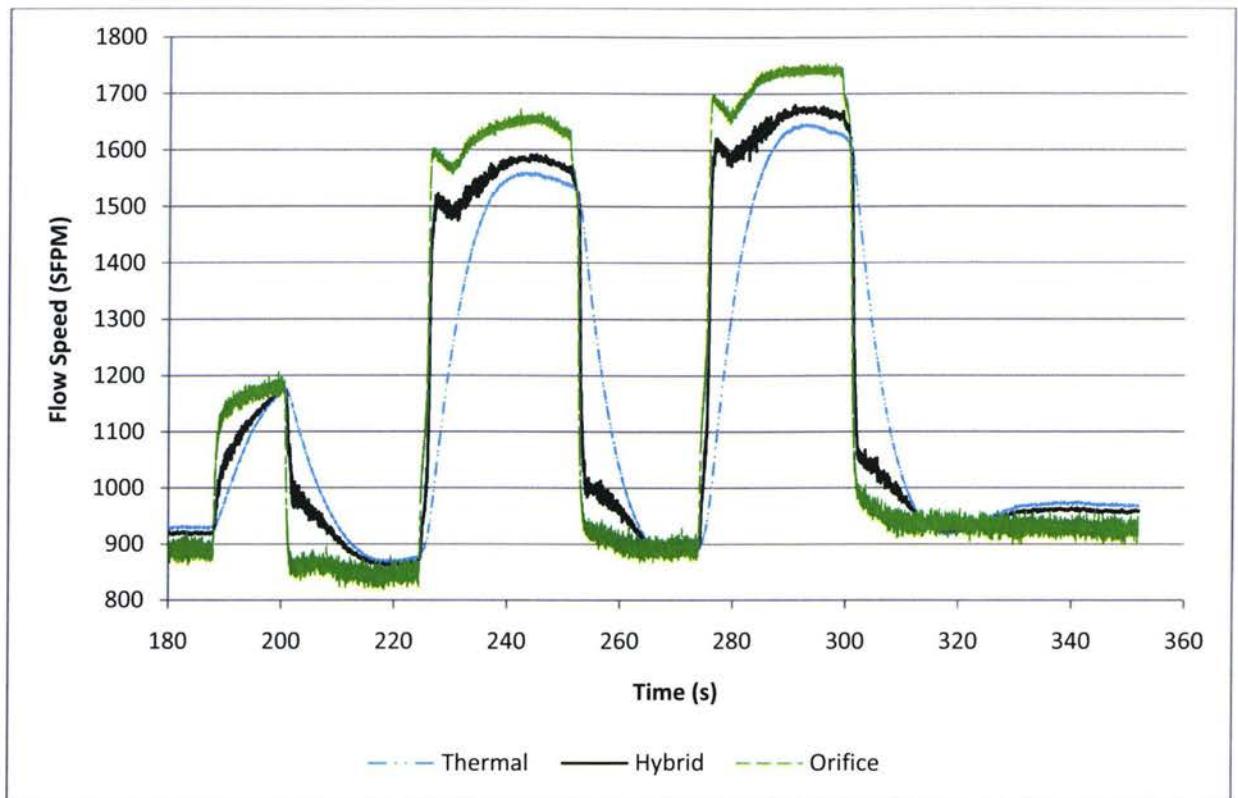


Figure 65: Hybrid Algorithm Flow Response Test

For each of the steps, the head loss calculation response typically gives the fastest response and noisiest signal. The hybrid algorithm is always between the head loss calculation and flow measurement. Finally the flow measurement is the smoothest and slowest responding signal of the three. For each of the three increasing steps, there is a noticeable dip followed by a gradual rise of the pressure and hybrid signals. The dip is due to the rapid pressure loss of opening the valve rapidly, and the gradual rise is due to the upstream bleed valve compensating by increasing the flow to the load tank to bring the pressure back to the set point. The opposite occurs on the decreasing steps, which is why there is a gradual decrease in flow rate after the initial rapid decrease as the excess pressure bleeds off from the load tank and steady state is reached again.

Figure 66 clearly shows the final decreasing step of the test. Between 290s and 298, the hybrid sensor is following the slight overshoot as the thermal flow sensor settles to steady state. At 299s, the valve

begins closing, and both the pressure drop flow calculation and the hybrid sensor drop to within 200 SFPM of the final value within a second, easily matching the rotational speed of the valve.

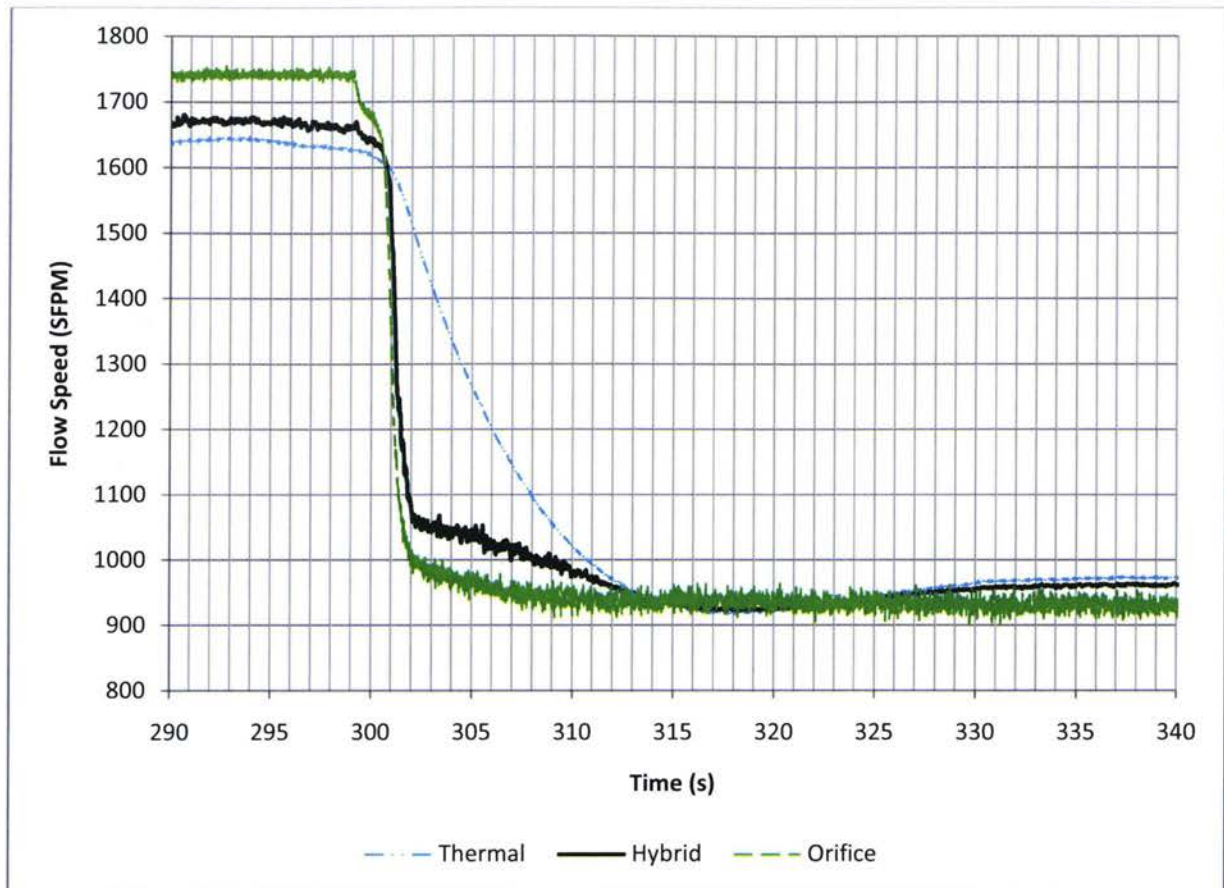


Figure 66: Hybrid Flow Sensor Step Response

Beginning around 312s, the thermal flow signal begins a slight overshoot, and the decreased rate of change causes the hybrid sensor to begin following the thermal flow signal more closely. Between 315s and 326s the three signals are nearly exactly overlapping. However by 335s, the signals have reached steady state. At this point, the pressure sensor is reading lower than the thermal flow sensor.

The hybrid equation and its application are relatively simple, and the only real means of improving the response is to fine tune the gains, signal filtering, and sample rates further. Assuming that the response of the thermal flow sensor cannot be improved by other means, the only place to improve is to get a

more detailed flow calibration to reduce the steady state uncertainty. Due to the rudimentary means of the pressure drop flow calculation, it leaves room for the largest improvement in steady state accuracy. This may be accomplished by including the actual upstream density, expansion, and discharge coefficients. However, considering that the restriction consists of a reducing elbow and a bushing, the discharge coefficient may be difficult to determine, but assuming that the other variables may be calculated, the discharge coefficient could be determined via calibration at steady state to a more accurate flow sensor.

In comparing the fast responding Omega flow sensor to the thermal flow sensor, it becomes apparent that simply increasing the response of the thermal flow sensor can only be accomplished with a loss of steady state accuracy. The very fast responding pressure sensors will still suffer from relatively noisy signals at steady state regardless of the thoroughness of the calibration. Filtering the data may provide some relief. However, calculating flow off pressure drop is still susceptible to offset errors when operating at flow rates far away from the calibrated range. Ultimately, even if the two sensors respond ideally and instantaneously, the hybrid algorithm simply provides a way to average the output of two redundant sensors which is not a hindrance at all.

4.3 Flow Control using the Hybrid Algorithm

To determine if any improvement in flow control could be determined, all three flow sensors were used as the feedback signal for the controller. Gains were changed slightly in each case to reduce oscillations. The same command signal was used in each case so that the different responses could be compared to each other. The first run used the thermal flow sensor as the feedback signal, the second run used the pressure drop flow calculation as the feedback signal, and the third run used the hybrid sensor for feedback. Figure 67, Figure 68, and Figure 69 show each of the individual sensor responses compared to the different runs. Figure 67 shows that the hybrid sensor responds ever so slightly faster than the

thermal flow sensor, and with a smaller overshoot. However, there is a steady state offset error, but not nearly as bad as that of Run 2, which is the case using the feedback signal of the pressure drop flow calculation.

The slow response of Run 2 had to do with the decreased gain values that had to be used to reduce the oscillations of the control signal. Even then, some of the oscillations are apparent on Figure 68 between 210s and 230s.

Figure 69 shows the hybrid sensor response, and for Run 3, the faster response and smaller overshoot can be clearly seen. Additionally, the hybrid signal generally lies within ± 75 SFPM uncertainty of the thermal flow sensor at steady state.

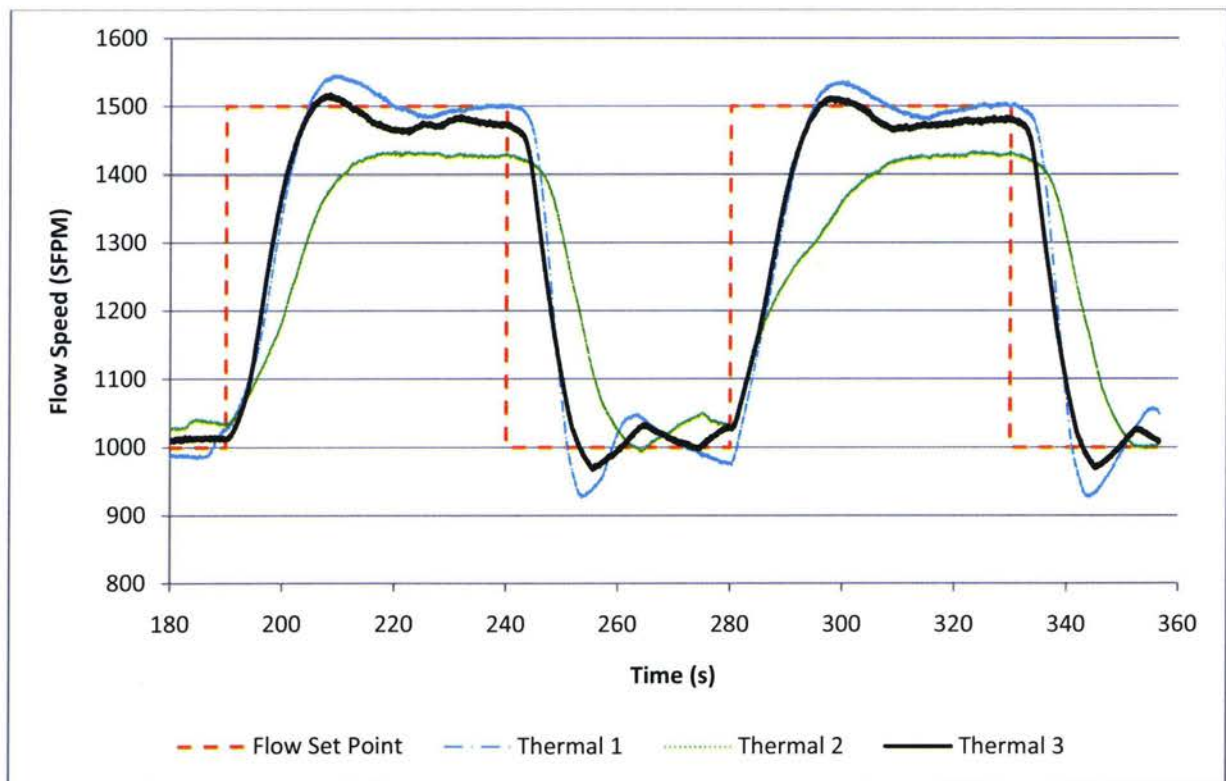


Figure 67: Flow Control: Thermal Flow Sensor Response

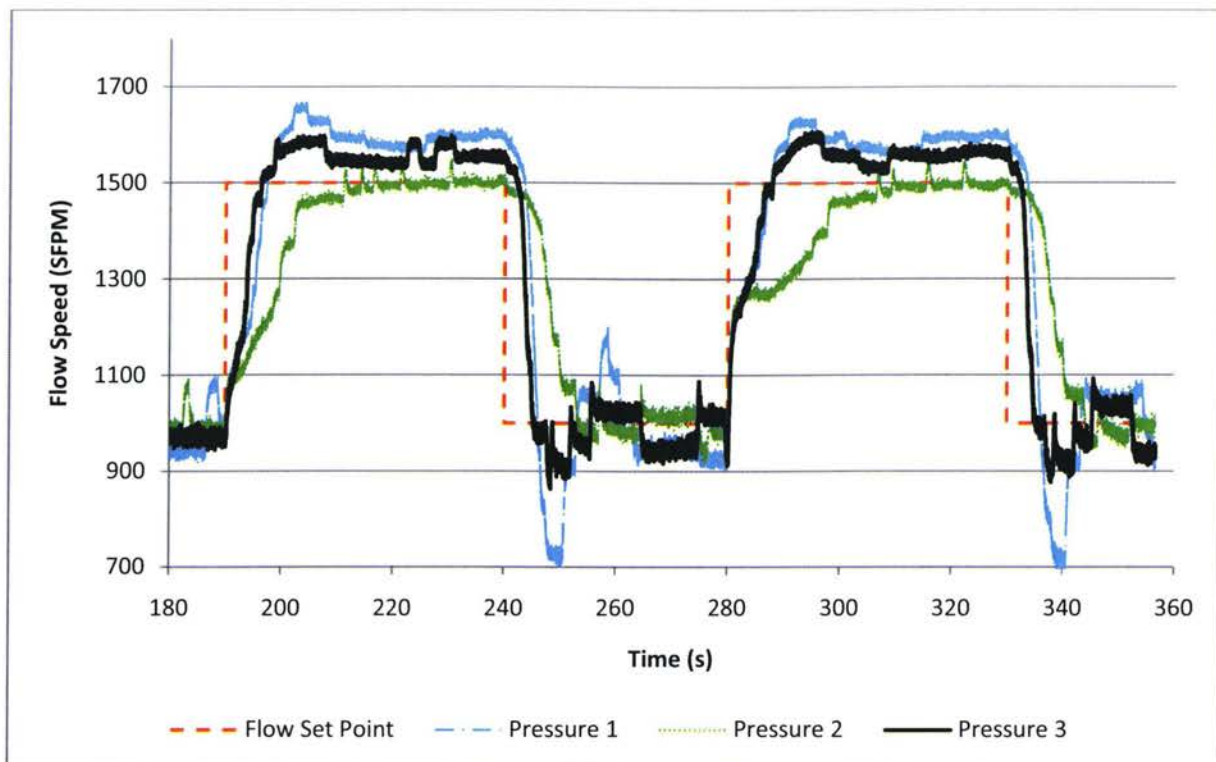


Figure 68: Flow Control: Pressure Drop Flow Calculation Response

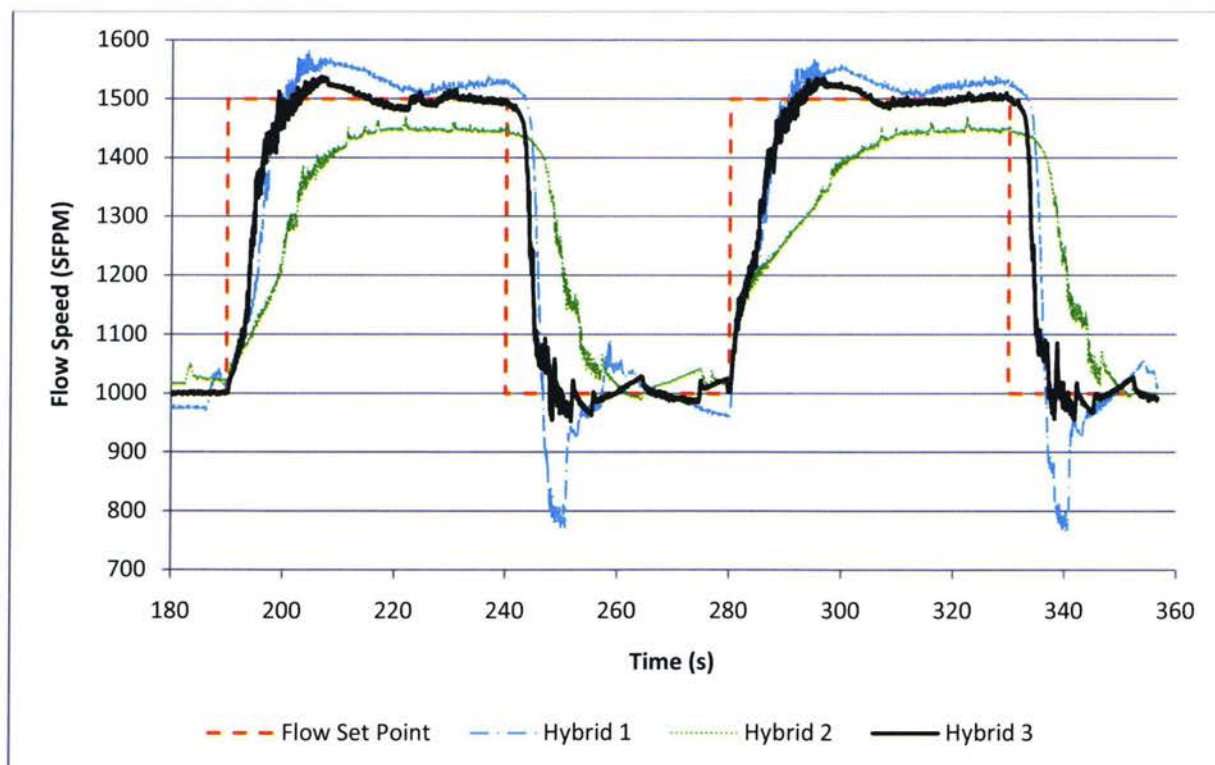


Figure 69: Flow Control: Hybrid Flow Sensor Response

The decrease in overshoot is most obvious on the decreasing steps. When using the thermal flow sensor for control, large overshoots of up to 200 SFPM occur. However, this is prevented using the hybrid flow sensor, and is shown clearly in Figure 70. As well, the faster response of the hybrid sensor controlled system is visible, and is approximately 1s faster over the normal thermal flow sensor controlled system.

Figure 71 shows the thermal, pressure, and hybrid flow sensor responses during Run 3, which is when the hybrid flow sensor provides control feedback. Once again, the faster response of the hybrid signal is apparent, along with a slight offset error.

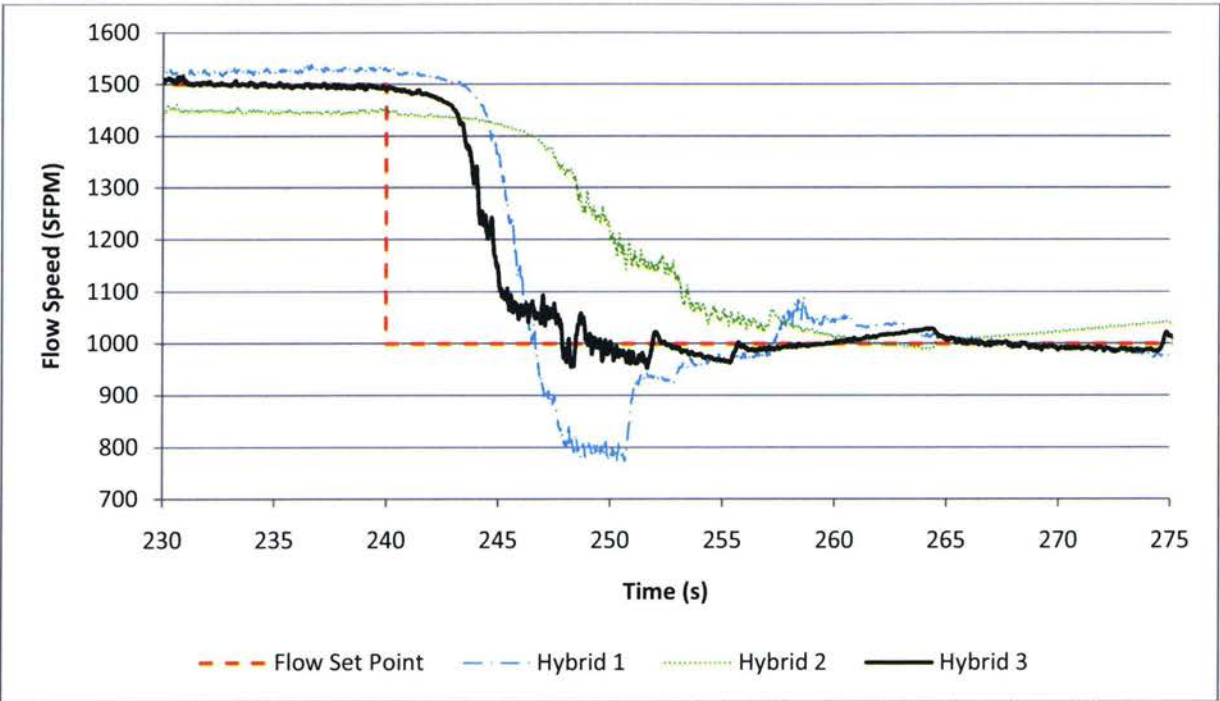


Figure 70: Decreasing Step Response: Hybrid Flow Sensor

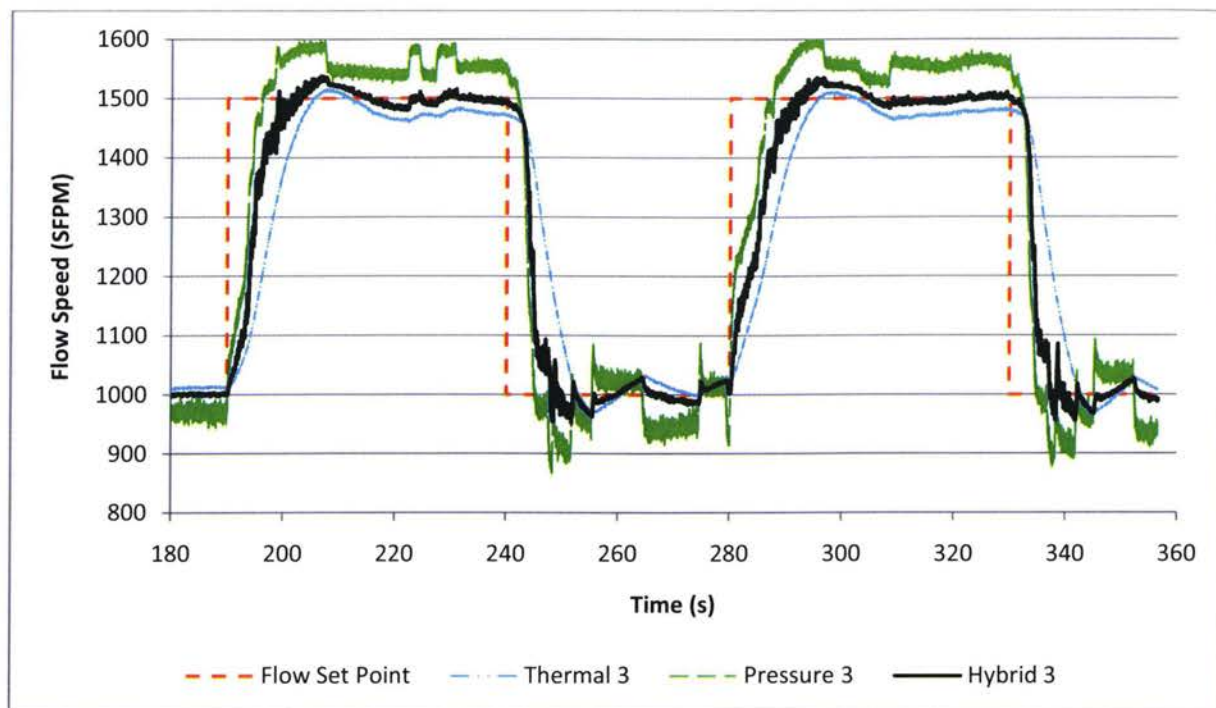


Figure 71: Run 3 Outflow Control with Hybrid Sensor Feedback

5 Conclusion and Future Research

This section is intended to summarize the work done on the test rig, results of the experiments performed, and outline possible future work and research.

5.1 Conclusion

The test rig has been built and can be used in its current form for tests. However, the heaters still need to be installed, as well as the pressure safety valves and several actuators. Overall, the SIMULINK control system interfaces smoothly with the instrumentation. However, for simultaneous temperature and flow control two more Omega flow sensors will need to be purchased.

Not all of the theory laid out in this thesis could be validated by experimentation. The pressure drop across the channel was too small to be measured accurately for a flow calculation. The pressure drop across a partially opened valve, though measurable, was not repeatable. This was most likely due to hysteresis and random interaction between the seal and disc.

However, using two different redundant means of flow calculation to improve the overall flow measurement was shown to be possible. By measuring the pressure drop across a flow restriction, flow can be repeatable calculated, and then compared with the measurement of the thermal flow sensor. Generally, when the flow rate changes it is due to either a gradual pressure change or a faster valve position change. The thermal flow sensor can accurately measure slight changes, but it lags heavily on detecting the large flow changes caused by the valve. Alternatively, the pressure drop flow calculation responds immediately to large flow changes, but oscillates heavily at steady state, making minor changes in flow rate difficult to detect.

Since the overshoot of the thermal flow sensor is not as large as expected in the theoretical section, only the weighted average needed to be used. The error switching portion of the theory was not necessary.

The weighted average assumes that the pressure drop flow calculation will have a single large step whenever a valve is moved, whereas the thermal flow sensor will detect a gradual rise. By differentiating the signals, the pressure drop flow calculation will have a very large spike initially, and then drop immediately back down to zero. On the other hand, the thermal flow sensor will not have any spikes in the differential, but instead have a sustained non-zero derivative during transients. Since the flow rate change is closer to a step change, one would expect the actual flow rate to be similar to that detected by the pressure drop flow calculation. Therefore the weighted average was developed to use the sustained, non-zero derivative to form a weighted average.

In theory, this was easy to be seen since the signals are smooth. In practice, the signals needed to be heavily filtered and down sampled so that the derivative could be roughly determined. Once the derivative was found, a gain was applied such that it could change the bias of the average based on measured changes of the individual flow measurements. When the thermal flow sensor has a large rate of change, the weighted average will bias towards the pressure measurement, but when the thermal flow sensor has a small or zero rate of change, like at steady state, then the weighted average will be biased towards the thermal flow measurement.

Nevertheless, experiments demonstrated the feasibility of the hybrid sensor. Not only did the algorithm capture the benefits of each of the redundant flow measurements, but also demonstrated the ability to improve control response when used as a feedback signal. Although the pressure drop flow calculation responds faster, it does not provide a very smooth signal, which results in choppy and fluctuating control signals. These may cause unnecessary wear on the actuator over time, and the gains were reduced to minimize the oscillations. On the other hand, the slow thermal flow sensor response causes unnecessarily large overshoots. The hybrid sensor allowed corrections to both of these problems. By

providing a smooth steady state signal, unnecessary wear can be avoided, and at the same time having a fast response minimizes the overshoot.

5.2 Future Research

The construction of the new test rig and improvement in hardware has opened up many possible research areas. The new rig returns flow sharing capabilities back to the lab, without the loss of the recently developed temperature control capability. Having two temperature control channels in a flow sharing arrangement naturally leads to the possibility of combining the two research streams, such that flow sharing and temperature are controlled simultaneously. The load tank provides the new possibility of independent outlet pressure control by changing the outflow exit. On previous flow sharing tests, the outflow valve was essentially set and fixed in place, so the downstream pressure was directly controlled by the upstream pressure and flow rate.

Beyond flow sharing and temperature control, which were developed in the past, the new rig also opens up the possibilities of testing fault tolerance in temperature control systems. One such scheme could involve maintaining the temperature and pressure in the load tank if one channel 'failed' in some way. Essentially, the working channel would be forced to make up the difference of the faulty channel.

Valve hysteresis is another area where research could be expanded. All of the actuated valves have been equipped with potentiometers, which should allow for more in-depth research of electric valve performance in air flows, especially in conjunction with sensor ports mounted upstream and downstream of each valve.

Accurate thermodynamic modeling of the entire test rig could also prove to be a challenging research topic. Initially, it was desired to build a SIMULINK model that could be used as a virtual sandbox to simulate the rig such that future changes to the control systems could be tested safely in advance. This was attempted, but too many assumptions significantly reduced confidence in the results.

Sensor fusion could be developed much more effectively as more accurate models of the system are developed. The simple hybrid algorithm in this thesis is essentially just a weighted average between two redundant flow sensors. Actual sensor fusion across the entire system requires a way to predict what each sensor should be measuring based on the signal of another sensor and vice versa. This may require analytical redundancy in the system which would require an accurate model.

As eluded to earlier, fault detection, identification, and accommodation could be another possible research topic. Two similar channels would allow for a simulated fault in one channel, while the other channel can accommodate, if required, after detection and identification of the fault. Sensor fusion and analytical redundancy could also play a role in detecting faults, especially soft sensor faults. The hybrid sensor also lends itself to fault tolerance by incorporating fault detection into the weighting function.

Heat exchanger analysis will also be easier to perform on this test rig due to the sensor ports at each inlet and exit. Other flow sensor tests and developmental work could also be performed on the new rig.

A basic framework for future research of the rig may be the design and model of a control system for the simultaneous control of flow, temperature, and pressure of the load tank. After the model, or simulation, is validated with experimental results, the model may be used to form an analytically redundant system in conjunction with sensor fusion. From this research, the fault detection, identification, and accommodation algorithms can most likely be readily developed. Beyond this, research could look into prognostics or fault prediction or new control schemes. Specific component research, such as valve hysteresis studies and heat exchanger or sensor analysis, could be integrated into the existing models to improve accuracy over previous models.

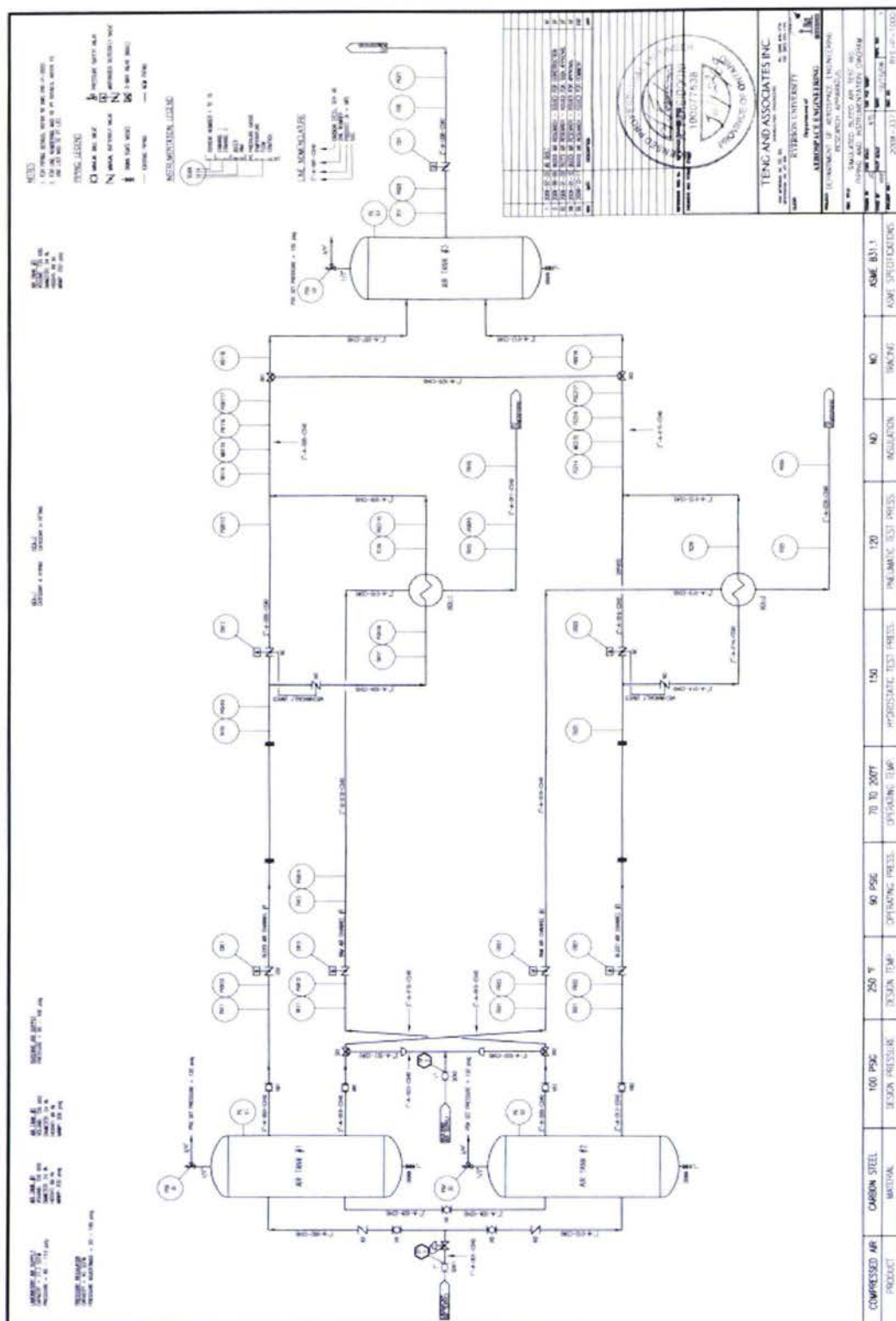
References

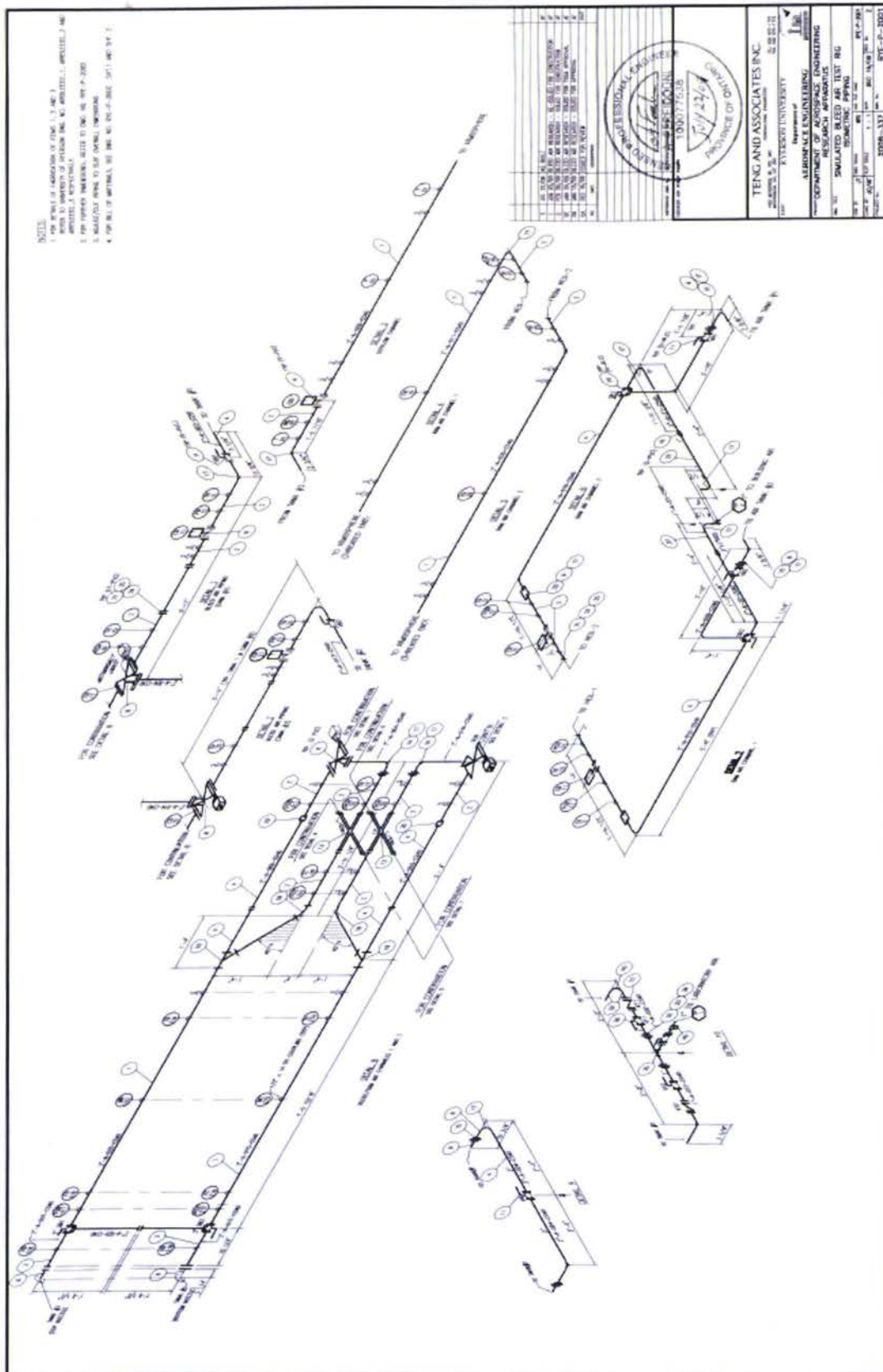
- Accardo, D., Esposito, F., Cimmino, G., Moccia, A., Ciniglio, U., & Corrado, F. (2004). Integration of Advanced Altimetric Systems for UAV Vertical Navigation During Landing Manoeuvres. *3rd "Unmanned Unlimited" Technical Conference, Workshop, and Exhibit* (pp. 1-12). Chicago: AIAA.
- Al-Dhaher, A. H., Farsi, E. A., & Mackesy, D. (2005). Data Fusion Architecture - An FPGA Implementation. *IMTC 2005 - Instrumentation and Measurement* (pp. 1985-1990). Ottawa: IEEE.
- Bao, G. (2003). *Fault-Tolerant Flow Sharing Control of Aircraft Engine Bleed Air System*. London: The University of Western Ontario.
- Bi-Torq. (2008, December 4). Quote: 0030816. La Fox, Illinois, USA.
- Buss, L. B. (1984). "Electric Airplane" Environmental Control Systems Energy Requirements. *IEEE 5th Annual Symposium* (pp. 250-255). Dayton: IEEE.
- Chan, C.-H. (2003). *Actuator Hysteresis Modelling and Compensation with an Adaptive Search Space Based Genetic Algorithm*. Toronto: Ryerson University.
- Chan, C.-H. (2001). *Design, Building, and Experiment on the Bleed Air Sharing Control System Emulation*. Toronto: Ryerson University.
- Cresnik, P., & Chong, J. (2009, April 27). Alternative Wafer and Lug-Style Butterfly Valves. Mississauga, Ontario, Canada.
- C-T Products Company. (n.d.). *Sylvania SureHeat Jet Air Heaters and SureHeat MAX Air Heaters*. Retrieved May 5, 2009, from C-T Products Company: <http://www.ctproductscompany.com/sylvania-SureHeat-Jet-SureHeat-Max.htm>
- Day, C. (2005). *Fault Detection and Accommodation of a Thermal-Type Flow Sensor in an Aircraft Bleed Air System*. MEng Project, Ryerson University, Mechanical Engineering, Toronto.
- Doebelin, E. O. (1966). *Measurement Systems: Application and Design* (3rd ed.). New York, New York, USA: McGraw-Hill, Inc.
- Eichler, J. (1975). Simulation Study of an Aircraft's Environmental Control System Dynamic Response. *Journal of Aircraft*, 12 (10).
- Elangovan, R., & Brushwood, D. L. (1985). Transient Model of a Pneumatic Ejector: Application to the Simulation of Aircraft Bleed Air Temperature Control Systems. *American Control Conference* (pp. 1187-1193). Boston: IEEE.
- Ensign, T. R. (2007). Performance and Weight Impact of Electric Environmental Control System and More Electric Engine on Citation CJ2. *45th AIAA Aerospace Science Meeting and Exhibit* (pp. 1-20). Reno: AIAA.
- Ensign, T. R. (2008). Sensitivity Studies of Electric Systems on Business Jet Range. *46th AIAA Aerospace Sciences Meeting and Exhibit* (pp. 1-29). Reno: AIAA.
- Ensign, T. R., & Gallman, J. W. (2006). Energy Optimized Equipment Systems for General Aviation Jets. *44th AIAA Aerospace Sciences Meeting and Exhibit* (pp. 1-16). Reno: AIAA.

- Farnam-Tutco. (n.d.). *Air Heaters by Farnam*. Retrieved May 5, 2009, from Farnam-Tutco: <http://www.farnam-custom.com/index.php>
- Hardacre, S. (2002). *Bleed Air Sharing Control Simulation*. Toronto: Ryerson University.
- Hodal, P. (2005). *Bleed Air Temperature Regulation System: Modeling, Control, and Simulation*. Toronto: Ryerson University.
- Humphreys, W. M., & Culliton, W. G. (2008). An Autonomous Sensor System Architecture for Active Flow and Noise Control Feedback. *26th AIAA Aerodynamic Measurement Technology and Ground Testing Conference* (pp. 1-14). Seattle: AIAA.
- Incropera, F. P., & DeWitt, D. P. (2002). *Fundamentals of Heat and Mass Transfer* (5th Edition ed.). Danvers, Massachusetts, USA: John Wiley & Sons, Inc.
- Jarrell, J., Gu, Y., Seanor, B., & Napolitano, M. (2008). Aircraft Attitude, Position, and Velocity Determination Using Sensor Fusion. *GNC Conference and Exhibit* (pp. 1-17). Honolulu: AIAA.
- Jiang, C., Liu, G., & Jiang, J. (2005). A Self-Validating Algorithm for Hot Thermistor Constant Differential Temperature Air Flow Sensor. *IEEE Conference on Control Applications* (pp. 669-674). Toronto: IEEE.
- Keithley Instruments, Inc. (2007). *Understanding New Developments in Data Acquisition, Measurement, and Control: A Practical Guide to High Performance Test and Measurement* (1st ed.). Cleveland, Ohio, USA: Keithley Instruments, Inc.
- Kong, F.-T., Chen, Y.-P., Xie, J.-M., & Zhou, Z.-D. (2005). Distributed Temperature Control System Based on Multi-Sensor Data Fusion. *4th International Conference on Machine Learning and Cybernetics* (pp. 494-498). Guangzhou: IEEE.
- Liu, G., & Lam, C. H. (2003). *Patent No. US Patent 6782701*. USA.
- Liu, G., Bao, G., Lam, C. H., & Jiang, J. (2005). A Master-Slave Approach to Aircraft Engine Bleed Flow Sharing Control. *13 (6)*, 1100-1106.
- Mitchell, H. B. (2007). *Multi-Sensor Data Fusion*. Berlin, Germany: Springer.
- Moir, I., & Seabridge, A. (2008). *Aircraft Systems: Mechanical, Electrical, and Avionics Subsystems Integration* (3rd ed.). Chichester, West Sussex, England: John Wiley & Sons Inc.
- Moir, I., & Seabridge, A. (2003). *Civil Avionics Systems*. Reston, Virginia, USA: AIAA.
- Olin, J. G. *Measurements & Control: Industrial Thermal Mass Flowmeters*. Sierra Instruments.
- Omega. (n.d.). *FMA-900: General-purpose Air Velocity Transducers*. (Omega) Retrieved June 10, 2009, from omega.ca: <http://www.omega.ca/shop/pptsc.asp?ref=FMA900>
- OSRAM Sylvania. (n.d.). *SureHeat Jet Control: Air Heater Control System*. Retrieved May 5, 2009, from Sylvania: <http://www.sylvania.com/content/display.scfx?id=003682486>
- Pellegrini, L. F., Gandolfi, R., & Lima da Silva, G. A. (2007). Exergy Analysis as a Tool for Decision Making in Aircraft Systems Design. *45th AIAA Aerospace Science Meeting and Exhibit* (pp. 1-12). Reno: AIAA.

- Perry, R. H., & Green, D. W. (2008). *Perry's Chemical Engineers' Handbook* (8th Edition ed.). McGraw-Hill.
- Rathburn, T. F., & Washburne, T. P. (1993). Pixel Level Sensor Fusion. *2nd Annual AIAA SDIO Interceptor Technology Conference* (pp. 1-5). Alburguerque: AIAA.
- Rees, D. (1989). *Essential Statistics* (2nd Edition ed.). London, UK: Chapman and Hall.
- Shang, L., & Liu, G. (2007). Optimal Control of a Bleed Air Temperature Regulation System. *IEEE International Conference on Mechatronics and Automation* (pp. 2610-2615). Harbin: IEEE.
- Slingerland, R., & Zandstra, S. (2007). Bleed Air versus Electric Power Off-takes from a Turbofan Gas Turbine over the Flight Cycle. *7th AIAA Aviation Technology, Integration, and Operating Conference* (pp. 1-12). Belfast: AIAA.
- Smith, P., & Zappe, R. W. (2004). *Valve Selection Handbook* (5th Edition ed.). Burlington, Massachusetts, USA: Elsevier, Inc.
- Upp, E., & LaNasa, P. J. (2002). *Fluid Flow Measurement: A Practical Guide to Accurate Flow Measurement*. Boston: Elsevier.
- White, F. M. (2003). *Fluid Mechanics* (5th Edition ed.). Boston, Massachusetts, USA: McGraw-Hill.
- Yiu, F. Y.-F. (2004). *Adaptive Measurement Control of a Thermal Flow Sensor*. Toronto: Ryerson University.
- Yuhas, A., & Ray, R. (1992). Effects of Bleed Air Extraction on Thrust Levels of the F404-GE-400 Turbofan Engine. *AIAA/SAE/ASME/ASEE 28th Join Propulsion Conference and Exhibit* (pp. 1-12). Nashville: AIAA.

Appendix A: TSSA Approved Drawings





BILL OF MATERIAL						QTY BY REVISION		REMARKS / REFERENCE
ITEM	SIZE	DESCRIPTION				0		
1	2"	PIPE, SCH40, SEAMLESS C.S., 11 1/2" NPT BOTH ENDS, CUT LENGTH @ 7'-2" c/w (5) 1/2" HALF COUPLINGS	ASTM A106 GR. B		5		RYERSON DWG NO. BLEEDAIR2_01	
2	2"	PIPE, SCH40, SEAMLESS C.S., 11 1/2" NPT BOTH ENDS, CUT LENGTH @ 12' c/w (2) 1/2" HALF COUPLINGS	ASTM A106 GR. B		19		RYERSON DWG NO. BLEEDAIR_02	
3	2"	PIPE, SCH40, SEAMLESS C.S., 11 1/2" NPT BOTH ENDS, CUT LENGTH, 8' c/w (1) 1/2" HALF COUPLING	ASTM A106 GR. B		2		RYERSON DWG NO. BLEEDAIR_03	
4	2"	PIPE, SCH40, SEAMLESS C.S.	ASTM A106 GR. B		40 FT.			
5	2" x 6" LG.	PIPE NIPPLE, SCH40 C.S., THREADED BOTH ENDS	ASTM A106 GR. B		10			
6	2" x 4" LG.	PIPE NIPPLE, SCH40 C.S., THREADED BOTH ENDS	ASTM A106 GR. B		21			
8	2"	ACTUATED BUTTERFLY VALVE, 3-WAY, TEE-LINKAGE ASSEMBLY, NPT FLANGED CONN. (ARRANGEMENT #2)	CRN 0C0569.95		4			
9	2"	BUTTERFLY VALVE, MOV. FLANGED CONN.	CRN 0C0569.95		5			
10	2"	BALL VALVE, MANUAL, 3-WAY, FLANGED, NPT CONN., TEE PORT	CRN 0C5091.5		4			
11	2"	BALL VALVE, MANUAL, FLANGED, NPT CONN., BRASS BODY	CRN 0C5091.5		5			
12	1"	CHECK VALVE, WAFFER TYPE, FLANGED NPT CONN.	CRN 0A10304.5		2			
13	2"	HEAT EXCHANGER (CATEGORY H FITTING), ALUMINUM BODY, c/w ALUMINUM FLANGED CONNECTIONS	CRN IN PROGRESS		2			
15	2"	UNION, 150#, FEMALE NPT CONN.	CRN 0A10304.5		6			
16	2"	UNION, 150#, MALE / FEMALE NPT CONN. (CRANE #25.5 H)			2			
17	2" x 90'	ELBOW, 150# FEMALE NPT CONN.	CRN 0A1087.95		17			
18	2" x 45'	ELBOW, 150# FEMALE NPT CONN.	CRN 0A1087.95		2			
19	2"	LATERAL "Y", FEMALE NPT CONN.	CRN 0A0570.95		2			
20	2"	FULL COUPLING, 150#	ASME B16.3, ASTM A395, CRN 0A1034.5		6			
21	FLANGE GASKET	FLANGE GASKET, TEFLON			17			
24	2"	FLANGE, 150# R.F. THREADED	ASME B16.5, ASTM A105, CRN 0B0565.95R2		34			
25	5/8"x3 3/4" LG	ALLOY STEEL STUDS c/w	SA 193 B7		68			
		HEAVY HEX NUTS	SA 194 2H		136			
26	3 1/4" SQ.	CHANNEL, GALV'D STEEL, (UNISTRUT, P1001C3 (12 GA.))			9 FT.			
27	5/8" x 3 1/4"	CHANNEL, GALV'D STEEL, (UNISTRUT, P1001 (12 GA.))			24 FT.			
30	2 1/2"	PIPE CLAMP (UNISTRUT, P2042) C/W SLOTTED HEX HEAD SCREW AND NUT			17			
31	PIPE GASKET	UNICUSHION, CUT LENGTH 7 1/2" FOR EACH CLAMP (UNISTRUT, P2600)			17			

LICENSED PROFESSIONAL ENGINEER
 A. FERREDOONI
 100077538
 P.E. OF ONTARIO

DATE: DEC 9/09	BY: JT	ENG. FILE No.:	JOB DESCRIPTION: SIMULATED BLEED AIR TEST RIG	RYERSON UNIVERSITY Department of AEROSPACE ENGINEERING	
DWG. No. RYE-P-2002-1	JOB ORDER No. 2008-337	BILL OF MATERIAL No. RYE-P-2002-1	REV 3		
TENG AND ASSOCIATES INC. <small>1000 SHEPPARD AVENUE EAST, SUITE 100, AURORA, ONTARIO M1T 3X4</small>					

BILL OF MATERIAL			QTY BY REVISION		REMARKS / REFERENCE & DELIVERY
ITEM	SIZE	DESCRIPTION	QTY	0	
32	1" x 6" LG.	PIPE NIPPLE, SCH40 C.S., THREADED BOTH ENDS	ASTM A106 GR. B	2	
33	1" x 4" LG.	PIPE NIPPLE, SCH40 C.S., THREADED BOTH ENDS	ASTM A106 GR. B	8	
34	1"	UNION, 150#, FEMALE NPT CONN. (CRANE #250 H)		2	
35	1"	TEE, 150#, FEMALE NPT CONN.	ASME B16.3, ASTM A395, CRN 0A10304.5	5	
36	1"	BALL VALVE, MANUAL, NPT CONN., BRASS BODY	CRN DC5091.5	2	
37	1"	PIPE, SEAMLESS, SCH40 C.S.	ASTM A106 GR. B	6 FT.	
38	1/4" x 6 5/8"	BASE ANGLE (FABRICATED)		14	
39	1 5/8" x 1 5/8"	CHANNEL, GALV'D STEEL, (UNISTRUT, P1000 (12 GA.))		20 FT.	
40	2" x 1 7/8"	90° BRACKET (UNISTRUT, P1026)		9	
41	2" x 1"	REDUCER, FEMALE NPT CONN.	CRN 0A1087.95	4	
42	1" x 90°	ELBOW, 150# FEMALE NPT CONN.	ASME B16.3, ASTM A395, CRN 0A10304.5	4	
43	1/2" x 3/4"	PRESSURE SAFETY VALVE, 1/2" MNPT x 3/4" FNPT, SET AT 120 PSIG	ASME SECTION VII	3	
44	1"	GATE VALVE, MANUAL, NPT CONNECTION, 150#	CRN 0A10304.5	3	
45	3/16" x 1 5/8"	LARGE KNEE BRACE (FABRICATED)		4	
46	1/2" x 4 1/2"	HILTI 1/2" x 4 1/2" LONG GALV'D, KWIK BOLT 3 EXPANSION ANCHOR C/W NUT AND WASHER (3 1/4" EMBEDMENT)			
47	1/2"	CHANNEL STUD NUT WITH SPRING (UNISTRUT, P23XX TO FIT), C/W WASHERS AND NUTS TO SUIT			
48	3/16" x 1 5/8"	SMALL KNEE BRACE (FABRICATED)		5	
49	1"	AIR PRESSURE REGULATOR, ADJUSTABLE DISCH. PRESSURE SETTING 20 TO 100 PSIG	CRN 0C0723.95	1	

LICENSED PROFESSIONAL ENGINEER
A. FERRELLI
100077538
STATE OF CALIFORNIA

DATE: DEC 9/09 BY: JT

DWG. No. RYE-P-2002-1

TENG AND ASSOCIATES INC.

ENG. FILE No.:

JOB ORDER No. 2008-337

JOB DESCRIPTION SIMULATED BLEED AIR TEST RIG

BILL OF MATERIAL No. RYE-P-2002-1

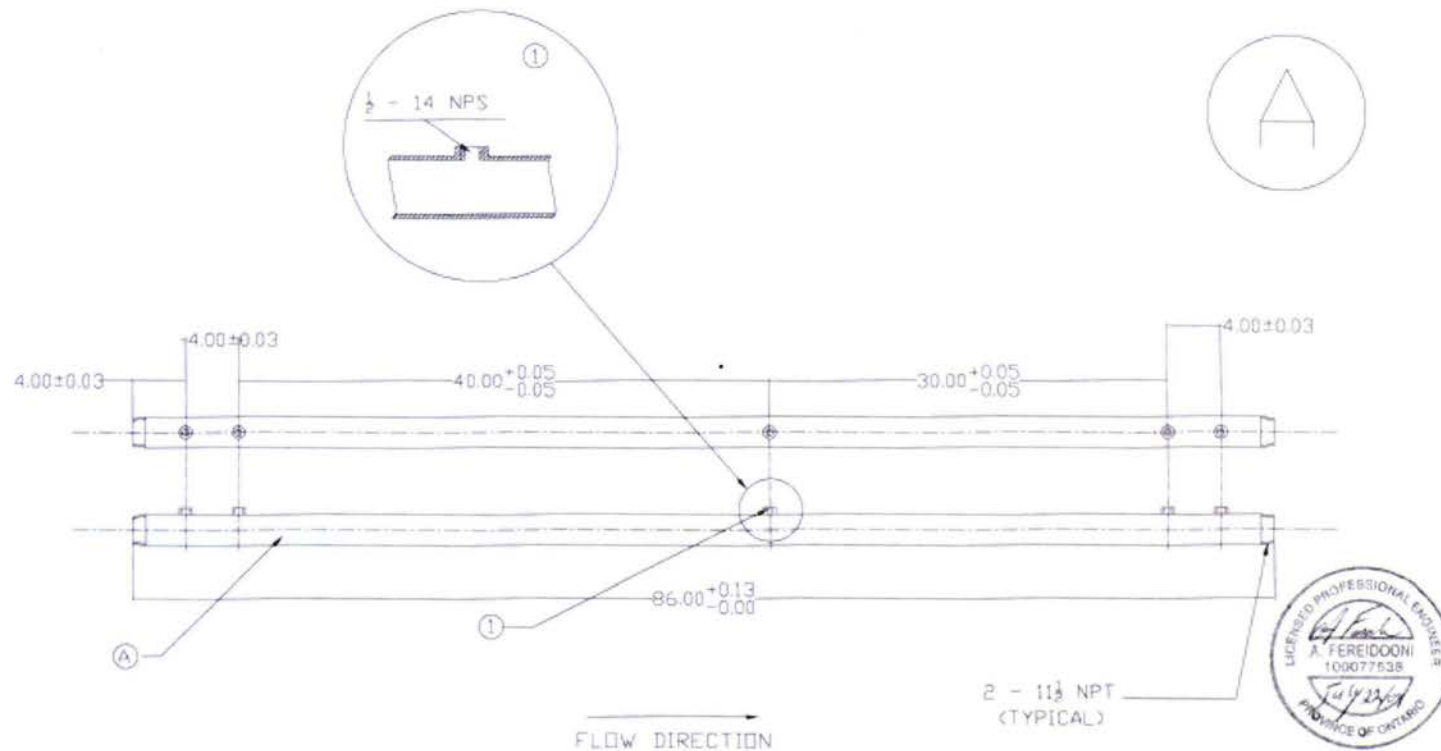
SHT 2 OF 2

RYERSON UNIVERSITY

Department of

AEROSPACE ENGINEERING

AEROSPACE



ITEM	PART NUMBER	DESCRIPTION	QTY	DIMENSIONS: INCHES
				TOLERANCES
A		2' - CS Sch. 40 Pipe	5	AS INDICATED
1		1/2" - 14 NPS (see 1)	5	Fabrication ONLY

NOTES: Hydrastatic Testing as Required
Prime and Paint Blue

RYERSON UNIVERSITY

Department of

AEROSPACE ENGINEERING

TITLE: 86" Pipe w/ Couplings

DWG. NO.: BleedAir2_01

DRAWN BY:

PC

CHECKED BY:

APPROVED BY:

DATE:

12/02/08

FILENAME:

BA2_PIPE_86in

REVISION:

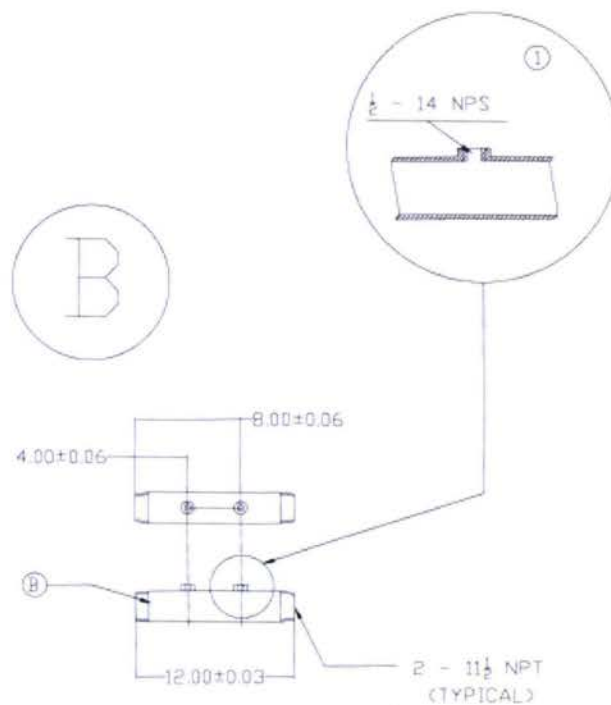
3


OTHER:

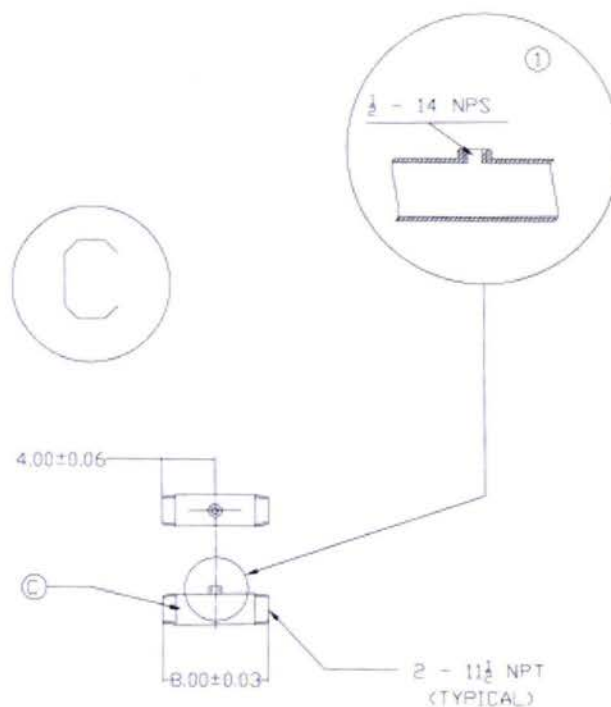
AEROSPACE



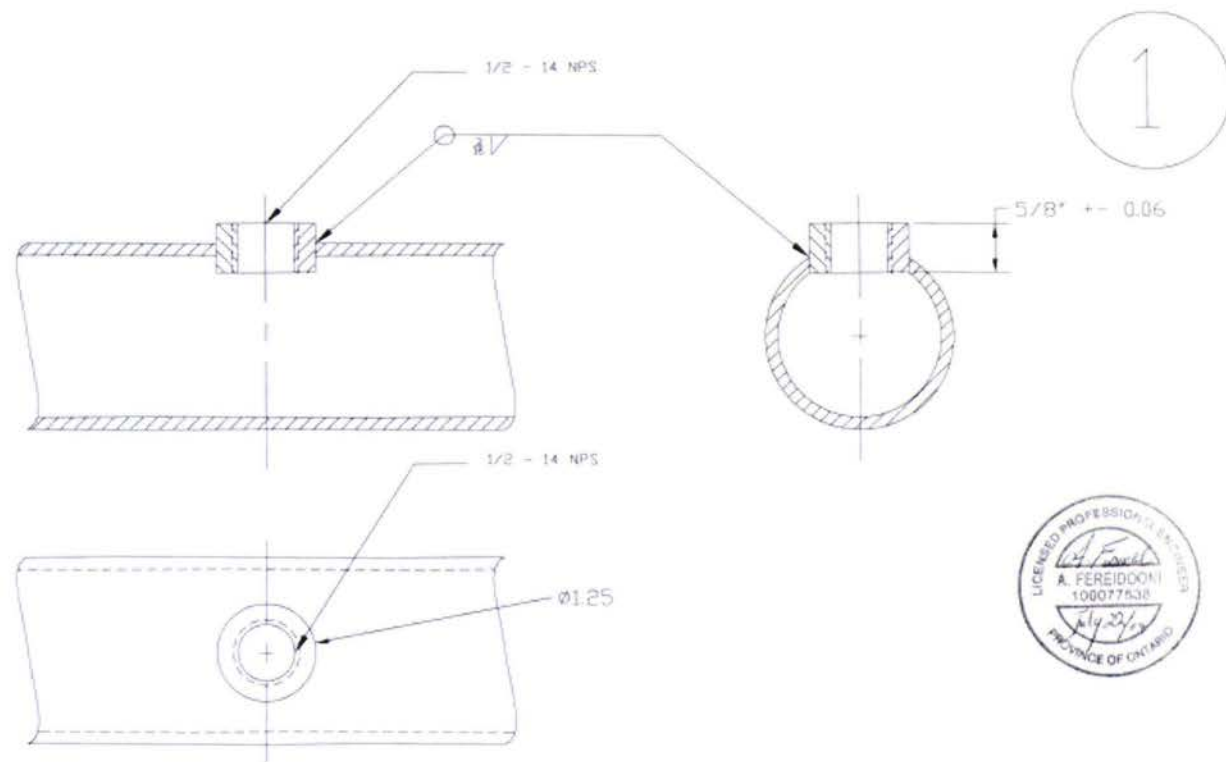
RYERSON UNIVERSITY



ITEM	PART NUMBER	DESCRIPTION	QTY	DIMENSIONS, INCHES	RYERSON UNIVERSITY Department of AEROSPACE ENGINEERING		 AEROSPACE RYERSON UNIVERSITY				
				TOLERANCES							
B		2" - CS. Sch. 40 Pipe	19	AS INDICATED Fabrication ONLY	TITLE: 12" Pipes w/ Couplings DWG. NO.: BleedAir2_02						
1		1/2 - 14 NPS (see 1)	2								
NOTES: Hydrottest as Required Prime and Paint Blue					DRAWN BY: PC	CHECKED BY:	APPROVED BY:	DATE: 12/02/08	FILENAME: BA2_PIPE_12in	REVISION: 4	OTHER:



ITEM	PART NUMBER	DESCRIPTION	QTY	DIMENSIONS INCHES	RYERSON UNIVERSITY Department of AEROSPACE ENGINEERING TITLE: 8" Pipe w/ Coupling DWG. NO.: BleedAir2_04	 RYERSON UNIVERSITY
				TOLERANCES:		
C		2" - CS Sch. 40 Pipe	2	AS INDICATED Fabrication ONLY		
1		1/2 - 14 NPS (see 1)	1			
NOTES: Hydratest as Required Prime and Paint Blue					DRAWN BY: PC CHECKED BY: APPROVED BY: DATE: 12/02/08 FILENAME: BA2_PIPE_Ban REVISION: 2 OTHER:	



ITEM	PART NUMBER	DESCRIPTION	QTY	DIMENSIONS: Inches
1	N/A	Welded Coupling for Sensor Connections		TOLERANCES As Indicated
NOTES: Couplings have National Pipe Straight threads				

RYERSON UNIVERSITY

Department of

AEROSPACE ENGINEERING

TITLE: Welded Coupling Connection

DWG. NO.: BleedAir2_03

DRAWN BY	CHECKED BY	APPROVED BY	DATE	FILENAME	REVISION	OTHER
			01/07/08	PIPE_Coupling	5	



TENG AND ASSOCIATES INC.

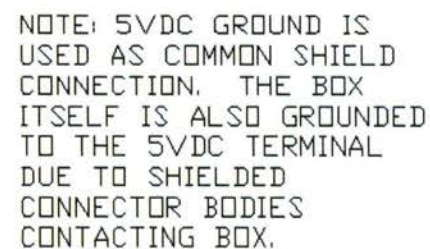
1450 Mayenside Drive
Suite 502
Mississauga, ON
L5T 2H2

Tel: 905 670 1779
Fax: 905 670 1775

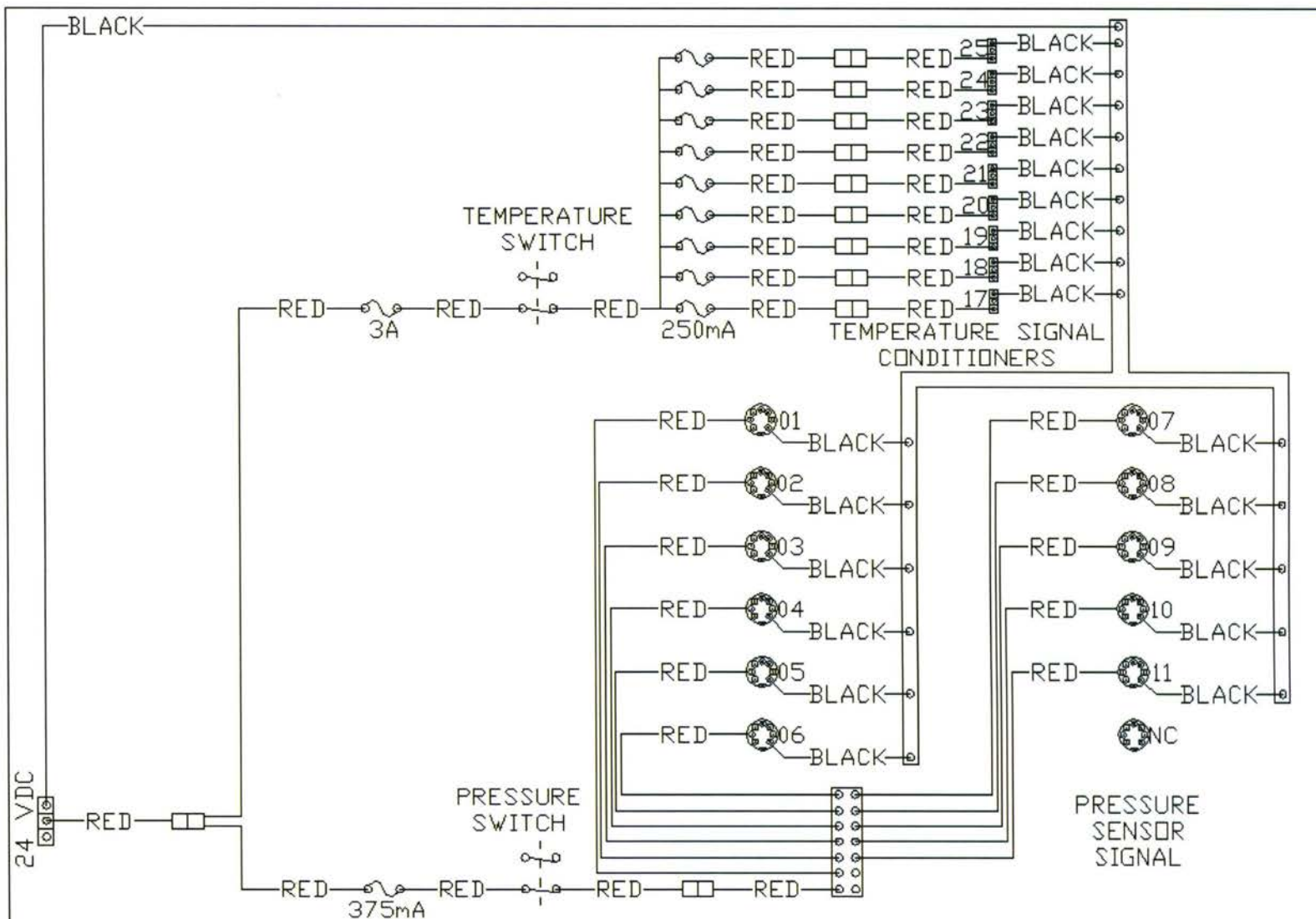
RYERSON UNIVERSITY

SIZE	SERVICE	LINE NO.	PIPING MATERIAL	SCH.	ORIGIN	TERMINATION	REFERENCE		OPERATING CONDITIONS		DESIGN CONDITIONS		FLUID	PHASE	REMARKS
							P&ID DRAWING NO.	PIPING / ISOMETRIC DRAWING NO.	PRESS.	TEMP.	PRESS.	TEMP.			
									PSI (GAUGE)	°F	PSI (GAUGE)	°F			
2"	A	001	CS	40	SOV1	1"-A-002-CS40 / 1"-A-012-CS40	RYE-P-1000	RYE-P-2001	120	70-200	150	250	Air	V	
1"	A	002	CS	40	1"-A-001-CS40	AIR TANK #1	RYE-P-1000	RYE-P-2001	120	70-201	150	250	Air	V	
2"	A	003	CS	40	AIR TANK #1	HTR-1	RYE-P-1000	RYE-P-2001	120	70-202	150	250	Air	V	
2"	A	004	CS	40	HTR-1	HEX-1	RYE-P-1000	RYE-P-2001	120	70-203	150	250	Air	V	
2"	A	005	CS	40	HEX-1	3B1	RYE-P-1000	RYE-P-2001	120	70-204	150	250	Air	V	
2"	A	006	CS	40	2"-A-004-CS40	2"-A-005-CS40	RYE-P-1000	RYE-P-2001	120	70-205	150	250	Air	V	
2"	A	007	CS	40	3B1	AIR TANK #3	RYE-P-1000	RYE-P-2001	120	70-206	150	250	Air	V	
2"	A	008	CS	40	AIR TANK #3	ATMOSPHERE	RYE-P-1000	RYE-P-2001	120	70-207	150	250	Air	V	
2"	A	009	CS	40	AIR TANK #2	3R2	RYE-P-1000	RYE-P-2001	120	70-208	150	250	Air	V	
2"	A	010	CS	40	3R2	HEX-1	RYE-P-1000	RYE-P-2001	120	70-209	150	250	Air	V	
2"	A	011	CS	40	HEX-1	ATMOSPHERE	RYE-P-1000	RYE-P-2001	120	70-210	150	250	Air	V	
2"	A	012	CS	40	1"-A-001-CS40	AIR TANK #2	RYE-P-1000	RYE-P-2001	120	70-211	150	250	Air	V	
2"	A	013	CS	40	AIR TANK #2	HTR-2	RYE-P-1000	RYE-P-2001	120	70-212	150	250	Air	V	
2"	A	014	CS	40	HTR-2	HEX-2	RYE-P-1000	RYE-P-2001	120	70-213	150	250	Air	V	
2"	A	015	CS	40	HEX-2	3B2	RYE-P-1000	RYE-P-2001	120	70-214	150	250	Air	V	
2"	A	016	CS	40	2"-A-014-CS40	2"-A-015-CS40	RYE-P-1000	RYE-P-2001	120	70-215	150	250	Air	V	
2"	A	017	CS	40	3B2	AIR TANK #3	RYE-P-1000	RYE-P-2001	120	70-216	150	250	Air	V	
2"	A	018	CS	40	AIR TANK #1	3R1	RYE-P-1000	RYE-P-2001	120	70-217	150	250	Air	V	
2"	A	019	CS	40	3R1	HEX-2	RYE-P-1000	RYE-P-2001	120	70-218	150	250	Air	V	
2"	A	020	CS	40	HEX-2	ATMOSPHERE	RYE-P-1000	RYE-P-2001	120	70-219	150	250	Air	V	
2"	A	021	CS	40	3R1	1"-A-023-CS40	RYE-P-1000	RYE-P-2001	120	70-220	150	250	Air	V	
2"	A	022	CS	40	3R2	1"-A-023-CS41	RYE-P-1000	RYE-P-2001	120	70-221	150	250	Air	V	
1"	A	023	CS	40	SOV1	2"-A-21-CS40 / 2"-A-22-CS40	RYE-P-1000	RYE-P-2001	120	70-222	150	250	Air	V	
2"	A	024	CS	40	AIR TANK #1 / AIR TANK #2	AIR TANK #2 / AIR TANK #1	RYE-P-1000	RYE-P-2001	120	70-223	150	250	Air	V	
2"	A	025	CS	40	3B1 / 3B2	3B2 / 3B1	RYE-P-1000	RYE-P-2001	120	70-200	150	250	Air	V	
Date							Project: RYERSON UNIVERSITY BLEED AIR SKID								
12/17/2008							Rev: 0A			Issued for Comment			Project No.: 2006-337		
1/13/2009							Rev: 0B			TSSA Approval			Client: Ryerson University		
7/22/2009							Rev: 0			As Built			Prepared By: JC		
													Checked By: AF		

TIE POINT NUMBER	FIRST LINE		SECOND LINE		REFERENCE			REMARKS
	SIZE	LINE NO.	SIZE	LINE NO.	P&ID DRAWING NO.	PIPING / ISOMETRIC DRAWING NO.	SERVICE	
1	1"	EXISTING LABORATORY AIR SUPPLY	1"	1"-A-002-CS40	RYE-P-1000	RYE-P-2001	Air	
2	1"	EXISTING BUILDING AIR SUPPLY	1"	1"-A-023-CS40	RYE-P-1000	RYE-P-2001	Air	
Date	Rev.	Description	Project:	RYERSON UNIVERSITY BLEED AIR SKID				
12/17/2008	0A	Issued for Comment	Project No.	2008-337	Document Title:	Tie-Point List		
1/13/2009	0B	TSSA Approval	Client:	Ryerson University	Document No.:			
7/22/2009	0	As Built	Prepared By:	JC	Checked By:	AF		



BOX #1 WIRING DIAGRAM			DALE MOLENAAR
5V CONNECTIONS		MAY 8, 2009	RYERSON UNIVERSITY



BOX #1 WIRING DIAGRAM
24V CONNECTIONS

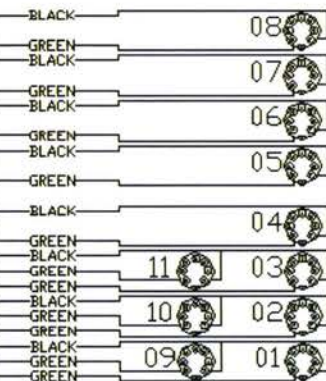
MAY 8, 2009

DALE MOLENAAR
RYERSON UNIVERSITY

BOARD 00 CB-68LPR

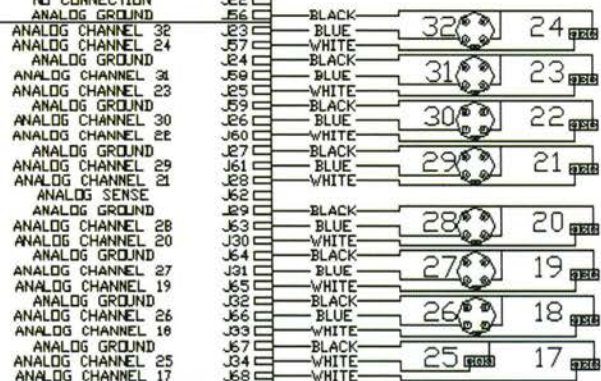
PFI 14/P2.6	J1
DIGITAL GROUND	J35
PFI 12/P2.4	J2
DIGITAL GROUND	J36
PFI 9/P2.1	J3
PFI 8/P2.0	J37
DIGITAL GROUND	J4
PFI 7/P1.7	J38
PFI 6/P1.6	J5
PFI 15/P2.7	J39
PFI 5/P1.5	J6
PFI 13/P2.5	J40
DIGITAL GROUND	J7
PFI 4/P1.4	J41
+5 V	J8
PFI 3/P1.3	J42
DIGITAL GROUND	J9
PFI 2/P1.2	J43
PFI 1/P1.1	J10
DIGITAL GROUND	J44
PFI 0/P1.0	J11
PFI 10/P2.2	J45
DIGITAL GROUND	J12
PFI 11/P2.3	J46
DIGITAL GROUND	J13
P0.3	J47
+5 V	J14
P0.7	J48
DIGITAL GROUND	J15
P0.2	J49
P0.6	J16
DIGITAL GROUND	J50
P0.1	J17
P0.5	J51
DIGITAL GROUND	J18
P0.0	J52
P0.4	J19
DIGITAL GROUND	J53
NO CONNECTION	J20
NO CONNECTION	J54
NO CONNECTION	J21
NO CONNECTION	J55
NO CONNECTION	J22
ANALOG GROUND	J56
ANALOG CHANNEL 16	J23
ANALOG CHANNEL 8	J57
ANALOG GROUND	J24
ANALOG CHANNEL 15	J58
ANALOG CHANNEL 7	J25
ANALOG GROUND	J59
ANALOG CHANNEL 14	J26
ANALOG CHANNEL 6	J60
ANALOG GROUND	J27
ANALOG CHANNEL 13	J61
ANALOG CHANNEL 5	J28
ANALOG SENSE	J62
ANALOG GROUND	J29
ANALOG CHANNEL 12	J63
ANALOG CHANNEL 4	J30
ANALOG GROUND	J64
ANALOG CHANNEL 11	J31
ANALOG CHANNEL 3	J65
ANALOG GROUND	J32
ANALOG CHANNEL 10	J66
ANALOG CHANNEL 2	J33
ANALOG GROUND	J67
ANALOG CHANNEL 9	J34
ANALOG CHANNEL 1	J68

NOTE: ANALOG CHANNEL NUMBERS HAVE BEEN MODIFIED TO MATCH SIMULINK. THESE TWO BOARDS PLUG INTO THE NI PCI-6224 M-SERIES A/D CARD.



BOARD 01 CB-68LPR

P0.30	J1
DIGITAL GROUND	J35
P0.28	J2
DIGITAL GROUND	J36
P0.25	J3
P0.24	J37
DIGITAL GROUND	J4
P0.23	J38
P0.22	J5
P0.31	J39
P0.21	J6
P0.29	J40
DIGITAL GROUND	J7
P0.20	J41
+5 V	J8
P0.19	J42
DIGITAL GROUND	J9
P0.18	J43
P0.17	J10
DIGITAL GROUND	J44
P0.16	J11
P0.26	J45
DIGITAL GROUND	J12
P0.27	J46
DIGITAL GROUND	J13
P0.11	J47
+5 V	J14
P0.15	J48
DIGITAL GROUND	J15
P0.10	J49
P0.14	J16
DIGITAL GROUND	J50
P0.9	J17
P0.13	J51
DIGITAL GROUND	J18
P0.8	J52
P0.12	J19
DIGITAL GROUND	J53
NO CONNECTION	J20
NO CONNECTION	J54
NO CONNECTION	J21
NO CONNECTION	J55
NO CONNECTION	J22
ANALOG GROUND	J56
ANALOG CHANNEL 32	J23
ANALOG CHANNEL 24	J57
ANALOG GROUND	J24
ANALOG CHANNEL 31	J58
ANALOG CHANNEL 23	J25
ANALOG GROUND	J59
ANALOG CHANNEL 30	J26
ANALOG CHANNEL 22	J60
ANALOG GROUND	J27
ANALOG CHANNEL 29	J61
ANALOG CHANNEL 21	J28
ANALOG SENSE	J62
ANALOG GROUND	J29
ANALOG CHANNEL 28	J63
ANALOG CHANNEL 20	J30
ANALOG GROUND	J64
ANALOG CHANNEL 27	J31
ANALOG CHANNEL 19	J65
ANALOG GROUND	J32
ANALOG CHANNEL 26	J66
ANALOG CHANNEL 18	J33
ANALOG GROUND	J67
ANALOG CHANNEL 25	J34
ANALOG CHANNEL 17	J68



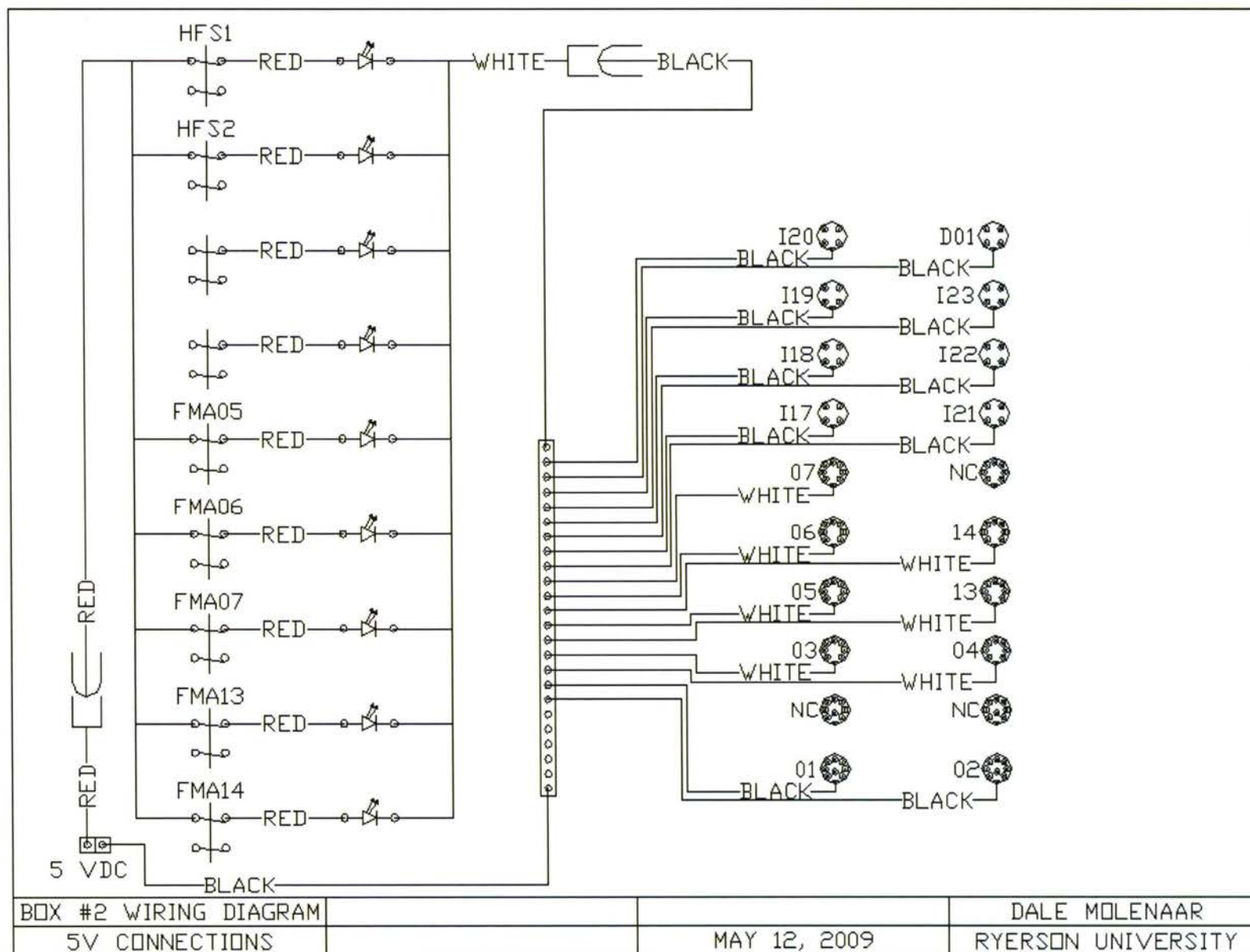
BOX #1 WIRING DIAGRAM

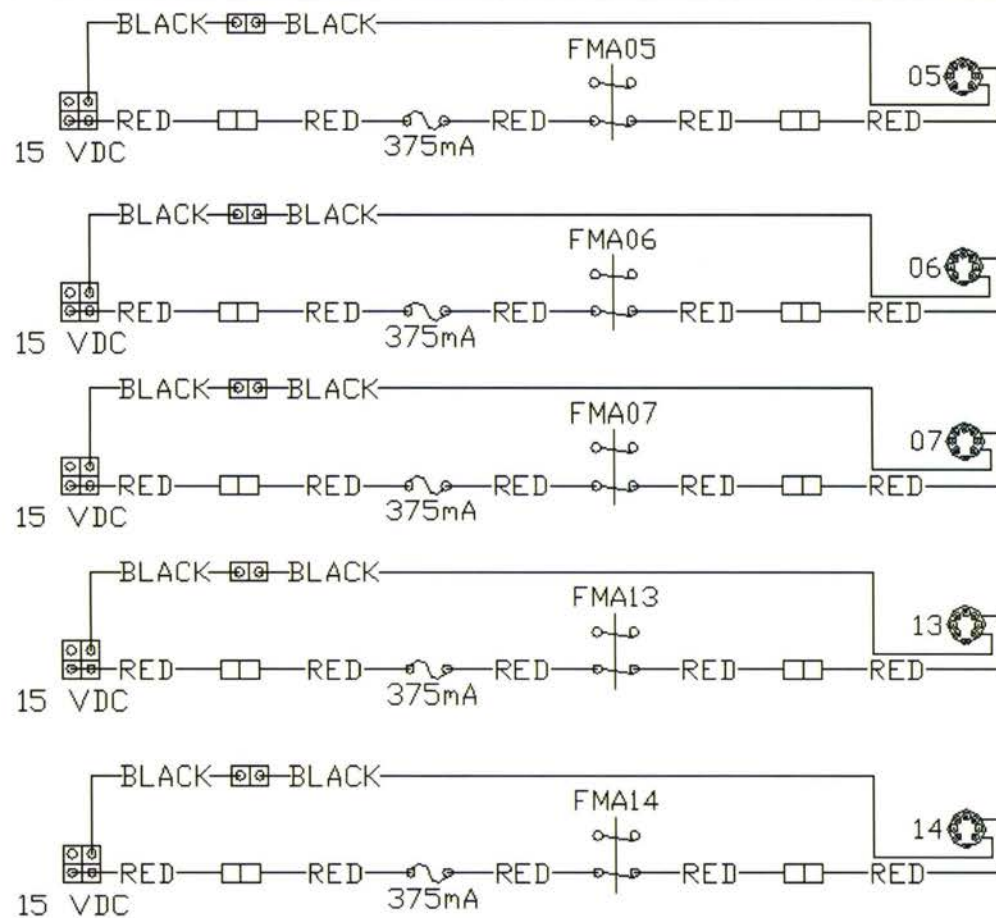
TERMINAL BOARDS

MAY 8, 2009

DALE MOLENAAR

RYERSON UNIVERSITY





BOX #2 WIRING DIAGRAM

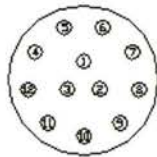
15V CONNECTIONS

MAY 12, 2009

DALE MOLENAAR

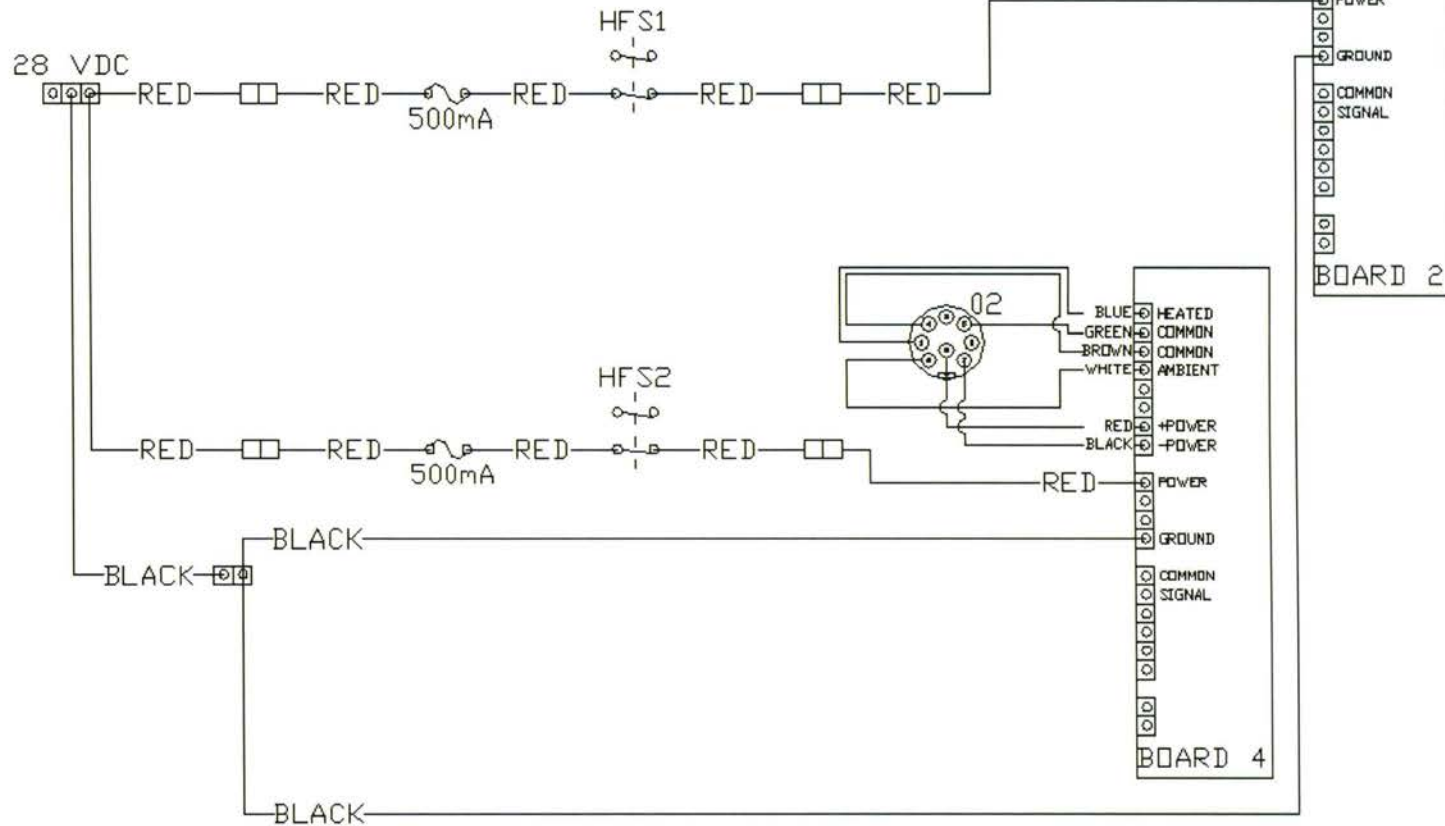
RYERSON UNIVERSITY

SENSOR PINS



- 1: RED (+POWER) PREH 8
- 4: BLACK (-POWER) PREH 7
- 6: BLUE (HEATED) PREH 1
- 7: GREEN (COMMON) PREH 5
- 7: BROWN (COMMON) PREH 4
- 9: WHITE (AMBIENT) PREH 6
- 10: ORANGE (TEMP) PREH 2
- 11: YELLOW (TEMP) PREH 3

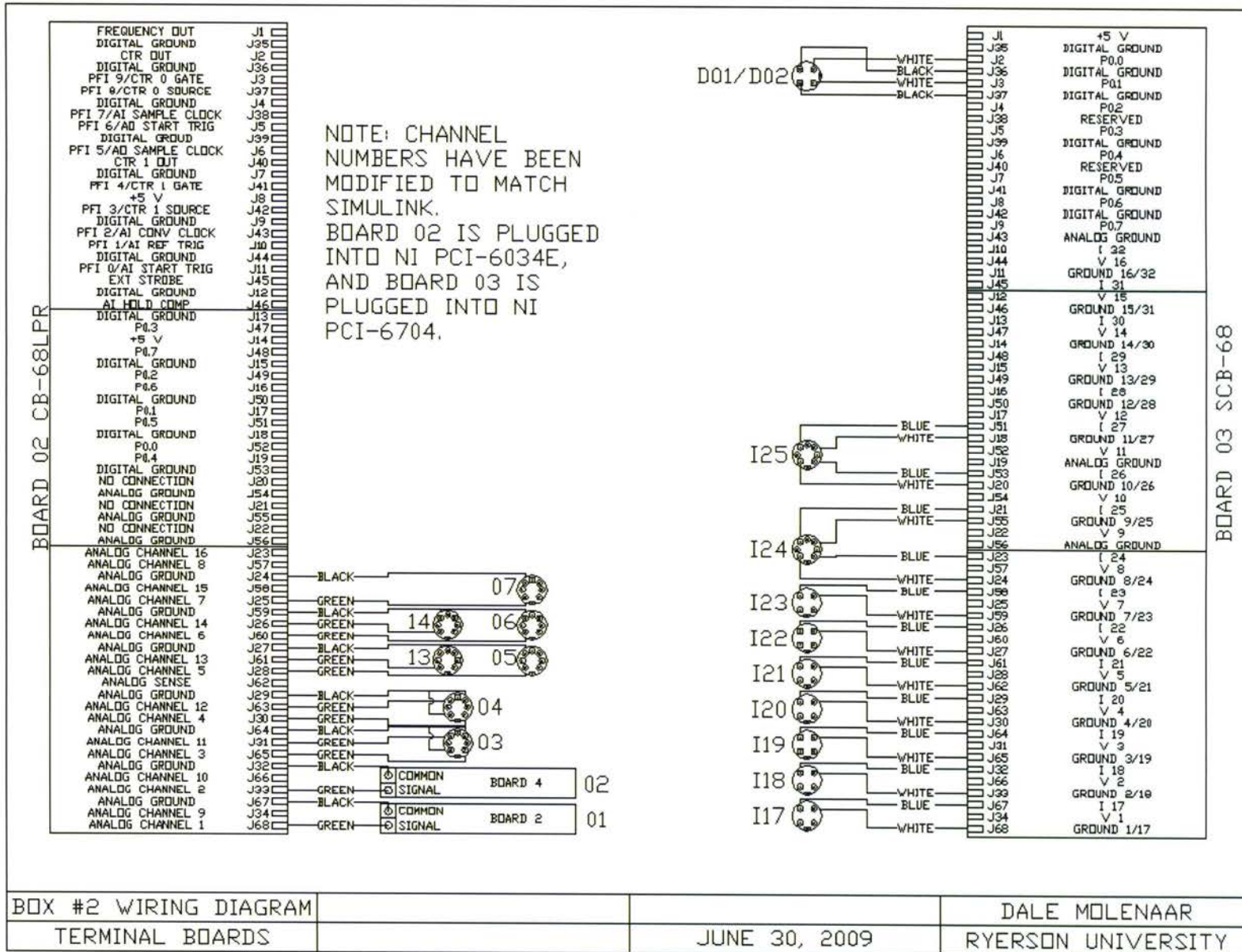
NOTE: CUSTOM PREH CONNECTORS HAVE BEEN ADDED TO BOTH FLOW SENSORS. ORANGE AND YELLOW WIRES HAVE NOT BEEN ATTACHED INSIDE THE BOX SINCE IT DOES NOT APPEAR THAT THE BOARDS SUPPORT TEMPERATURE SENSING. BOARDS TWO, THREE, AND FOUR HAVE BEEN TESTED, WITH BOARD THREE FOUND TO BE FAULTY.

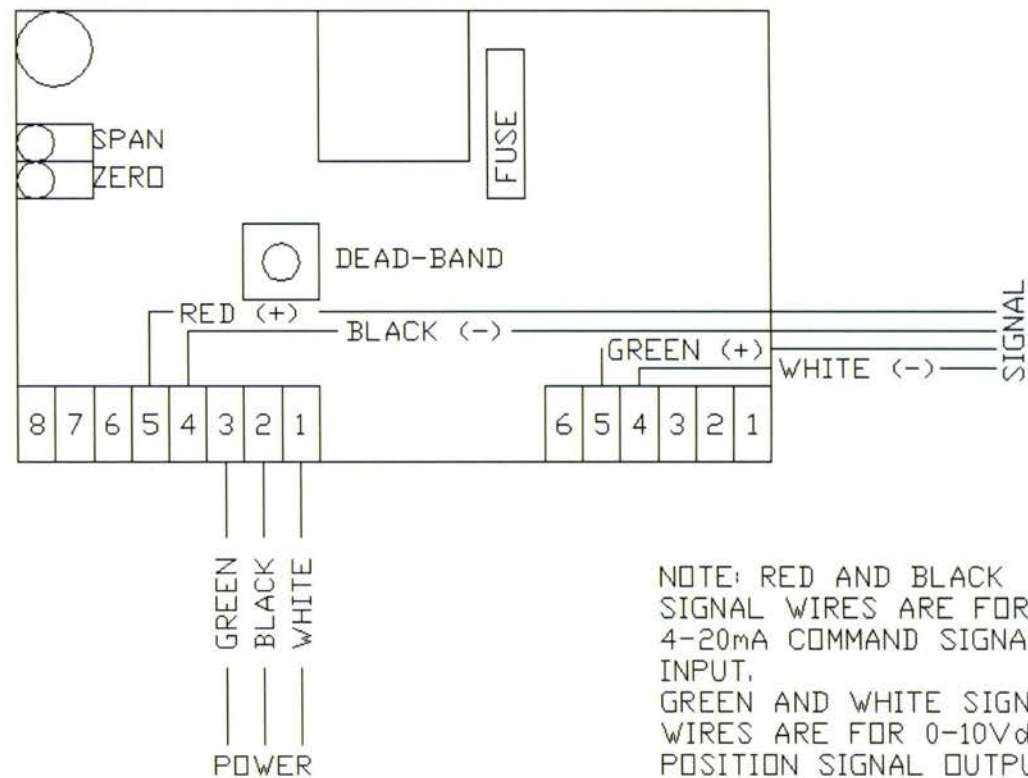


BOX #2 WIRING DIAGRAM
28V CONNECTIONS

JUNE 30, 2009

DALE MOLENAAR
RYERSON UNIVERSITY





VALVE DIAGRAM

JULY 20, 2009

DALE MOLENAAR

RYERSON UNIVERSITY